ABSTRACT

Title of Thesis:	BPOD: A WIRELESS INTEGRATED SENSOR PLATFORM FOR CONTINUOUS LOCALIZED BIOPROCESS MONITORING
	Justin M. Stine, Master of Science, 2019
Thesis Directed By:	Dr. Reza Ghodssi Department of Electrical and Computer Engineering Institute for Systems Research

Process parameter spatial inhomogeneities inside cell culture bioreactors has attracted considerable attention, however, few technologies allow investigation of the impact of these variations on process yield. Commercially available sensing probes sit at fixed locations, failing to capture the spatial distribution of process metrics. The bio-Processing online device (bPod) addresses this problem by performing real-time in situ monitoring of dissolved oxygen (DO) within bioreactor cell cultures. The bPod is an integrated system comprised of a potentiostat analog-front-end, a Bluetooth Low Energy microcontroller, and a Clark-type electrochemical DO sensor. The Clark-type sensor uses chronoamperometry to determine the DO percent saturation within a range relevant for mammalian cell culture. The free-floating capsule is packaged inside a 3D-printed biocompatible shell and wirelessly transmits data to a smartphone while submerged in the reactor. Furthermore, the bPod demonstrated a sensitivity of 37.5

nA/DO%, and can be adapted to multiple sensor types, enabling numerous bioprocess monitoring applications.

bPOD: A WIRELESS INTEGRATED SENSOR PLATFORM FOR CONTINUOUS LOCALIZED BIOPROCESS MONITORING

by

Justin Matthew Stine

Thesis submitted to the Faculty of the Graduate School of the
University of Maryland, College Park, in partial fulfillment
of the requirements for the degree of
Master of Science
2019

Advisory Committee:
Professor Reza Ghodssi, Chair
Professor Pamela Abshire
Professor William Bentley

.

Dedication

To my parents, Victor and Melissa, and my younger brothers Colin and Mason, for their love and support.

Acknowledgements

I would like to acknowledge my advisor Prof. Reza Ghodssi for his guidance and support throughout the completion of this work, as well as his tireless patience and motivation to maintain my focus and achieve success. I would also like to thank my committee members, Prof. William Bentley and Prof. Pamela Abshire for their constructive feedback and influence with this work and beyond.

I would like to give a special thanks to Dr. Luke Beardslee whose collaboration and mentorship has helped exceed all expectations for this project and myself as a researcher. Also, to all my colleagues from the MEMS Sensors and Actuators Laboratory (MSAL) to 'whom' I am grateful for correcting my grammar and for their insightful discussions. Also, I would like to acknowledge Ben Woodard and the staff of the Bioreactor Scale-up Facility (BSF), for assisting with the bioreactor setup, as well as the Bentley Lab for their assistance with my experiments and warm welcome to the Clark Hall lab space.

Lastly, to the funding agency from National Science Foundation - Advanced Mammalian Biomanufacturing Innovation Center (NSF-AMBIC) [Award Number: 1841506] for their generous support throughout this work, and the staff of the Maryland Nanocenter, Mr. Thomas Loughran, Mr. John Abraham, Mr. Jonathan Hummel, and Mr. Mark Lecates, for their assistance during the sensor fabrication.

Table of Contents

List of Tables

List of Figures

List of Abbreviations

(Listed Alphabetically)

ADC: Analog-to-digital converter

AFE: Analog-front-end

AMI: Acetone, methanol, and isopropanol rinse

BLE: Bluetooth low energy

bPod: bio-Process online analytical device

CA: Chronoamperometry

CAD: Computer aided design

CE: Counter electrode

CEC: Card edge connector

CHO: Chinese Hamster Ovary cells

COTS: Commercial-off-the-shelf, components

CV: Cyclic voltammetry

DIP: Dual in-line package

DO: Dissolved oxygen

EM1: Active mode for BGM121 Bluetooth micro-controller

EM2: Low-energy mode for BGM121 Bluetooth micro-controller

EM4: Shutdown mode for BGM121 Bluetooth micro-controller

FDA: Food Drug Administration

FDM: Fused deposition modeling

FEP: Fluorinated ethylene propylene

GI: Gastrointestinal

GOx: Glucose oxidase

GPIO: General input/output pin

H/D: Height/Diameter ratio factor for bioreactors

I^2C: Inter integrated circuit

IC: Integrated circuit

k_LA: Ratio of oxygen cell uptake rate and oxygen gas-liquid interface transport rate

Li-Ion: Lithium-Ion

mAb: monoclonal antibodies

MCU: Micro-controller unit,

PAT: Process analytical technology

PBS: Phosphate buffered saline, or phosphate buffer solution, a commonly used buffer solution in biological studies.

PCB: Printed circuit board

PDMS: Polydimethylsiloxane, a transparent, biocompatible, and chemically inert silicone-based polymer.

RE: Reference electrode

RFID: Radio frequency identification

RSSI: Received signal strength indicator

SiP: System in package

SLA: Stereolithography

STR: Mechanically stirred tank bioreactor

SUB: Single-use bioreactor

TIA: Transimpedance amplifier

UART: Universal Asynchronous Receiver/Transmitter

WE: Working electrode

Chapter 1. Introduction

1.1. Background and Motivation

Recent advancements in continuous monitoring of large-scale pharmaceutical bioprocessing has enabled rapid, high quality, and high throughput production of a wide variety of mammalian and bacterial culture products (i.e., biopharmaceuticals, antibiotics, and vaccines). Among these, monoclonal antibodies (mAb) are a critical product for both therapies and diagnostics. Monoclonal antibodies are capable of targeting specific antigens and are gaining traction in the treatment of cancer and autoimmune disorders among others [1]–[4]. Furthermore, scaling and optimization of these processes has driven significant financial investment from biopharmaceutical and biomanufacturing industries with global biopharmaceutical market values expected to reach approximately $390 billion by the end of 2019 [5].

A major concern, most common in large-scale bioreactors, is the presence of spatial gradients or heterogeneity of culture parameters that reduces bioreactor product yield and creates products with varying or inconsistent efficacy [6]–[8]. For example, controlling bioreactor heterogeneity is relevant to recombinant DNA processes utilizing *Escherichia coli* (*E. coli*), as well as other highly productive mammalian cell lines, such as Chinese Hamster Ovary (CHO) cells, as a host organism. Widespread use of CHO cells has been attributed to the demonstrated safety of CHO cells as a host, their low specific productivity, capacity for efficient post-translational modification compatible with humans, and easily adaptability to growth in serum [9]. The proliferation of *E. coli* recombinant DNA products and CHO cells is controlled by the

precise regulation of culture parameters throughout the bioreactor, namely, dissolved oxygen (DO), pH, glucose, and temperature [10]. More uniform distribution of these process parameters throughout the reactor will create better, more reliable products. Understanding the origin of these inhomogeneities and how process parameters effect the uniformity of the reactor products is critical to obtaining higher process yields with ultimately more effective products. Currently, standard techniques for monitoring culture parameters in bioreactors involve inline instrumental probes – widely used amongst the biomanufacturing and biopharmaceutical industries. However, inline probes only represent a single-point measurement taken as the averaged value for an entire cell reactor [11]. To overcome this limitation, new implementations of real-time in-situ sensors are needed that can permeate the bioreactor flows to achieve high precision bioprocess monitoring.

Wireless *in situ* devices exhibit numerous advantages over traditional probes and will help to eliminate reactor condition non-uniformities. Most notably, they interact locally with solutions/feedstocks throughout the reactor, have a lower contamination risk and represent a cost-effective path towards device scaling and multiplexed measurements, providing significant improvements in process scale-up and bioreactor optimization [12]. However, wireless modules must overcome several challenges towards bioprocess monitoring before becoming viable replacements, such as power consumption, module size, biocompatibility with products, and communication through a lossy media. Moreover, methods integrating commercial-off-the-shelf (COTS) components with wireless modules have enabled a variety of new applications using *in situ* sensors and packaging configurations for specific

environments [13]–[17]. By modernizing current approaches with application specific electronics, miniaturized sensors, and 'smart' materials, devices can address a variety of challenges at a lower cost and with higher resolution than ever before. The paradigm of integrating microsystems and biosensor technologies is well positioned to not only enhance capabilities but revolutionize the next generation of bioprocess monitoring for the biomedical and biomanufacturing industries.

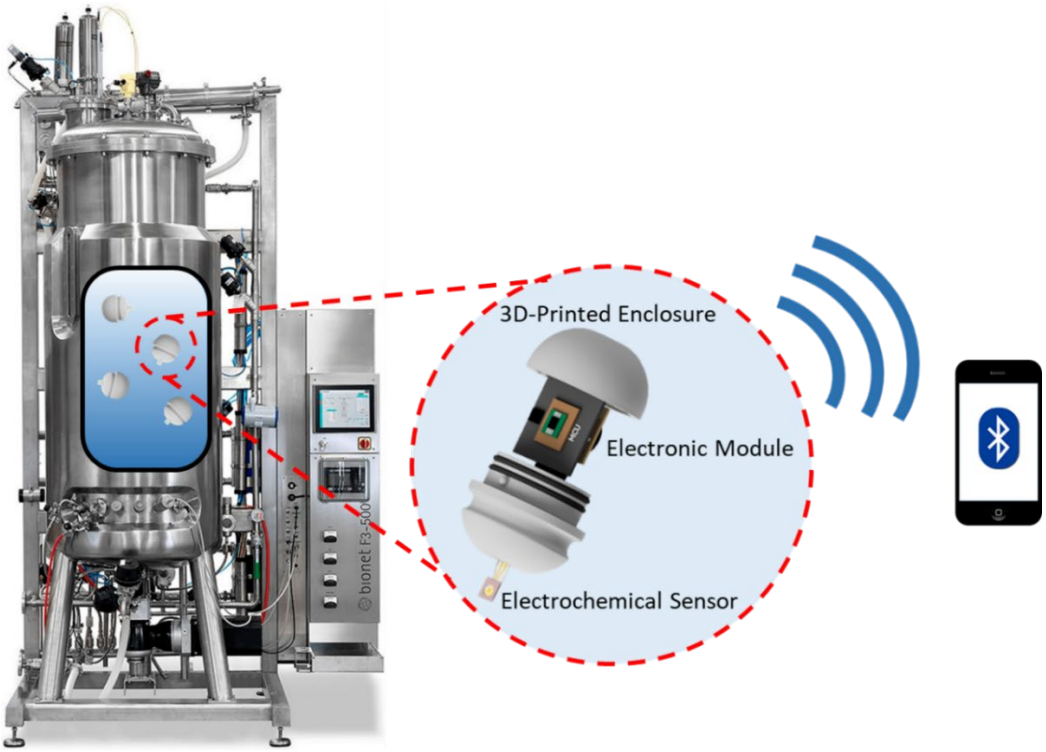

Figure 1-1. Conceptual overview of fully integrated bio-process online analytical device (bPod). Module swarm is deployed into stain-less steal bioreactor. bPod system components allow for underwater amperometric measurement of DO and wirelessly transmit the data to an external device via Bluetooth communication.

In this work, the bio-process online analytical device (bPod) was developed for real-time wireless, *in situ* monitoring of dissolved oxygen. The bPod highlights

integration and design of key system components to achieve a scalable prototype that specifically addresses challenges associated with *in situ* sensing within bioreactors. The platform consists of an electrochemical Clark-type oxygen sensor [18] and an amperometric potentiostat readout circuit paired with a Bluetooth low energy (BLE) system-in-package (SiP) microcontroller all contained within a leak-proof 3D-printed package. The BLE functionality allow for wireless data transmission to a custom smartphone app while the Clark-type gold electrochemical sensor enables the measurement of dissolved oxygen partial pressure in a non-conductive media.

1.2. Thesis Accomplishments

1.2.1. Development of Wireless 'smart marble' Platform

The goals of this research are the design and systems integration of a marble-like platform for wireless real time, *in situ* bioprocess monitoring within industrial bioreactors. Initial efforts into this topic sought to improve understanding of suitable wireless modalities for data transmission through a lossy media, design of a readout circuit topology that would enable electrochemical sensing, as well as 3D-printing a bio-compatible enclosure designed to encapsulate the device. Comparative studies of multiple wireless communication methods were conducted focusing primarily on scalability of the system and the availability of needed functionality. Key metrics considered were form factor, power consumption, available peripherals, and wireless transmission performance. It was determined that a BLE communication solution would satisfy all key design requirements, while also providing capabilities for future adaptation into a sensor network (i.e. Bluetooth Mesh) enabling robust device-to-

device communication. Additionally, the system takes advantage of COTS components to achieve a workable prototype for sensor testing.

1.2.2. Integration of Dissolved Oxygen Sensor for Real-time Monitoring

In order to successfully demonstrate the effectiveness of the platform, monitoring of a pertinent bioprocess parameter was explored. While initially investigating glucose and temperature sensing it was determined that the detection of dissolved oxygen content during the cell culture would prove to be essential in multiple bioreactor environments. Therefore, the primary focus of this work is the fabrication and integration of a dissolved oxygen sensor with the proposed platform. A three-electrode electrochemical oxygen sensor based on a Clark-type electrode configuration was explored. For oxygen sensing, the electrodes are contained within an electrolyte solution and are isolated from the surrounding media using a gas permeable fluorinated ethylene propylene (FEP) membrane. Leveraging the material properties of the electrodes and membrane, respectively, a fully integrated device prototype was assembled and tested at various dissolved oxygen saturation percentages generated using mixtures of pure oxygen and nitrogen and compared to a commercial inline DO probe.

1.3. Literature Review

The following section presents background information and a review of literature relevant to this thesis. First, a review of bioreactor design and flow dynamics is presented with a focus on identifying sources of culture parameter heterogeneity.

Second, a review of electrochemical and optical methods for monitoring dissolved oxygen is included. Finally, insights into microsystems and systems components essential for realizing *in situ* monitoring within a lossy environment are presented. The presented literature will be confined to gastrointestinal (GI) tract ingestible capsules and bioprocessing capsules.

1.3.1. Bioreactor Scale-up

Bioprocess scale-up is a critical component of process development in the biopharmaceutical industry. Manufacturing technologies which dictate the purification and proliferation of cell culture products are divided into up- and downstream processing. Upstream processes encompass cell line development and engineering, cell clone selection, media and feed development, bioprocess development, and scale up [12], [19], [20]. Downstream processes include cell purification and chromatographic polishing steps directed towards producing a purified (i.e., to relevant FDA standards) and usable product (i.e. monoclonal antibodies and Fc fusion proteins). Development of these therapeutic modalities has become increasingly important with the recent approval of several drugs for a range of critical illnesses [21], [22]. In addition, increasing demands for greater product quality, quantity, and variety, while at the same time demanding lower costs have presented a significant challenge for overcoming process bottleneck within each of the upstream and downstream flow steps, as seen in Figure 1-2. Notably, emerging technologies and optimizations within upstream bio-processing have driven advances toward bioreactor design and continuous monitoring

strategies for scaling cell culture production, particularly mammalian cells, improving product yield and quality [10], [12].

Cell cultures are typically first produced at a bench-top scale before moving to larger bioreactors for commercial production, where ideally vast quantities of products are generated with equal quality and yield. In particular, CHO cells, often used for production of therapeutic proteins, are among the most important biopharmaceutical products and as such have been the focus of many investigations for scale-up in stirred tank bioreactor designs. Several key factors which influence the yield of a production process are the time to accumulate the desired amount of biomass, the process duration, and the specific productivity of a particular species [23]. The production of recombinant protein, such as a biotherapeutic, it is essential to ensure that a consistent glycosylation profile, or attachment of glycan structures, is maintained throughout the bioreactor growth cycle.

Due to the complexity of the protein products, irregularities and variations of the glycosylation sites, or micro-heterogeneities, can occur due to a depletion of nutrients, which ultimately effects the final product quality [24]. More specifically, varied distributions of process parameters DO, pH, CO2, and glucose among others, are known as a significant source of heterogeneity for mammalian cells and related proteins (i.e. mAb) in large-scale bioreactors. Formation of either hypoxic or hyperoxic regions have produced varied glycosylation pattern, charge variants, aggregates, and low-molecular-weight species [7]. Limiting sources of heterogeneity has become a focal point of mAb and CHO cell production scale-up, and has been extensively

discussed amongst researchers and industry [7], [8], [12], [22], [23], [25]–[29]. The United States Food and Drug Administration's (FDA) has also supported innovation efforts through the process analytical technology (PAT) initiative, which supports the design, analysis, and control of manufacturing through timely measurement of critical quality attributes in the bioreactor process. Following PAT, new technologies that improve final product quality are increasingly sought after for implementation into the manufacturing process [30]. To identify possible sources of heterogeneity within bioreactors, design parameters for bioreactor design and culture mixing strategies will be explored.

Figure 1-2. Biopharmaceutical manufacturing technology flowchart for Upstream and Downstream bioprocess modified from [20].

Bioreactor Design

Bioreactor topology and parameters which dictate aeration and agitation within the bioreactor are critical for successful batch culture processes. Currently, a variety of bioreactor topologies are utilized, including mechanically-stirred tank bioreactors (STR), airlift bioreactors, and single-use bioreactors [31]–[33]. Though there exists a multitude of bioreactor types targeted towards specific specialized product species, STR bioreactors remain the most prevalent among the biopharmaceutical industry. This is primarily due to the ease of consistent process scaling, which can range from 10 L glass vessels up to 500 L - 5000 L stainless steel reactors. More recently, single-use bioreactors (SUBs) are notably rising in popularity and eliminate the need for cleaning or sterilization, significantly reducing contamination rates [12], [34]. Additionally, SUBs allow for more flexible design and can be adapted to address many different cell culture variations, while also achieving 500 L bioreactor scale production. However, for popular mammalian cell culture lines (CHO and mAb) STR bioreactors remain the preferred means for producing large quantities of product.

Despite numerous architectures there exist standardize parameters to compare the efficiency of different bioreactors, namely, mixing time of the system, volumetric mass transfer coefficient k_La and the specific power input. STR bioreactors consist primarily of the following components as seen in Figure 1-3:

1. Gas cylinder – Source of air and N_2 for calibration of the DO probe and providing DO for cell respiration.
2. Mass flow controller – Controls the ratio of air and N_2 entering the vessel for varied DO% saturation values.
3. Heating coil – Maintains the bioreactor environment at 35°C by heating the system.
4. Air sparger – Produces bubble patterns of the input gas mixture.
5. Impellers/agitators – Driven aeration mechanism for homogeneous mixing of bioreactor contents.
6. Baffles – Metal vanes to help direct fluid flow.
7. DO & temperature probe – Measurement probes for assessment culture parameters.
8. Chiller – Maintains the bioreactor environment at 35°C by cooling the system.
9. Data acquisition system – Meter for analyzing probe outputs and controlling cell culture cascade.

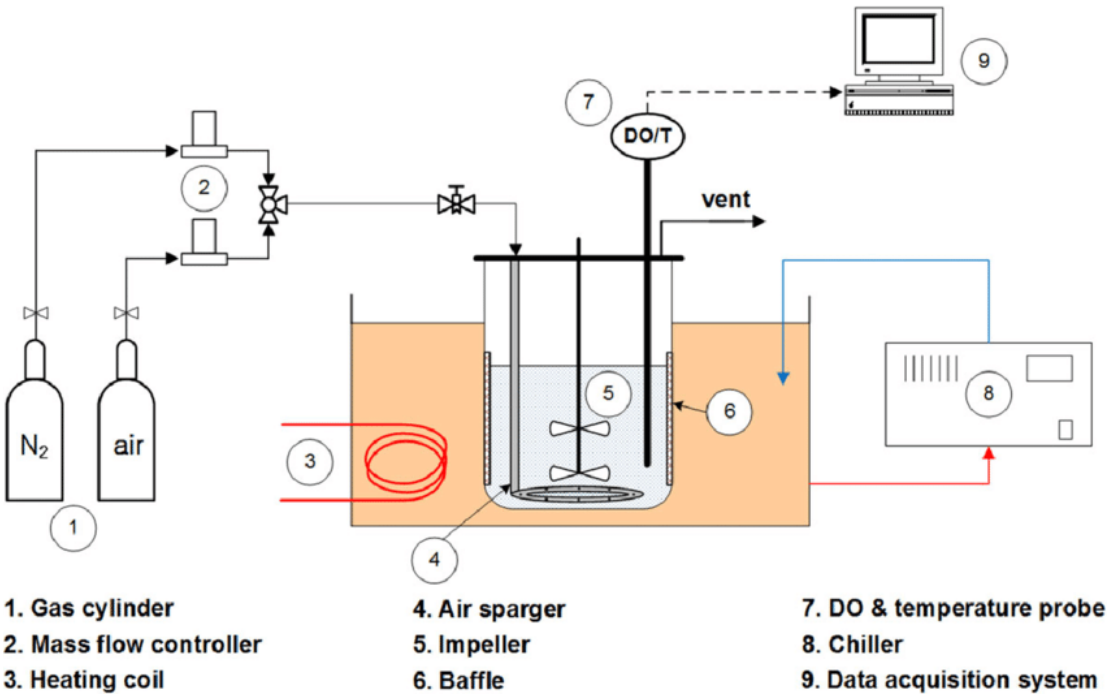

Figure 1-3. Schematic diagram of stirred tank bioreactor topology [35].

Common dimensions for STR bioreactors are denoted by aspect ratio (H/D) of the height and diameter of the vessel. This may differ depending on the types of cells or proteins being cultured, but typically are found in ratios of 3:1 and 5:1 for large scale bioreactors [36]. Key parameters are power input to the motor for driving the impeller, RPM and tip speed that determine system agitation, gassing/aeration or airflow (VVM rate: volume of air per volume of liquid per minute), and the viscosity of the cell culture [37]. Additionally, as bioreactors continue to scale the importance of maintaining product yield and quality becomes more difficult. Zhou et al. have investigated the effects of temperature, agitation, and aeration on glycoprotein GP-1 production in bench-scale fermenters [38].

Bioreactor Mixing

Why is mixing in bioreactors necessary? Oxygen is fundamental for growth, production, and maintenance of all cellular activities in the bioreactor. Cells are able to obtain the necessary oxygen in a non-compound form, called dissolved oxygen, which is provided to the cells through agitation and aeration of the system [39]. Agitation disperses oxygen bubbles released by the sparger and promotes molecular transport throughout the bioreactor. The rate of oxygen transfer to dissolved oxygen (OTR) across the gas-liquid interface is dependent on many factors including the fluid properties, the size of the bubbles, system geometry, and operating conditions of the bioreactor as mentioned above [40]–[42]. The ability of the cell culture to absorb DO and the effect on the growth of the microbial species is defined as the oxygen uptake rate (OUR). The ratio of OUR and OTR characterizes the efficiency and effectiveness

of the bioreactor and is defined as k_La. The k_La parameter should remain constant for scaling of the same bioreactor topology and is used to compare various bioreactor designs. The k_La for bioreactors is determined using two methods: the sulfite oxidation method which scavenges oxygen for a catalyst reaction, and the dynamic method which involves analyzing the DO concentration during brief interrupts in aeration [43]. In either case the homogeneity of the system is reflected in the accuracy of the estimated k_La and both improved mixing and evaluation methods are critical for determining optimal bioreactor design [44].

STR's are widely used as mixing vessels for bioreactors and aeration systems. Homogeneous mixing of the process feedstocks leading to a homogenous distribution of parameters (DO, pH, and temp), as well as reactor constituents has motivated various modifications of impeller blade design and positioning within the bioreactor vessels. A balance between improving k_La and overall system mixing, and minimizing damage to the cell lines from the impeller blades oscillations due to sheer stress has been the focus of much research into the effects of agitation on cell growth [45]–[47]. To achieve a suitable mixing condition the agitation of the system is defined by the Reynolds number, which describes several flow regimes, namely laminar, transient, and turbulent; the latter of which is ideal for homogenous mixing. To this end, the effects of various Rushton turbine impeller fin geometries, the number of blades (triple and double), the spacing between the blades, and the eccentricity of the rotational axis of the impeller have been characterized and in most cases provide a representative k_La parameter [48]–[50]. Figure 1-4 from Cervantes et al. compares the dispersion of a dye blob after equivalent impeller rotations, showing a more rapid response for eccentric

bioreactor design [50]. The mixing time necessary to reach a homogeneous state (+/- 5% variation), or for the target parameter to become fully dispersed in the liquid environment, may vary significantly between designs and adding multiple impellors have been known to cause stagnant “dead zones” if not spaced properly. Heterogeneities due to “dead zones” in the flow pattern are a type of macro-scale mixing related to agitation, while micro-scale mixing sources can be derived from eddies of the turbulent flows that can hinder cell growth [51]. Despite challenges towards achieving truly homogenous process parameter distribution at an ever increasing scale, integrated continuous monitoring has shown potential to revolutionize bioprocessing, and deliver low-cost biopharmaceuticals for addressing critical health challenges [28].

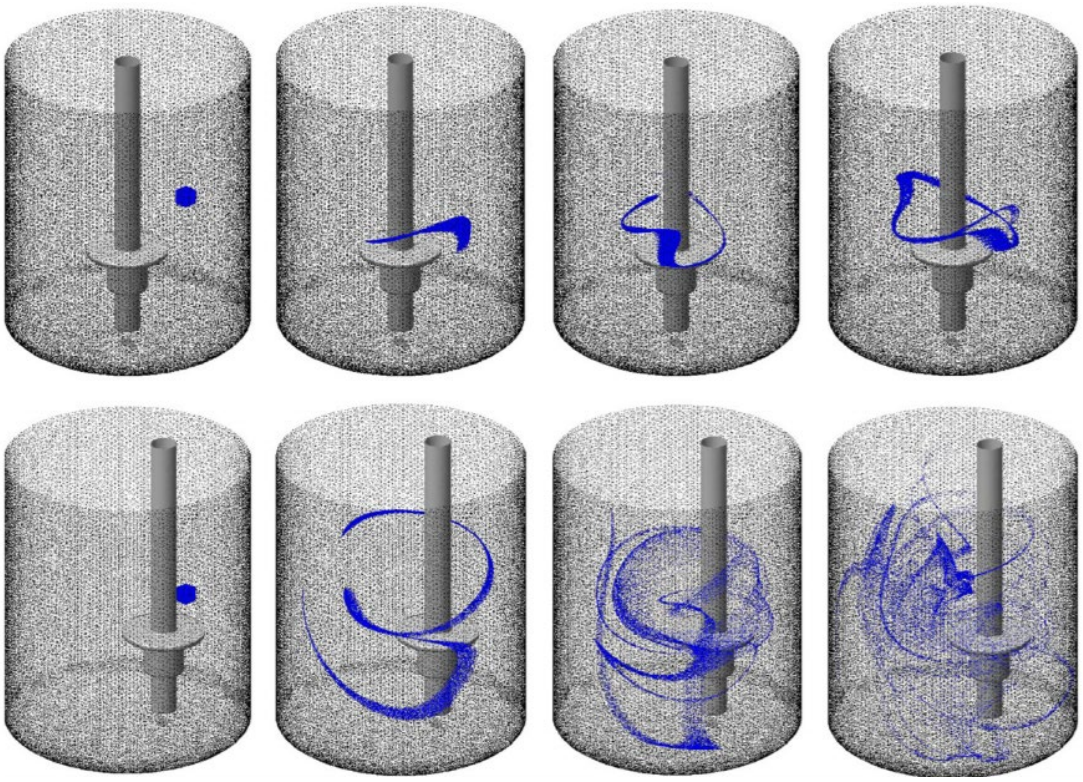

Figure 1-4. Computational model of dispersion of "dye" blob for two stirred tank bioreactor designs: concentric and eccentric. Highlights relationship of bioreactor dimensionality on how quickly homogeneous distribution of particles can be achieved [50].

1.3.2. Monitoring of DO in Bioprocessing

Dissolved oxygen plays a critical role in the proliferation of batch cell cultures and maintaining a homogeneous oxygen distribution throughout the bioreactor is key to successful cell proliferation. As biomass increases, poor distribution of DO can form hypoxic zones. Some biologics, including mAb are produced with varied aggregation patterns of oxidation, deamidation, glycosylation, charge, etc. due in part to the nonuniform distribution of parameters such as dissolved oxygen. Reducing these inhomogeneities requires targeted online and automated measurements [52]. Standard approaches rely on optical and amperometric measurement of the partial pressure of

DO [43]. In general, optical sensors are resilient to flow and more accurate than amperometric sensors [53]. However, they have a comparatively slow response time and high power consumption, which would invariably hinder embedded monitoring approaches that dynamically sample within a bioreactor. In this section recent developments in optical and electrochemical DO sensing applications will be reviewed.

Electrochemical Measurement of DO

Since 1953 the Clark-type electrode has provided a standard method for electrochemical sensing of oxygen and has been utilized for a wide range of applications including blood gas analysis, glucose monitoring, and oceanography [18], [54]. The Clark cell produces a linear amperometric current proportional to the partial pressure of oxygen under an external polarization voltage. This partial pressure can be represented as a concentration or a percentage saturation. This system is derived from a basic electrochemical cell involving a silver/silver chloride reference anode, a platinum cathode, and an electrolyte solution – typically potassium chloride. The anode, or negative electrode, serves as a terminal for which the flow of current is directed, whereas the cathode, or positive electrode, is the terminal for which current flows out of. The electrolyte serves as a medium for electron transfer by providing excess ions. When a potential difference is applied between these two electrodes the flow of electrons can elicit a chemical reaction, or redox reaction, within the solution. The polarity of the source voltage dictates the direction of this electron flow and causes either an oxidation reaction, release of electrons by the atom or molecule, or a reduction reaction, or the addition of electrons by the atom or molecule.

Polarographic probes are widely used commercially as dissolved oxygen sensing probes in bioreactors, and are amenable for monitoring several comparable gas species such as dissolved carbon dioxide (dCO_2) and nitric oxide (NO) which like oxygen is permeable to membrane [54]. Polarographic probes are a type of electrochemical sensor that utilizes a gas permeable membrane to allow dissolved gas to diffuse from the sample into the Clark-type electrode sensor, which is surrounded by an electrolyte buffer. A constant voltage applied to the probe is required for monitoring DO and similar gases, which requires 5-15 minutes of charging/polarization prior to operation. An illustration of a commercial polarographic probe is seen in Figure 1-5A, and a schematic of the underlying geometry is shown in Figure 1-5B. Electrochemical monitoring using polarographic probes in bioreactors while well understood for a wide range of cell parameters, in their current implementation are quite bulky, require frequent membrane replacement, and provide a single-point measurement defining an averaged value for the entire cell culture.

To this end, significant efforts towards miniaturization of the dissolved oxygen sensing electrodes and isolation from various media has been explored for applications in the biomanufacturing and biomedical field [55]–[57]. MEMS fabrication techniques have been increasingly employed to microfabricate working electrode structures, enabling fast response times, high sensitivities, small sample volumes, and reproducible geometries [58]. Twomey et al. have utilized nanoporous gold microdisc arrays to achieve lower signal-to-noise ratio and faster response time when compared to commercial dissolved oxygen sensors [59]. Novel Ag/AgCl anode structures have also been investigated to improve the stability of micro-fabricated

Clark-type electrodes and verify their functionality [60], [61], however at the microscale and if integrated into a miniaturized sensing system could enable well-defined dynamic sensing capabilities across a wealth of relevant mammalian cell lines.

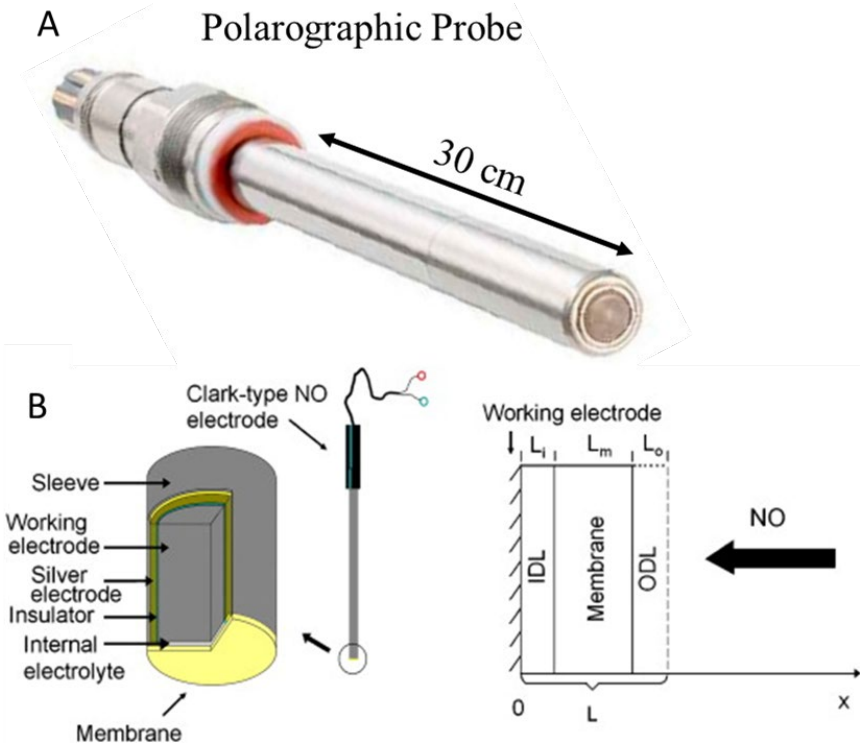

Figure 1-5. A) Commercial polarographic DO probe (Mettler Toledo). B) Diagram of probe layers of generic Clark-type electrode for NO, which like oxygen is permeable to membrane [54].

Optical Measurement of DO

The majority of optical DO sensing approaches are derived from fluorescence quenching based on the presence of oxygen. Dynamic quenching of fluorescence is described by the Stern-Volmer equation

$$\frac{F_0}{F} = 1 + k_+^* \tau_0 [O_2] \qquad (1\text{-}1)$$

, where F_0 and F are the fluorescence intensities in the absence and presence of a quencher, τ_0 is the fluorescence lifetime in the absence of quencher, and k_+^* is the bimolecular quenching constant [62]. The intensity of the quenching depends on the probability of the encounter between an oxygen molecule and the fluorescent particle. A light source is used to excite the fluorescent particle, however in the presence of molecular oxygen the energy which would otherwise be emitted is instead absorbed [63]. The general implementation consists of an oxygen sensitive particle or molecule, a polymer matrix to host the particle or molecule, and a read-out system for processing the data. Noted advantages of optical monitoring systems include (a) the lack of oxygen consumption during measurements; (b) full reversibility; (c) good precision and accuracy; and (d) the ease of miniaturization (down to the size of nanosensors) [53]. Recently, many organic and inorganic luminescent indicators have been designed, such as polycyclic aromatic hydrocarbons. However alone, these indicators have poor adhesion to glass probe substrates. Therefore, integration of the indicators with supporting materials, such as polyethylene glycol hydrogels and sol-gels with high oxygen permeability, is necessary to support the measurement of DO [64]. Staudinger et al. have demonstrated long-term optode systems for measuring oxygen, carbon dioxide and pH in seawater. Figure 1-6 shows the optode incorporated as an optical sensor device that measures the response of a chemical coating specific to each analyte of interest. A red light source was utilized to excite the sensor material, which transmits in the near infrared frequencies, and is recorded by a logger board [65]. McDonagh et al. also showed a method for ruggedizing a ruthenium DO sensor by immobilizing a hydrophobic sol-gel sensor film and demonstrated phase fluorometry [66].

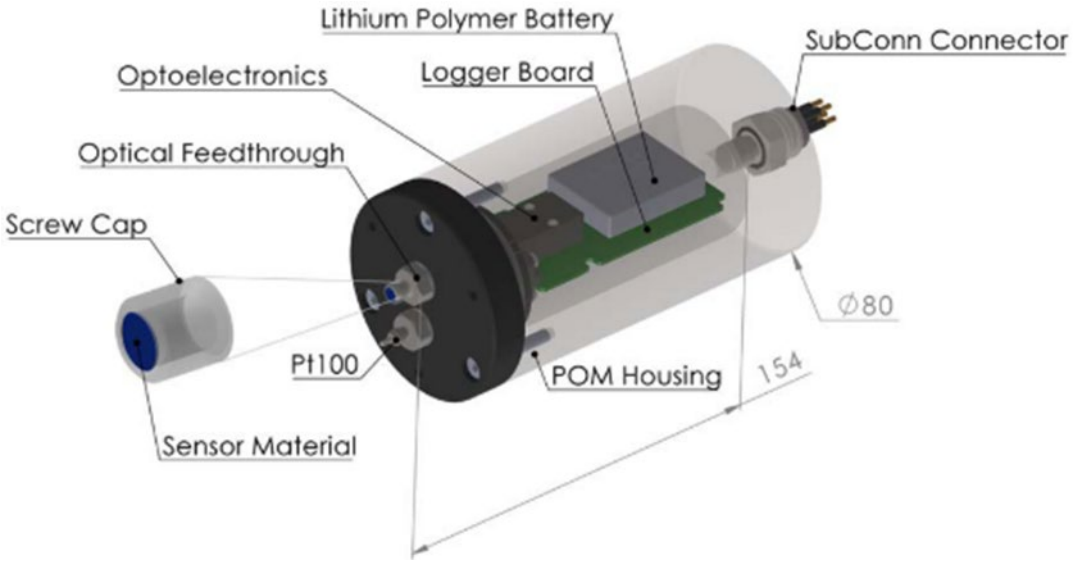

Figure 1-6. Sketch of the optode in a pressure housing with logic boards, Li-Polymer battery, optical feedthrough, temperature feedthrough, SubconnVR connector, and screw-able sensor cap [65].

1.3.3. Microsystems for *in situ* Monitoring

The design and usage of miniaturized systems as an analytical tool for healthcare and bioprocess monitoring has shown significant progress over the last decade, enabling interrogation of difficult to target environments. Common themes amongst these approaches is the use of COTS components to provide signal conditioning for on-board sensors, as well as the use of a microcontroller unit to process and wirelessly transmit data. Moreover, interfacing sensors or biosensors with application specific analog front ends (AFE) with COTS microcontrollers have become a robust and rapid prototyping option. Various applications for monitoring human health have taken advantages of this approach for achieving fully integrated systems [13], [14], [16]. For example, a hybrid electrochemical sensor platform targeting

capsaicin within food was investigated by Sopstad et al. utilizing stepped cyclic square wave voltammetry and carbon electrodes integrated with a printed circuit board [67].

In recent years, the Internet of Things (IoT) and sensor networks have become ubiquitous with wearables, healthcare monitoring, and smart homes, providing users' with unprecedented amounts of information and connecting multiple devices under a unified network [68]. These technological developments have led to a push for many variations of 'smart' technologies that enable exploration of previously difficult to monitor environments. Both ingestible capsules and bioprocessing microsystems utilize similar system components to enable *in situ* sensing to achieve higher sensitivity and reside within a target environment. Although IoT chipsets have made simple sensing nodes accessible and straightforward to develop and use, there remain significant shortcomings in existing IoT technology for RF transmission in a lossy environment, which require further exploration in their representative environments: the GI-tract and the STR bioreactor. Table 1-1 highlights several MCU's available with differing communication modalities to enable wireless connectivity to sensing systems.

Table 1-1. List of microcontrollers suitable for portable data transmission. Modules are organized by wireless communication modality and include key design parameters for integrated microsystems.

Ref	Company	Module Name	Modality	Size (mm)	Active Mode (dBm)	Max Power	Antenna	Cost
[69]	Silabs	WGM110	WiFi	L: 21.0 W: 14.4 H: 2.0	261mA @ +16	16 dBm	Yes	$12.19
[70]	Microchip	RN1810	WiFi	L: 17.8 W: 26.7 H:2.2	247mA @ +16	16 dBm	Yes	$17.48
[71]	Zentri	AMW106	WiFi	L: 20.3 W: 15.2	11.4mA @ 14	18 dBm	Yes	$15.30
[72]	Texas Instruments	CC3120	WiFi	L: 9.0 W: 9.0 H: 0.5	229mA @ +18	18 dBm	No	$8.40
[73]	Nordic Semiconductor	NRF9E5	sub-1GHz	L: 5.0 W: 5.0	9mA @ -10	10 dBm	No	$5.32
[74]	Silabs	EFR32	433 MHz	L: 7.0 W: 7.0	34mA @ 10.5	20 dBm	No	$8.08
[75]	Radiocrafts Tinymesh	RC1141-TM	433 MHz	L: 12.7 W: 25.4 H: 3.7	35mA	11 dBm	Yes	$14.36
[76]	Adafruit	RFM69HCW	433 MHz	L: 50.8 W: 22.8	130mA @ +20	20 dBm	Yes	$19.95
[77]	Nordic Semiconductor	nRF52810	BLE	L: 6.0 W: 6.0	4.6mA @ 0	4 dBm	No	$4.15
[78]	NXP Semiconductor	MKW41Z	BLE	L: 7.0 W: 7.0 H: 0.9	6mA @ +4	4 dBm	No	$7.24
[79]	Texas Instruments	CC2564-MODA	BLE	L: 7.0 W: 7.0 H: 1.4	107mA @ +10	10 dBm	Yes	$10.98
[80]	Silabs	BGM121	BLE	L: 6.5 W:6.5 H: 1.4	8.2mA @ 0	8 dBm	Yes	$10.48
[81]	Silabs	BGM13S	Bluetooth 5	L: 6.5 W:6.5 H: 1.4	8.9mA @ 0	18 dBm	Yes	$8.76
[82]	ST Electronics	STM32WB55	Bluetooth 5	L: 7.0 W: 7.0	5.2 mA @ 0	6 dBm	No	$8.44

Ingestible Capsules

Integration of microsystem components (i.e. materials, sensing modality, communication, and readout circuit) required for ingestible capsules are highly dependent on the target environment or system. In addition, many of these considerations share noted similarities to the expected bPod functionality and provide significant insight on packaging of the sensor and electronics, available biocompatible

materials, as well as wireless communication modalities available for complex environments.

Current commercial GI devices, namely, the Pillcam COLON, CorTemp, Proteus Digital and IntelliCap, incorporate sensing modalities ranging from pressure, pH, temperature, and optical measurement [83], [84]. Additionally, ingestible capsules have been developed for a host of sensing applications, targeting specific biomarkers, such as GI gases, oxidative analytes, and GI bleeding [85], [86]. Most existing capsules rely on sub-GHz wireless communication to transmit data. McCaffrey et al. have performed electrochemical examination of fluid within the colon using the 433MHz comminution band. COTS components, polyimide flex connects, and a lithium manganese oxide (11.4 mm diameter) battery are integrated to achieve sub-30 mm scales. Others utilize mechanical actuation of the device packaging to achieve prolonged residence for monitoring and drug delivery at specific locations [87]–[90]. The field is quickly evolving towards 'smart capsule' implementations that use Bluetooth for device to device communication [88]. Kong et al. have developed a GI capsule capable utilizing the expansion of 3D-printed poly-L-lactic acid (PLA) and flexible thermoplastic polyurethane (NinjaTek NinjaFlex 85A) for residing at the intersection of the stomach and small intestine, as seen in Figure 1-7. The expansion is triggered due to dissolution of a gelatin capsule within the stomach, and the capsule provides temperature measurements, as well as externally triggered drug delivery of doxycycline. Higher data rate sensor monitoring, but ultimately place more emphasis on a persistent, robust wireless link at the 2.45GHz frequency band. Overall, the recent

trends support technologies that augment automated nodes and seamlessly integrate diverse sensor modalities into emerging wireless mesh solutions.

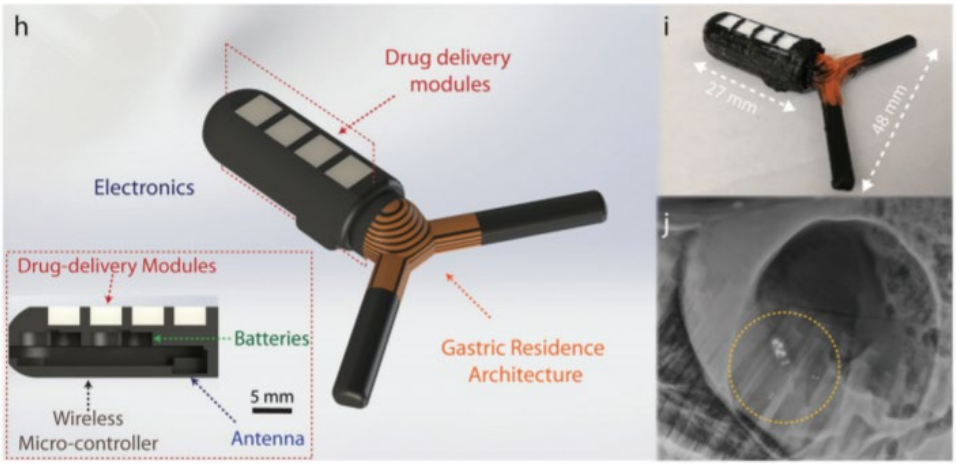

Figure 1-7. Image of gastric resident capsule integrating drug delivery and wireless Bluetooth communication [88].

Bioprocess Monitoring Microsystems

Bioprocess monitoring microsystems are important for bioprocess control for recombinant protein production, in which cells multiply until the desired cell density is reached [91]. Real-time *in situ* monitoring methods that can perform long term measurements have been demonstrated for a variety of process parameters. Radio frequency identification (RFID) tags are capable of passively interrogating the culture broth and have been demonstrated for monitoring temperature and humidity within single-use bioreactors [92]–[94]. The RFID tags are affixed to the bioreactor walls, wirelessly powered using an external source, and directly sterilized. However, RFID utilizing near-field communication are limited to glass and plastic walled vessels, and require scaling of the antenna size with increasing bioreactor volumes. Other RFID

systems have also been demonstrated for monitoring pH, as well as fixed sensor arrays for temperature monitoring [95]–[97].

There have been only a few reports demonstrating free-floating wireless sensors not requiring a physical connection to the bioreactor. Todtenburg et al. developed a capsule for detecting biochemical parameters, such as pH, glucose and conductivity within a photobioreactor. By integrating CMOS circuitry and COTS components, the device wirelessly transferred information to an external receiver [98]–[100]. The capsule consists of a waterproof top to protect the electronics and a liquid permeable bottom to expose the sensor to the culture media. Figure 1-8 displays the sensor capsule architecture and shows the wireless interrogation via 433 MHz communication with a base station.

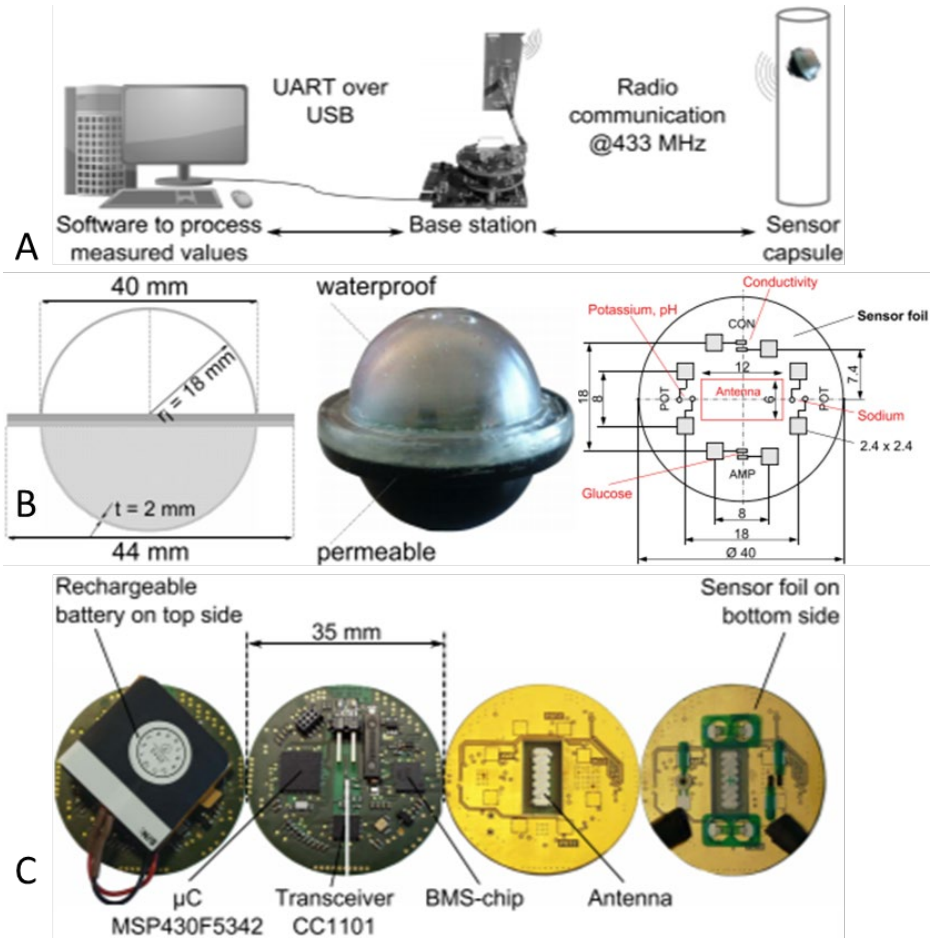

Figure 1-8. Bioprocess capsule developed by Todtenburg et al. for the evaluation of glucose and pH within photobioreactors. Capsule uses a liquid permeable seal to interface the sensors with the environment and stacked PCB design for achieving 40 mm diameter [98].

Zimmerman et al. have utilized sensor spheres to characterize fluid dynamics within turbulent flows of an aerated bioreactor. The sensors were a commercially available neutrally buoyant monitoring capsule fabricated from poly ether ketone (PEEK), known as smartCAP (smartINST, Lyon, France), which support several sensing modalities, including temperature, conductivity, and agitation [101] – specifications for the smartCAP product are summarized in Supplemental Table A-1. Additionally. the capsule's movements were tracked optically to correlate the location

to the measured acceleration, therefore identifying agitation and flow patterns within the mixed system [102], [103]. Other technologies derived from ingestible capsule microsystems, namely PATsule, have been investigated as potential devices designed to freely move around the bulk media of the bioreactor and monitor temperature, pH, and DOMcCaffrey et al. developed a wireless swallowable capsule, which leveraged a flip-chip-over-hole assembly to directly integrate and seal a dissolved oxygen sensor onto a printed circuit board [36], [104], [105]. However, transitioning from an ingestible integrated capsule to a bioprocess monitoring microsystem has yet to be realized.

These commercial products, smartCAPs and the PATsule [101], are shown in Figure 1-9, and have emerged to provide solutions for monitoring agitation, pressure, and conductivity of the bioreactor flows. Technologies within the bioprocessing field have yet to reach their full potential in terms of unlocking local variations within the reactor that lead to inhomogeneous products. These technologies will enable new explorative research towards eliminating bioprocess heterogeneity.

Figure 1-9. Commercial bioprocessing capsules for in situ monitoring within bioreactors. (Left) Illustration of PATsule a wireless bioprocess monitoring node derived from ingestible capsule technology [29], [104]. *(Right) Illustration of smartCAPS module, and demonstration of mixing within agitated bioreactor (smartINST)* [103].

1.4. System Overview of bio-Processing analytical Online Device (bPod)

The preceding sections presented the motivation behind the development of *in situ* wireless nodes for deployment in bioreactors, along with background information providing context for the design and development of the research and work presented in this thesis.

The proposed device contains three main system components: an electronic module, a leak-proof 3D-printed enclosure, and an electrochemical DO sensor. The electronic module utilizes a Bluetooth Low-Energy chipset and a portable potentiostat integrated circuit, or analog front end (AFE), to enable wireless amperometric monitoring of DO. The leak-proof packaging is 3D-printed using a biocompatible material, MED610, to seal the device using a combination of O-rings and an interlocking bayonet connector. A Clark-type DO sensor is assembled by forming an electrolyte well with electroplating tape, trapping the electrolyte with a liquid impermeable fluorinated ethylene propylene (FEP) membrane. This creates a gas permeable diffusion barrier between the solution and the electrolyte above the electrode surface.

In the envisioned implementation of the bPod deployment, multiple bPod's will be placed inside the bioreactor with each individual device performing localized measurements of relevant culture parameters. The bPod could be deployed in large stainless-steel bioreactors as well as small and large single use bioreactors (SUB), allowing the convenient extraction of information via BLE, or a Bluetooth Mesh approach. Eventually, these measurements could be fed back into the control system of the bioreactor enabling real-time tuning of culture parameters increasing process yield.

This thesis will be organized according to the outline below. The following chapters will introduce the systems components and discuss their integration and testing. Chapter 2 presents the design and fabrication of the electrochemical DO sensor along with considerations around the choice of sensor topology and packaging of the electrodes with the appropriate electrolyte. Chapter 3 will discuss the details of the

development of the integrated bPod system. Specifically, the design and construction of the electronic module and 3D-printed packaging, as well as the assembly of the bPod system. Chapter 4 will investigate the performance of the bPod platform by providing testing and results for several different characterization experiments in different environments. Finally, the integration of the electronic module, electrochemical DO sensor, and 3D-printed package for monitoring of DO will be explored, first providing a two-point calibration for establishing the measurement bounds and then the generation of a calibration curve in using a commercial inline DO probe as a gold standard reference. Lastly, Chapter 5 will provide a summary and conclusion of this work with mention of potential future directions. Supplemental materials, including all embedded programming code for the proposed microcontroller will be included at the conclusion of this document.

Chapter 2. Fabrication of Electrochemical DO Sensor

2.1. Overview

In this work, a three-electrode configuration is utilized for the amperometric measurement of dissolved oxygen partial pressure, denoted as a saturation percentage. Figure 2-1 illustrates the final DO sensor assembly, consisting of a contained reservoir of electrolyte solution on the three-electrode sensor with an attached fluorinated ethylene propylene (FEP) membrane to create a gas permeable, but liquid impermeable, interface between a contained electrolyte solution and the surrounding media.

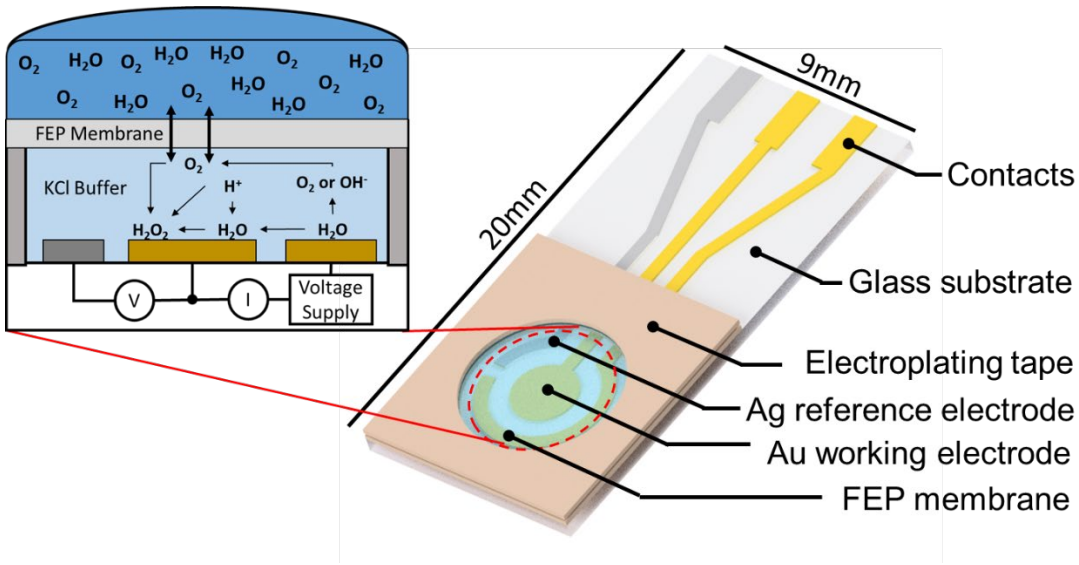

Figure 2-1. Illustration of assembled dissolved oxygen sensor and a cross-sectional diagram of oxygen reaction at the Clark-type electrode. The oxygen reduction reaction is measured using a three-electrode system with gold working and counter electrodes, and a silver reference electrode.

The previous chapter presented the bPod platform, and the system components used for interfacing with the sensor. The challenge of ensuring a reliable and leak-proof

interface is a prevalent theme throughout the chapter and dictates several modifications to the DO sensor assembly. In the following sections, the design, fabrication, and assembly of the proposed DO sensor and its components will be discussed.

2.2. Sensor Design

Here the full design and specifications for the fabricated electrode are explained, beginning with motivations for the sensor materials and topology, then moving towards specific fabrication details to complete the miniaturized DO sensor.

2.2.1. Glucose Sensor

The initial electrochemical sensor that was investigated for use in the bPod was a glucose sensor, chosen for the importance of glucose concentration in cell growth and metabolism [106]–[110]. Typical glucose sensing topologies involve three-electrode sensors with a glucose oxidase (GOx) functionalized working electrode. As glucose interacts with GOx at the surface of the electrode, under a specific voltage bias, a chemical reaction will produce hydrogen peroxide (H_2O_2). Reduction of H_2O_2 at a platinum working electrode produces a measurable reduction current, corresponding to a maximal excitation voltage peak. Extensive studies have been conducted that characterize both the functionalization/bonding of GOx to Clark electrodes, as well as modifications such as dendrimer analogues (nano-sized, radially symmetric molecules with homogeneous tree-like structures ideal for binding) to achieve chemical specificity to glucose as compared to other sugars (i.e. lactose and fructose) [111], [112]. While glucose biosensor applications are well documented and widely used amongst researchers and the general population, their one-time use or limited use (i.e.

glucose strips) application makes long term sensing at small scales very challenging. Since the overall architecture of the glucose sensor is based on similar implementations to the Clark cell oxygen sensor, it served as a natural segue into the design of a dissolved oxygen sensor, however the application was not pursued beyond electrochemical characterization of the sensors in glucose solutions. Additionally, signal conditioning requirements for the glucose sensor provided an initial platform for the development of the bPod electronics. Details of this characterization are included below and were critical for identifying several key design features of the final DO sensor assembly.

A commercial screen-printed glucose sensor (BVT Technologies), with GOx derived from *Aspergillus Niger* immobilized on a 1.0 mm diameter platinum electrode, was purchased from PalmSens for determining electrochemical parameters needed for design of the bPod potentiostat IC (Figure 2-2). The electrodes were 7.26 mm in width and 25.4 mm in length with a 2.54 mm pin pitch. The counter electrode was made of platinum and the reference electrode was made from silver.

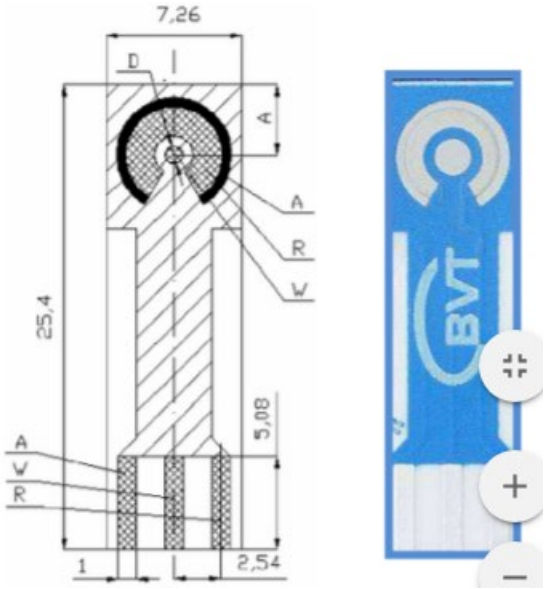

Figure 2-2. PalmSens glucose electrode with GOx (Aspergillus Niger) [113]. *The schematic provides the relevant dimensions of the AC1.GOD glucose sensor (in mm).*

The AC1.GOD glucose sensors were stored in a -20° C refrigerator. Prior to performing glucose measurements, the electrodes were first allowed to acclimate to room temperature, then submerged into a negative control of 1x pH7.2 phosphate buffered-saline (PBS) for 30 seconds. The 30 second wait time was normalized across each glucose concentration prior to electrochemical measurement. Cyclic voltammetry (CV) was performed to identify the peak current response from the sensor, which was verified with a chronoamperometry (CA) utilizing the excitation bias at which the peak current response occurred (V_B = -0.1 V). For specific details of the experimental protocol please refer to Appendix A.

Electrochemical characterization was performed with the BioLogic potentiostat, to generate concentration curves for the GOx electrodes. For these sets of experiments the concentrations of the glucose solutions were chosen to reflect glucose

ranges described in the datasheet reported by the manufacturer [113]. The targeted glucose concentrations include PBS alone (i.e., 0 M glucose), 10 μM, 100 μM, 200 μM, 500 μM, and 1 mM. The findings are summarized in the calibration curve below (Figure 2-3A). In order to eliminate any doubt from the instrumental setup correlated to the poor linear fit of the glucose electrode, electrochemical measurements were performed with a chemical which exhibits Nernstian behavior, potassium ferrocyanide ($K_4Fe(CN)_6$), using a commercial 2.0 mm diameter bare gold electrode (DropSens). These electrodes differed slightly in size, though could be fitted into the same card edge connector. Calibration curves were generated similarly to the glucose measurements above, however, a linear fit showed a much improved and predictable response (Figure 2-3B).

Since the reference electrode of the AC1.GOx glucose sensor was pure silver and not silver/silver chloride, it was susceptible to a slight voltage shift over repeated measurements. This behavior was monitored by using a separate control solution of only PBS. The PBS and glucose concentration measurements were performed in parallel under the same excitation conditions to determine if the glucose was assisting this voltage shift. On the contrary, the solution with glucose at any concentrations remained reasonably stable, and significant shifting only occurred in the control PBS solution, due to the lack of discernable voltage peak. The only noticeable change found in the target solution was an initial shift when moving from PBS to the lowest concentration, signifying that the reduction peaks associated with glucose were well characterized.

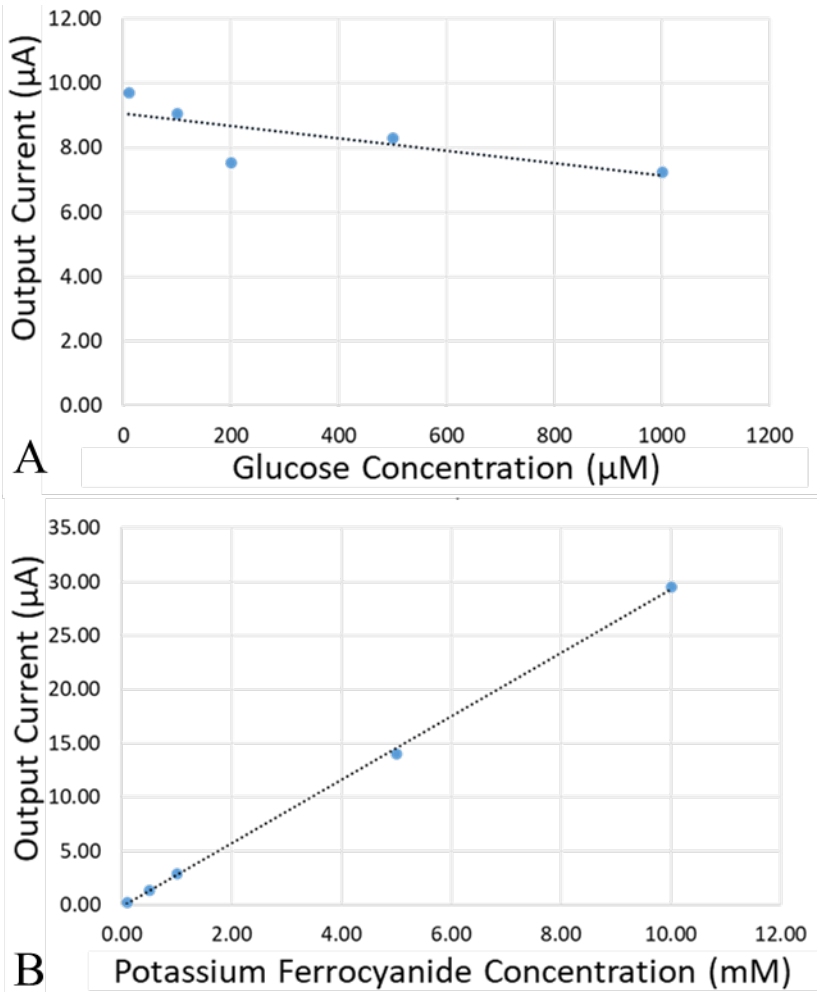

Figure 2-3. Concentration curves for commercial screen-printed electrodes. A) GOx sensor in glucose solutions and B) bare gold sensor in several $K_4Fe(CN)_6$ solutions, ranging from PBS, 10 µM, 100 µM, 200 µM, 500 µM, and 1 mM .

CA and CV measurements of glucose performed using the Biologic potentiostat were later compared to measurements taken using the LMP91000, however the results were not able to confidently reflect an accurate reading of glucose concentration after many repeats. Several factors may contribute to this, including the possibility that the glucose concentrations were too high (~10 mM) and caused sensor saturation, even though the concentrations were chosen in reference to the manufacturer provided

calibration curves. Additional parameters such as equilibration time, temperature acclimation, reference electrode shift, and measurement duration were all modified in the attempt to extend electrode lifetime. However, the PalmSens electrodes presented limited effectiveness towards the measurement of glucose beyond one time use applications, which would have been detrimental for integrating with the bPod. The utility of these electrodes lied instead in measurement of more standard and predictable analytes with clear oxidation peaks, such as $K_4Fe(CN)_6$, which has an oxidation peak at 0.22 V, to compare readings from the benchtop potentiostat (BioLogic) to the LMP91000.

In summary, commercial screen-printed electrodes provided the necessary background for the design of the fabricated DO sensor, and assisted in fine tuning methods for evaluating electrochemical properties of the sensors. Specifically, investigation of a commercial glucose sensor highlighted the advantages of the 3-electrode Clark-type topology, as well as design considerations for the surface areas of the working electrode, which could be directly applied to the fabrication of the oxygen sensing electrodes. Not only is robustness and response time of the sensor important, but the electrochemical sensor lifetime must last for the duration of the bioprocess monitoring application.

2.2.2. Dissolved Oxygen Sensor

Electrodes for the detection of dissolved oxygen were fabricated on top of a Pyrex™ substrate. Each individual sensor was 9.0 mm in width and 20 mm in length with a contact pin pitch of 2.54 mm. These dimensions allowed the sensors to interface

with the electronic module through a card edge connector, which had a 10 mm x 8 mm cavity for positioning of the sensor, as well as to provide enough spacing (13.7 mm) between the contact pads and sensor area for the addition of leak-proof fittings. Similar to several commercial glucose sensors, the WE electrode was designed to have 4.0 mm diameter. The surface area of the CE compared to the WE was designed in a 2:1 ratio.

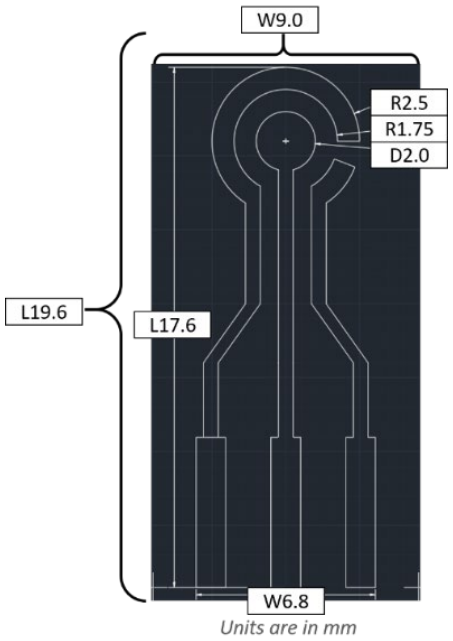

Figure 2-4: Schematic detailing the dimensions of custom DO sensor drawn in AutoCAD. Length and width were determined to interface with a card edge connector (CEC) and the electronic module.

2.2.3. Electrode Fabrication

This section describes the design and fabrication of the electrochemical DO sensor. All fabrication was performed at the UMD Nanocenter and its Fablab.

Mask Creation

Due to the millimeter scale geometry, paper shadow masks provide sufficient spatial resolution of the electrode pattern. Two shadow masks were drawn in AutoCad and then laser cut into cleanroom paper using an Epilog laser cutter, shown in Figure 2-5A and 2-5B. The first mask was used for patterning gold onto a Pyrex substrate for formation of the working and counter electrodes. A second mask was used to pattern silver onto the reference electrode. Laser raster speed and power output were adjusted to improve the resolution and to completely cut through the cleanroom paper. The resolution of the laser cutter was found to be 100 μm, thereby limiting the smallest feature sizes for the electrode traces. Each mask design included 24 sensors oriented to maximize the surface area coverage on the 100 mm diameter wafer. Alignment marks were added for dicing and metal deposition steps. A critical challenge of using a paper mask is affixing them directly to the surface of the wafer, avoiding gaps between the mask and the wafer which will slightly alter the width of the resulting electrode pattern. To overcome this, spaced rectangular cutouts were added to the mask for taping directly to the Pyrex substrate. Despite this effort to enhance paper mask adhesion to the substrate, any loss of adhesion can impact the clarity of the e-beam patterned features. For example, the paper masks can tend to curl away from the wafer surface, and since e-beam evaporation is highly directional, this may result in some elongated or cutoff electrodes. Sources of this error can result from the placement in the substrate holder, which if the mask was not sized properly would introduce minor folding, and the limited adhesion of the tape while inside the e-beam evaporator. Additional challenges associated with the laser cutting includes accumulation of burn marks (rough edges) on

the paper, which lead to non-uniform features on several of the patterned electrodes on the wafer.

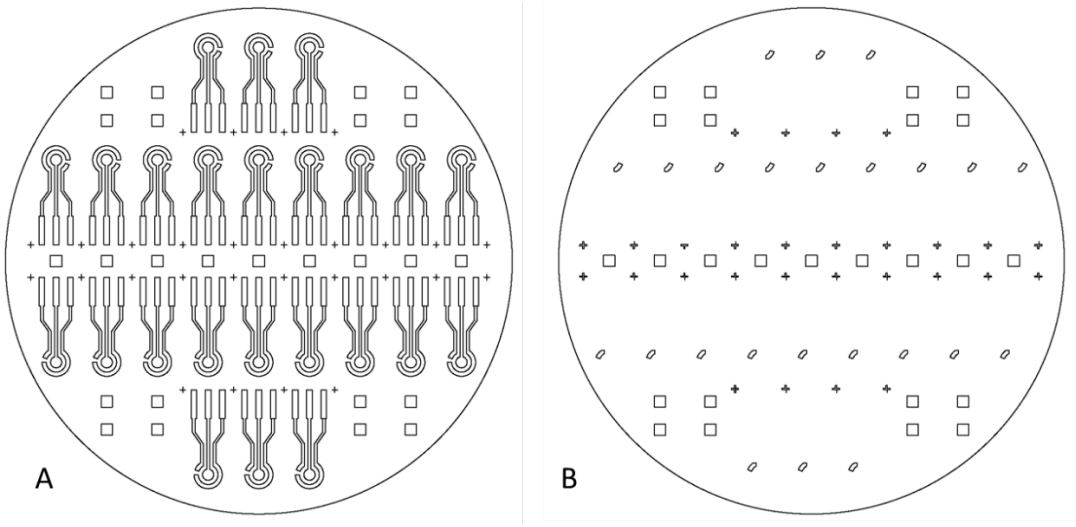

Figure 2-5. Mask design for electrode patterning for A) Cr/Au deposition and B) Ag deposition.

E-beam Evaporation

The three-electrode sensor with a thin-film 4 mm diameter gold working electrode, gold counter electrode, and a silver reference electrode was fabricated as depicted in Figure 2-6. Cr/Au (20 nm/200 nm) layers were deposited using e-beam evaporation, followed by deposition of Ag (250 nm) onto the patterned reference electrode. As mentioned, the deposition pattern was created via two separate laser cutting steps (Epilog Laser Fusion) and the cleanroom paper masks were affixed sequentially to the Pyrex wafer. The alignment of the subsequent Ag mask to the initial Au patterned electrodes was performed by manually aligning the cross features on the mask through the backside of the wafer, aided by the transparency of the Pyrex substrate. After deposition, the masks were removed and the wafers were cleaned with

a combination of acetone, methanol, and isopropanol (AMI), followed by rinsing with DI water and drying with nitrogen gas. The wafers were then prepped for dicing by spin coating a thin layer of Shipley S1813 positive photoresist (Micro-Chem, Westborough, MA) to protect the wafer from dust and debris during the dicing process. This procedure was completed using the Model P-6708D 8" spin coater. Spin parameters are summarized in Table 2-1 below. The wafer was then diced into individual sensors (9 mm x 19.6 mm) using the dicing saw (Microautomation, Centreville, VA). A 100 μm thick perforation was leftover following the dicing process such that the sensors could be stored and then separated when ready for assembly. The yield of the fabrication process was roughly 20 electrodes per wafer, due to variations in the coverage of the reference electrode and cracking of the substrate when separated individual sensors. To remove the photoresist layer, the electrodes were once again cleaned using the AMI process and rinsed with DI water.

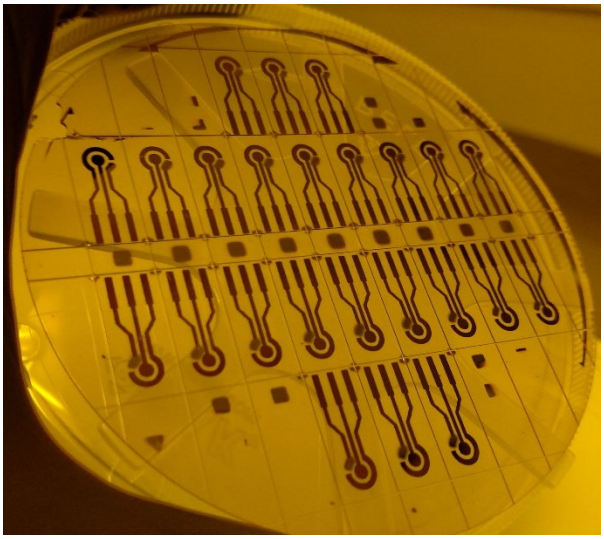

Figure 2-6. Photograph of fabricated Clark-type sensors with gold working and counter electrodes, and a silver reference electrode.

Table 2-1. Spin parameters for deposition of photoresist to achieve desired thin film thickness for wafer dicing. Wafer was baked for 100 seconds at 100° C on a hotplate following spin coating.

RPM	Ramp	Time
RPM1 = 100	Ramp1 = 1 s	Time1 = 1 s
RPM2 = 1500	Ramp2 = 1 s	Time2 = 5 s
RPM3 = 2000	Ramp3 = 2 s	Time3 = 40 s
RPM4 = 0	Ramp4 = 3 s	Time4 = 0 s

Preparation of the Ag/AgCl Reference

Once cleaned, the reference electrode (RE) was functionalized to have a Ag/AgCl surface layer. This was done to ensure a stabile voltage peak for the reduction of dissolved oxygen. The Ag/AgCl REs were prepared using a 50 mL solution of 50 mM Ferric chloride to create an AgCl layer [60]. Electrodes were dipped into solution for about 5 seconds as the electrode underwent a change in color from silver to black. The electrodes were then rinsed in two separate DI water petri dish baths to minimize contamination of the rinses and to completely remove the ferric chloride. Following this process, all sensors were cleaned using AMI. Following Ag/AgCl RE fabrication, characterization of the reference potential for stability and voltage level was conducted, as will be discussed in Chapter 4 of this thesis. However, it was found that Ag REs will spontaneously produce an Ag/AgCl surface when under KCl solution, which is the electrolyte used for DO sensing by the Clark electrode. In fact, the ferric chloride treatment often removed too much of the silver layer and significantly reduce the lifetime of the sensor.

2.3. Electrochemical Cell

The electrochemical cell consists of three main components: a sensor, an electrolyte solution, and a gas permeable membrane. The fundamentals for electrochemical cells were discussed in the literature review (section 1.3.2), however here the chemical reaction with oxygen enabled by the presence of the electrolyte is explained. Potassium chloride is a salt that dissolves easily in water and dissociates into K+ and Cl- ions. These ions support the transfer of electrons between the electrodes, making the electrolyte more conductive. The KCl concentration utilized for DO sensing may vary slightly or include additional molecules such as glycerol to support electrochemical reactions, but typically KCl is used in a 0.1 M concentration.

What distinguishes the Clark cell is the use of a gas permeable membrane. In solution, the difference in the O_2 partial pressure gradients between the electrolyte solution in the well and the external solution will cause the diffusion of O_2 through the membrane. The proposed membrane for the bPod is a 25 μm thick FEP membrane purchased from Strathkelvin. As expected, the O_2 molecules diffuse from a high to low pressure until a system equilibrium is achieved. This introduces two diffusion regions that dictate the ability of the sensor to detect changes in the external DO saturation and affects the response time of the sensor: diffusion across the FEP membrane, and within the KCl electrolyte. Therefore, the response time of the measurement of DO is diffusion limited and dependent on diffusion between the outside of the FEP membrane and electrode surface where the electrochemical reaction takes place. To allow for sufficient transfer of DO into the electrolyte chamber, the diffusivity of the FEP membrane is determined by its thickness, hydrophobicity, and pore size. Identifying

the FEP membrane or the electrolyte as the diffusion limiting region will guide targeted improvements can be made to the electrochemical cell.

For the bPod, the chemical reaction of the Clark-type electrode can be summarized as follows:

$$O_2 + 2H^+ + 2e^- \rightarrow H_2O_2 \quad (2\text{-}1)$$

$$H_20_2 + 2H^+ + 2e^- \rightarrow 2H_2O \quad (2\text{-}2)$$

In reference to Figure 2-7 oxygen diffuses through the FEP membrane until an equilibrium is reached with the external solution. An excitation bias is applied between the WE and RE while electrons are provided by the counter electrode. The gold working electrode in this system is inert and does not interfere with the reaction, and will only accept and pass electrons to reduce O_2 at the working electrode surface into hydroxide ions, thus producing a current which is proportional to the partial pressure of oxygen [55]. Additional bi-products in a KCl solution are found when the K^+ ions pair with the excess OH^- and the Cl^- pair with Ag(s) to form KOH and AgCl, thus oxidizing the RE surface. This can be observed visibly as the reference electrode surface darkens overtime, signifying the degradation of the electrode, which can result in a lower unstable current response for the sensor that is unable to be calibrated.

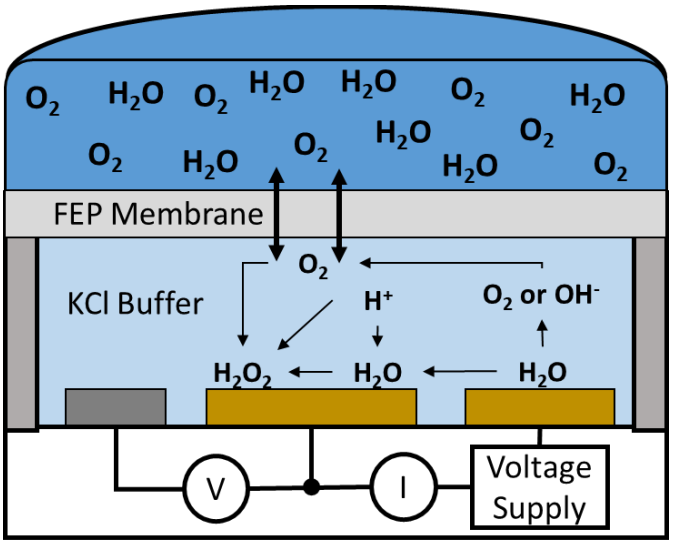

Figure 2-7. Cross-sectional diagram of the chemical reaction for the Clark-type electrode. The oxygen reduction reaction is represented using a three-electrode system with gold WE and CE, and a silver RE.

2.4. Attachment of FEP Membrane

Three generations of the sensor and membrane attachment to form the electrochemical cell have been explored, to date. Each generation highlights a distinct assembly strategy to achieve the goal of providing a gas permeable, liquid impermeable barrier between the external solution and internal electrolyte well. With each modification, the thickness and complexity of the Clark cell was reduced, which correlated with improved electrochemical measurements due to reduced time of O_2 diffusion. The three generations can be summarized as 1) an extrusion from main 3D-printed packaging body, 2) a separate 3D-printed well for each individual sensor that is inserted into the main body, and 3) an electroplating tape-based well that directly interfaces with the sensor substrate. The design motivations and commentary for the assemblies will be discussed below.

2.4.1. 3D-Printed Screw-top Sensor Interface

The first attempt to construct the electrolyte well (potassium chloride electrolyte) focused on modification to the main 3D-printed packaging. Though this would increase the complexity of the design significantly, it offered several noted advantages compared to assembling the electrolyte well during the fabrication process or individually for each sensor. In this manner, the same bPod enclosure could be used repeatedly without permanent sealing, by simply inserting a sensor into the packaging and screwing down the top with two screws, as shown in Figure 2-8A. Additionally, a variety of electrolyte concentrations and composition could be quickly loaded and reloaded into the well and the gas permeable membrane could be applied in an efficient manner, without formation of bubbles that would skew DO measurements. Figure 2-8 shows several images of the generation 2 of the 3D-printed enclosure, which will be covered in detail in Chapter 3. The gas permeable membrane is attached to a 5 mm opening using an O-ring. The relevant dimensions of the sensor interface include a cylindrical electrolyte well of height 7 mm (the distance between the FEP membrane and the electrode surface) and a diameter of 5 mm created by two concentric O-rings used for leak-proof sealing as shown in Figure 2-8B.

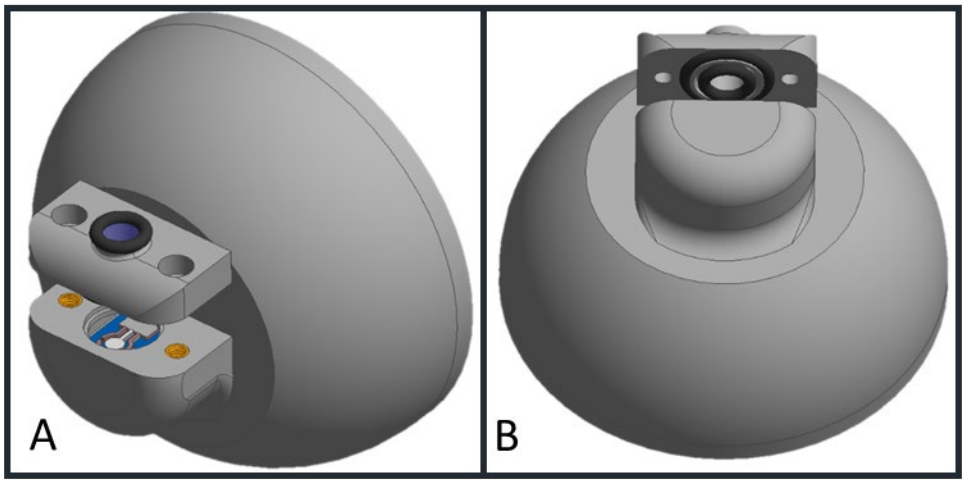

Figure 2-8. Generation 2 of bPod enclosure incorporating the 3D-printed screw-top interface and membrane attached using an O-ring. A) Highlights the thermoset inserts, placement of the electrode, and the sealing of the FEP membrane with a 5 mm O-ring. B) Shows the concentric O-ring feature used for creating a leak-proof seal.

However, the interface resulted in issues with leaking into the main body of the bPod at sparging system pressures, which are on the order of 10 – 50 mmHg [114]. This was attributed to ill-fitting O-rings and slight bending in the 3D-printed parts resulting from the placement of the screws between the two 3D-printed pieces. Leaking issues were overcome with several iterations of the 3D-printed screw-top sensor interface as well as application of epoxy. Another concern with the electrolyte well integrated into the 3D-printed package was the distance between the FEP membrane and the surface of the sensor. This distance was found to be non-negligible, and in fact was the predominant source of diffusion limited behavior as sensor response times were observed on the order of 10-15 minutes during integrated testing of the bPod. Experiments even showed at times that there were no changes in the CA current signal between a nitrogen purged state (0% DO) and a fully oxygen saturated state (100% DO) due to prohibitively slow diffusion across the 7 mm electrochemical well

thickness. While leaking issues were solved, the dimensions of the electrochemical well needed to be decreased in the subsequent generation.

2.4.2. 3D-Printed Receptacle Sensor Interface

The electrochemical well was redesigned to minimize the electrolyte chamber volume, hence reducing the distance between the FEP membrane and the gold WE. To accomplish this, a 3D-printed receptacle, as shown in Figure 2-9, was designed such that the sensor could be inserted and fixed with epoxy. This was a shift in design philosophy as the modifications were conducted individually for each sensor as opposed to just the main bPod enclosure. The relevant dimensions for the 3D-printed cover are as follows: the length coincides with previous iterations and is 21 mm in total with 20 mm accounting for the cavity, the diameter of the circular opening was 8 mm, and the opening was 10 mm x 0.75 mm giving a 0.25 mm tolerance for inserting the sensor. The 8 mm opening was chosen to maximize the surface area of the FEP membrane. To create the electrolyte well, the sensor was inserted into the 3D-printed part and epoxy was applied along the circumference of the circular junction between the glass substrate and the MED610 part. After drying for 5 minutes, the top of the part was covered with a thin layer of epoxy along three of the edges and a 10 mm x 10 mm square cutout of FEP membrane was attached. Then 1 mL of 0.1 M KCl was pipetted into the well through the unattached side of the FEP membrane, ensuring that no bubbles were formed. Finally, the last edge of the membrane was sealed to the 3D-printed receptacle with epoxy.

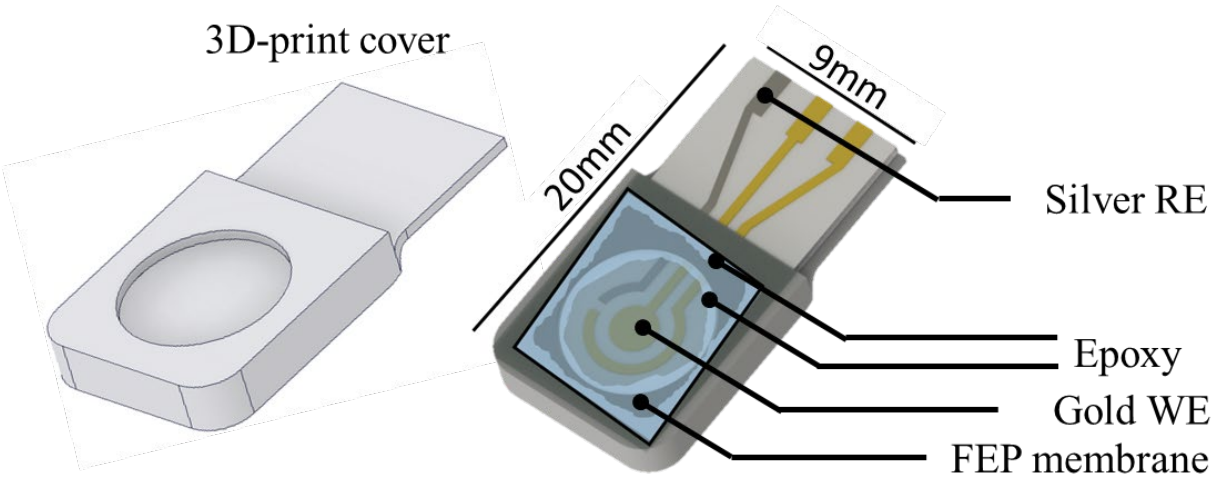

Figure 2-9. Conceptual drawing of the 3D-printed receptacle sensor interface. The electrochemical well was formed by trapping 1 mL of KCl onto the sensor surface with an FEP membrane and epoxy.

The advantage of this approach was seen in the greatly reduced complexity of the overall enclosure design; however, the assembly time of each sensor was also increased to account for three separate applications of epoxy. Though noted success in measurements with this sensor configuration will be discussed in Chapter 4, issues arose regarding the sensor assembly lifetime. This design left very few options for refilling the electrolyte solution, and the KCl solution tended to evaporate over time unless the sensor was stored in a DI water solution. Another disadvantage was the lack of control over the spread of epoxy. During testing of the device, the epoxy may have partially covered the sensor electrodes, reducing the effective surface area of the sensing electrodes, thus lowering the electrochemical response. In addition, wicking of the epoxy along the FEP membrane could also lead to substantially lower response times and long wait times in order for the dissolved oxygen to diffuse through the membrane. As a result, the inconsistency of this design generation required further

innovation of the sensor interface that would minimize application of epoxy and speed up assembly times.

2.4.3. Tape-based Sensor Interface

The tape-based sensor interface for containing the electrolyte solution above the Clark-type sensor was fabricated as using Type-490 electroplating tape (3M), as seen in Figure 2-10. Two pieces of electroplating tape were cut to form a circular well (5 mm diameter/25 μm height) using a biopsy punch. The first layer was attached directly to the glass substrate, containing the electrolyte solution, then 10 μL of electrolyte solution (0.1 M KCl) was pipetted onto the electrode surface. To entrap the electrolyte solution, a small square (8 mm x 8 mm) of the 25 μm thick FEP membrane was attached to the second piece of electroplating tape and then carefully attached to the first layer, such that no bubbles were trapped in the well. This method of encapsulation was used to minimize the distance between the FEP membrane and the sensor surface, ensuring that only diffusion through the FEP membrane would limit sensor response time [115]. To prevent evaporation of the electrolyte solution through the FEP membrane, the sensors were stored in DI water between successive measurements.

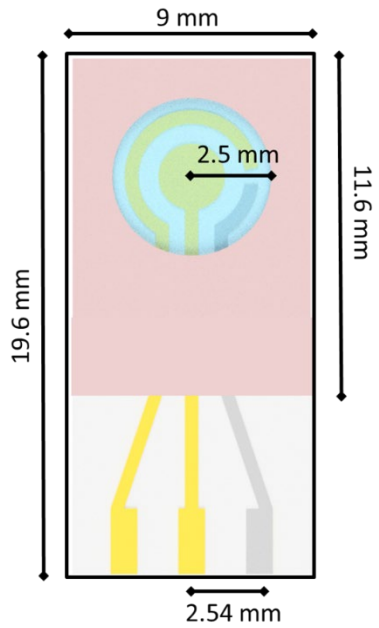

Figure 2-10. Schematic of the tape-based DO sensor.

Having addressed the assembly challenges from previous generations of the sensor interface, this iteration proved to be effective for the measurement of dissolved oxygen. By replacing the 3D-printed part with electroplating tape, the cost and assembly time per sensor was greatly reduced. Additionally, the simplicity of the modification provides a clear path towards scaling down the sensor size without needing to redesign an entire accompanying interface. Several aspects of the sensor assembly can be improved. The electroplating tape at times can remove the metal traces if not applied properly and the current application is limited to a single process flow, such that sensors are assembled manually one at a time. However, this electroplating tape method does lend itself to wafer level assembly in the future by using appropriately laser cut materials. The tape-based FEP attachment scheme offers a highly adaptable method for creating an electrochemical well, using a minimal amount of electrolyte

solution, hence the diffusion limited properties of the chemical reaction become entirely dependent on the physical characteristics of the gas permeable membrane. Extensive use of this assembly will be discussed in the following sections.

Chapter 3. bPod Platform Design and Assembly

3.1. Electronic Module

Several considerations for the design of the electronic module to achieve real-time wireless sensing in an aqueous environment were explored. Among these were low power consumption, small form factor, sensor calibration, and robust device to device communication. In Figure 3-1, the overview circuit schematic is shown, outlining the connections between the electronic components. The electronics system contains a (1) BLE 4.0 microcontroller for data processing and transmission to an external user device, such as a mobile phone or laptop, (2) an analog-front-end (AFE) portable potentiostat readout circuit to bias and read the signal from the electrochemical sensor, (3) a single 3.7 V lithium polymer (Li-Po) battery with 14 mAh capacity and 30 mA maximum discharge current, and (4) a linear voltage regulator to stabilize and step-down the battery output to 3.3 V for each of the electronic components. Finally, the electronic module is attached to a 2.54 mm pitch card edge connector (CEC) in order to interface with the DO sensor assembly.

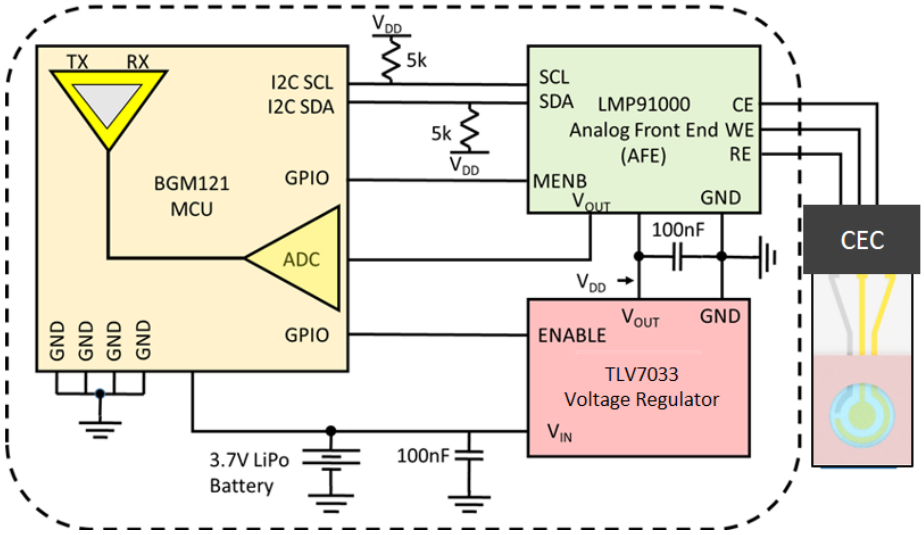

Figure 3-1. Schematic of readout circuitry employed in smart marble design for electrochemical measurements.

3.1.1. Potentiostat IC - LMP91000

The readout circuit for this application consisted of a single AFE potentiostat integrated circuit (IC), namely the LMP91000 from Texas Instruments. This IC, though primarily designed for gas sensing, was instead operated for the amperometric measurement of DO, and has been demonstrated in numerous portable miniaturized analytical devices [13], [116].

As discussed in section 1.3.3, the desired sensor configuration consists of three-electrodes: a working electrode (WE), a reference electrode (RE), and a counter electrode (CE). The primary function of the potentiostat IC is to directly interface with the sensing electrodes, providing both a stable voltage bias across the WE and RE to stimulate an electrochemical reaction, as well as to convert the current response to an analog voltage. To better understand how the LMP91000 functions, it is best to divide the device into several operational blocks. These include a control loop, a

transimpedance amplifier (TIA), temperature sensor, and an inter-integrated circuit (I^2C) interface as shown in Figure 3-2.

The control loop, denoted by the A1 op-amp in the schematic, is connected as a voltage buffer, utilizing negative feedback to equate the DC voltages at the non-inverting and inverting pins of the op-amp. In this way the potential applied by the voltage regulator will show up at the reference electrode, while the CE provides the necessary current to stabilize the voltage. The TIA, which is typically rated for low input current noise, will measure the current output from the WE and convert it to a voltage. Depending on the value of the feedback resistor, this value will be amplified to observe changes at various current scales. The I^2C interface allows for much of the device functionality to be controlled by an external microcontroller (MCU), which specifically includes adjusting the variable bias point of the RE, modulating the gain from the TIA, and toggling the device into a low power sleep mode [117].

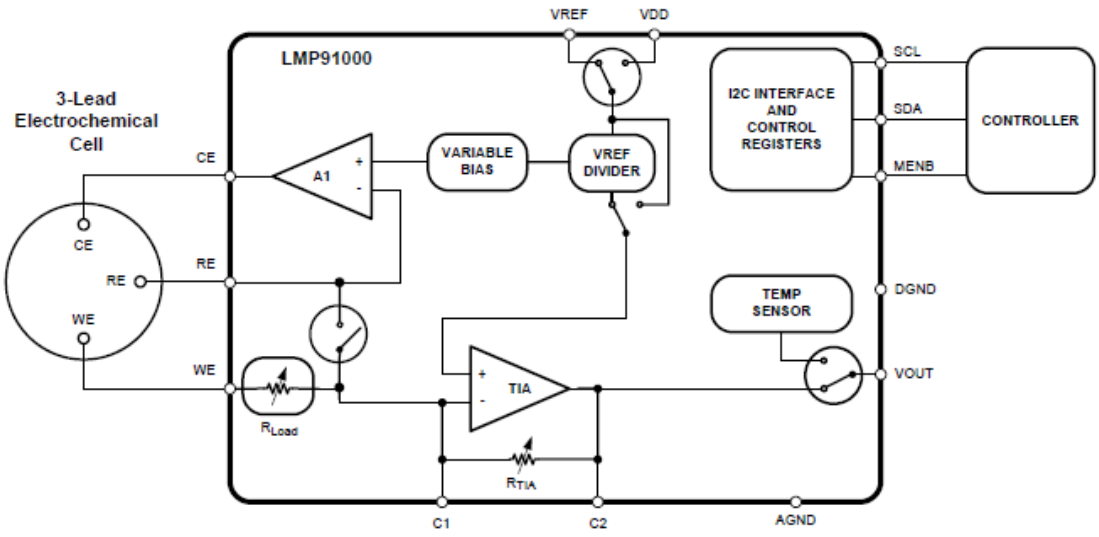

Figure 3-2. Schematic diagram of LMP91000 AFE from Texas instruments [50].

3.1.2. Microcontroller Unit (MCU)

Bluetooth Low Energy (BLE) Module - BGM121

Compared to other wireless modalities, BLE boasts a small form factor and low-power consumption at high data rates and easy integration with user devices such as smartphones. The Silicon Labs BGM121 SiP chipset (6.5 mm x 6.5 mm x 1 mm) was chosen for this application and includes a programmable microcontroller, an integrated 2.45GHz transceiver antenna, and a flash memory unit. The internal inverted-f antenna provides an adjustable +8 dBm transmission signal at a 2.45GHz excitation frequency. To correct for detuning due to the surrounding media, the length of the antenna ground plane may be modulated; an increase in the length corresponds to a decrease in the resonant frequency and a shortening of the ground plane results in an increase in the resonant frequency [118]. The BGM121 utilizes the Low-Energy protocol described in the Bluetooth 4.0 specifications with a footprint of 6.5 mm x 6.5 mm and a height of 1.0 mm. For development of the prototype the BGM121 radio board, a pre-soldered PCB with a sufficient ground plane was used. The PCB allows the design and verification of the rest of the circuit components as well as the DO sensor without having to design an RF PCB layout for the internal antenna.

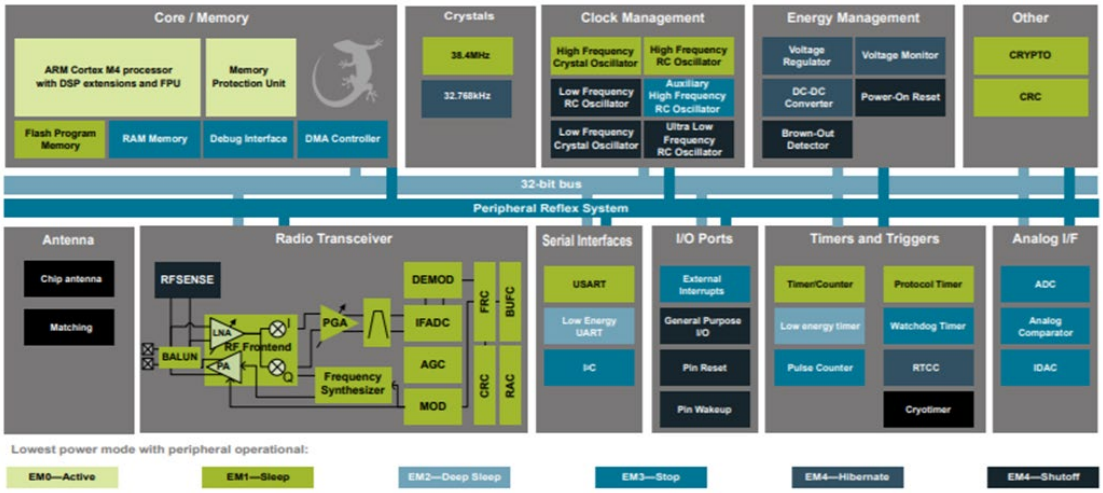

Figure 3-3. Schematic of available peripherals for the BGM121 microcontroller. Each function is colored to correspond to the energy mode necessary for its use. Ports are defined as letter blocks and allow programmable access to the device peripherals [80].

The core peripheral and energy mode operational guidelines for the BGM121 are shown in Figure 3-3. The available peripheral pinouts include a 10-bit analog-to-digital converter (ADC) for digitizing sensor data, several general-purpose input-output (GPIO) pins used for toggling the enable pins of electronic components, and two I^2C lines allowing bidirectional communication between the LMP91000 and the BGM121. One of the GPIO pins toggles the I^2C enable on the LMP91000, which allows I^2C communication when the value is low. The bPod relies on I^2C to configure the LMP91000 to handle a variety of sensor types and excitation biases. Further information regarding the I^2C operation and the communication between the BGM121 and LMP910000 can be found in Appendix A. The other GPIO pin toggles the capabilities of the voltage regulator connected to the LMP91000; when low, the voltage regulator will simply pass the battery voltage. Doing this reduces the power

consumption of the voltage regulator. Three pins: PF0, PF1 and RESET are used to program the microcontroller along.

Energy Modes

The BGM121 utilizes several energy saving modes to control current consumption depending on the required function, thus extending the operational lifetime of the device. When transmitting and receiving data, the device enters an "active" mode and draws 25 mA of current. While idling for an event interrupt to occur, the device is set to "deep sleep" mode where it consumes 2.5 μA and can also enter a temporary shutdown of the device using "hibernate" mode consuming 0.58 μA.

To verify the successful transition into the different energy modes of the BGM121, the circuit was connected to the Simplicity Studios Energy Profiler. This utilizes current measurement circuits on the Silicon Labs wireless starter kit (SLWSTK6101C), or WSTK, and the computer program to measure the current consumption from the microcontroller. Figure 3-4 shows one iteration of the measurement sequence. The sequence can be customized for the timing of the DC bias and setting of the correct energy modes. The energy modes in the figure are denoted EM1 (high energy mode for data acquisition with the UART), EM2 (sleep mode while the device is waiting for an event), and EM4 (shutdown – everything is off except for a cryotimer that will reset the device to reinitialize and start again). The measurement sequence is described by the following modes: DELAY (wait to start measurements), STANDBY (LMP91000 wakes up and the configuration is switched to a zero bias), BIAS (-0.5 V voltage bias applied between the working and reference electrodes),

ZERO (bias returned to zero), SLEEP (LMP91000 put to sleep and UART communication stopped), and OFF (most functions disabled for extended hibernation).

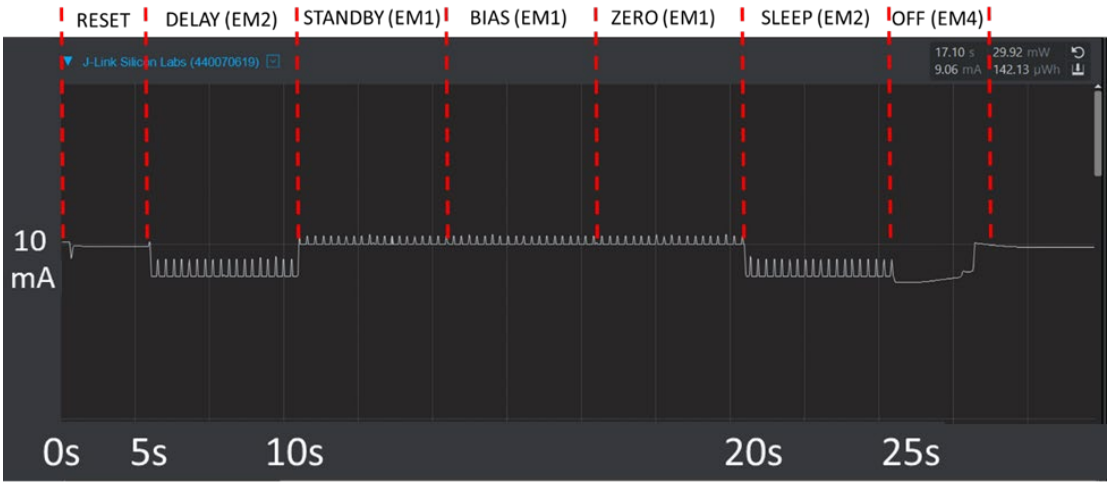

Figure 3-4. Energy profile of the BGM121 using Simplicity Studios Energy Profiler. Spikes represent data pulses, while the overall shifts indicate the switching of the energy mode.

Debugging of the MCU

Programming of the BGM121 was performed using the Silicon Labs IDE, Simplicity Studios 4. Debugging of the electronic module was performed either by connecting the BGM121 radio board directly to the starter kit, or by attaching 24-gauge wires directly to the programming pins. A Simplicity Debug Adapter (SLSDA001A) was connected to the starter kit and connected with wires to externally flash the code onto the device. The five necessary pins were the Reset, SWDIO, SWCLK, GND, and VDD as shown in Figure 3-5. Throughout the operation of the electronic module new application code is flashed to the device in this manner.

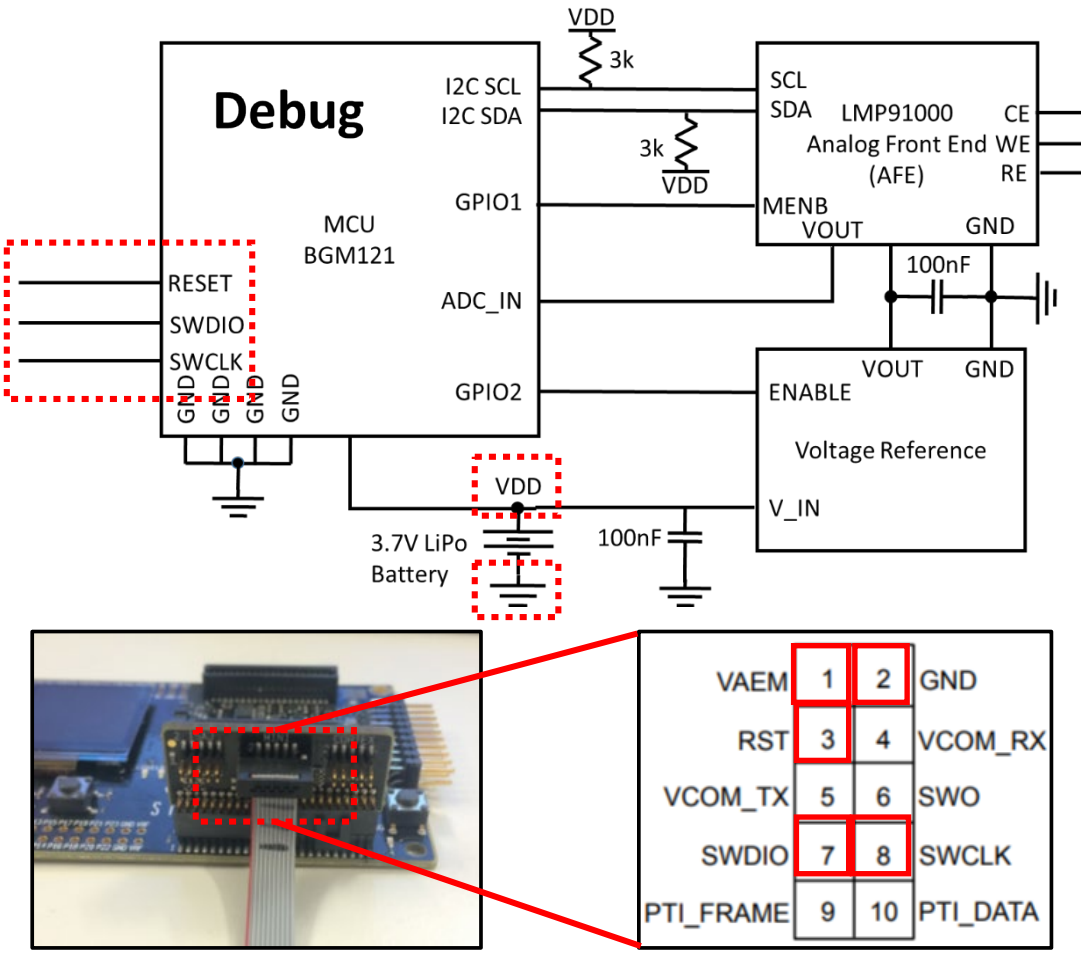

Figure 3-5. Schematic depicting external debugging of the BGM121 using the WSTK. Connections highlighted in red are made between the electronic module and the WSTK.

GATT Profile

For communication between a Bluetooth enabled device, smartphone or PC, and the bPod a GATT profile is generated, detailing how data is exchanged between the two devices. This information is organized into a hierarchy of services and characteristics which contain the data that is to be sent or received. More information can be found in the Bluetooth v5.1 specification manual [119]. There are two main characteristics used for the bPod prototype. The first characteristic, sensor data,

contains the DO measurement and is able to both display the information on the screen, as well as save the information to a .csv file for further analysis. The second characteristic, Command, allows writing data to and the control of the bPod by an external device. This characteristic was programmed to control the operational state of the bPod, defining the energy mode, the calibration, and the on/off state of the device. This will be discussed in detail below. The device name and default appearance are also contained within the GATT profile, as shown in Figure 3-6.

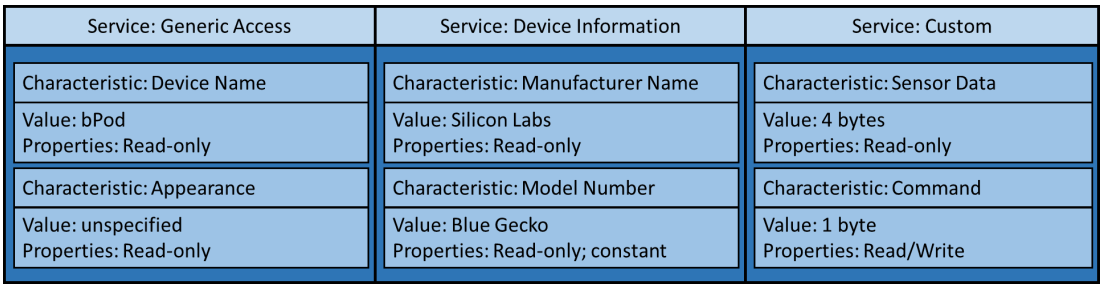

Figure 3-6. GATT profile for bPod device.

There are three services incorporated into the coding of the sensor platform. The first is the "Generic Access" service which includes the device name, such as bPod, as well as an appearance characteristic that associates the platform to known Bluetooth devices, such as a phone, computer, or watch. The second service describes the device information and uses two characteristics. The first characteristic identifies the name of the manufacturer and details about the hardware and software specification. For this device the BGM121 is manufactured by Silicon Labs and is part of the Blue Gecko product line. This is used primarily to determine which version of the Bluetooth software SDK or which hardware revision is currently in use. The final service, as

mentioned previously, is a custom service containing information on the sensor output. This information is represented as the *sensor data* characteristic, which provides the DO concentration transmitted by the sensors as a 16-bit integer as measured by the 12-bit ADC. The values are converted into the appropriate voltage and current units using the exported .csv file in Microsoft Excel (Microsoft, Redmond WA). Since the steady state response time of the sensor can vary, proper conversion requires the use of "For" loops, which lock-up the bPod from transmitting the next data point until the sensor response is complete. The *command* characteristic provides remote access to the bPod, allowing external commands to trigger interrupts and to be used for configuration. The characteristic is an 8-bit write command used to place the bPod into one of four operational states, used to wake the device from sleep mode or shut off for a specific amount of time. These operational states are discussed in detail in the section below

Operational States

The BGM121 microcontroller was programmed to receive commands from a modified BLE app (Silicon Labs) for data acquisition and transitioning the device into multiple operational states. When a command is received by the microcontroller, it enters one of four operational states: OFF, CALIBRATE, MEASURE, and STAND-BY. The default state of the device is triggered by resetting or reconnecting to the bPod through the app, placing the device in low power mode, or EM2. The OFF state places the device into the lowest energy (*hibernate*) mode, effectively turning off the device so that it consumes minimal current. In this mode, the device will disconnect from the phone app and will not receive commands, which is ideal for stopping an incorrect

measurement; an internal timed wake-up event is programmed using the cryotimer to turn the bPod back on after a specific amount of time, which can vary between 1 second and 18 hours. This feature allows the device to remain in the lowest energy mode when not in use, as well as provide a software reset, which can be useful to reinitialize the bPod. Next, the CALIBRATE, or single-shot, state performs a single measurement sequence. This sequence intermittently toggles between the active mode when transmitting data and the low power mode when operating the BGM121 peripherals. Similarly, the MEASURE state will perform the measurement sequence a finite number of times, alternating the configuration of the LMP91000 between the active mode when data is recorded and a three-minute wait period between measurements, where the device is left in low power mode. Finally, the STANDBY state configures the sensor for monitoring the open circuit potential, but does not transmit the data, keeping the device in a low power state. This allows for sensor conditioning if necessary, prior to applying a voltage bias. The generic process flow for the MEASURE operational state is shown in Figure 3-7. By utilizing software timers and external write commands to control the state of the device, the bPod operates autonomously towards the electrochemical monitoring of DO.

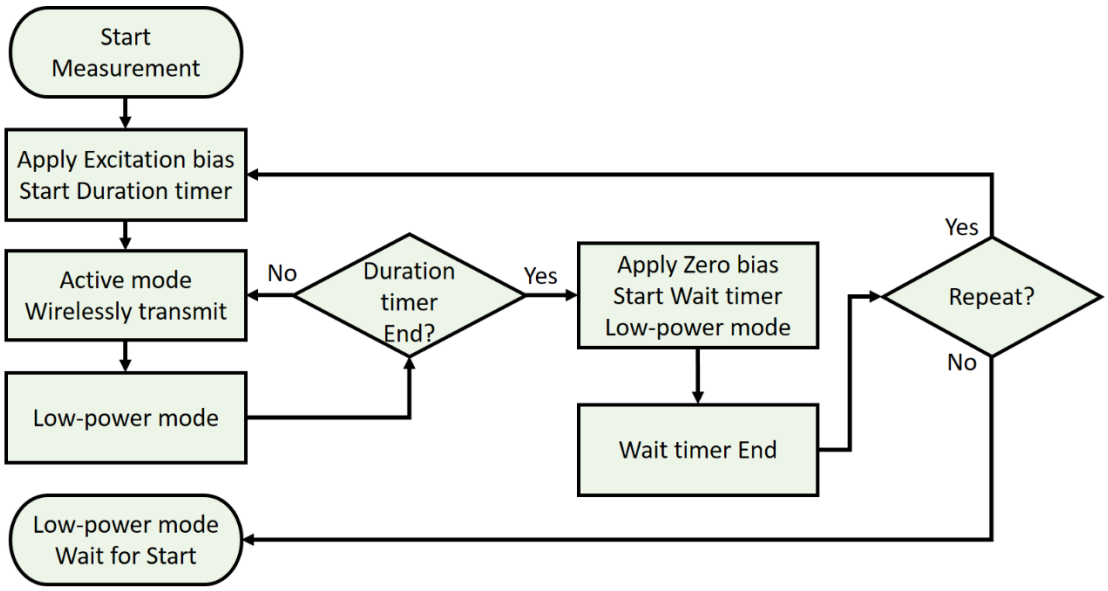

Figure 3-7. Flow diagram for the 'MEASURE' operational state for the bPod. Upon an external write command from the user, internal timers are set to control the BGM121 energy modes and perform amperometric measurements.

3.1.3. Custom Android App

To receive data from the bPod, a custom app was created to send write commands to the BGM121, as well as store and display DO concentrations on the external user device, namely the phone or PC. Figure 3-8 shows the command prompt that allows the user to type in a 1-byte command. The "4" present on the screen (*left*) corresponds to the CALIBRATE state, for example. Next, under the 'Sensor 1' tab (*middle*), the data begins to populate and refresh onto the screen. The measurement from the bPod is both timestamped by the phone and formatted into an Excel spreadsheet (*right*). For future development of the bPod coding, it is ideal to perform all post-processing of the data off of the microcontroller. In this manner, the MCU will be able handle interrupts as they occur to reduce unnecessary power consumption and

time delays in the device, hence reserving the MCU for event scheduling, sensor transduction, enhanced power management, and data transmission.

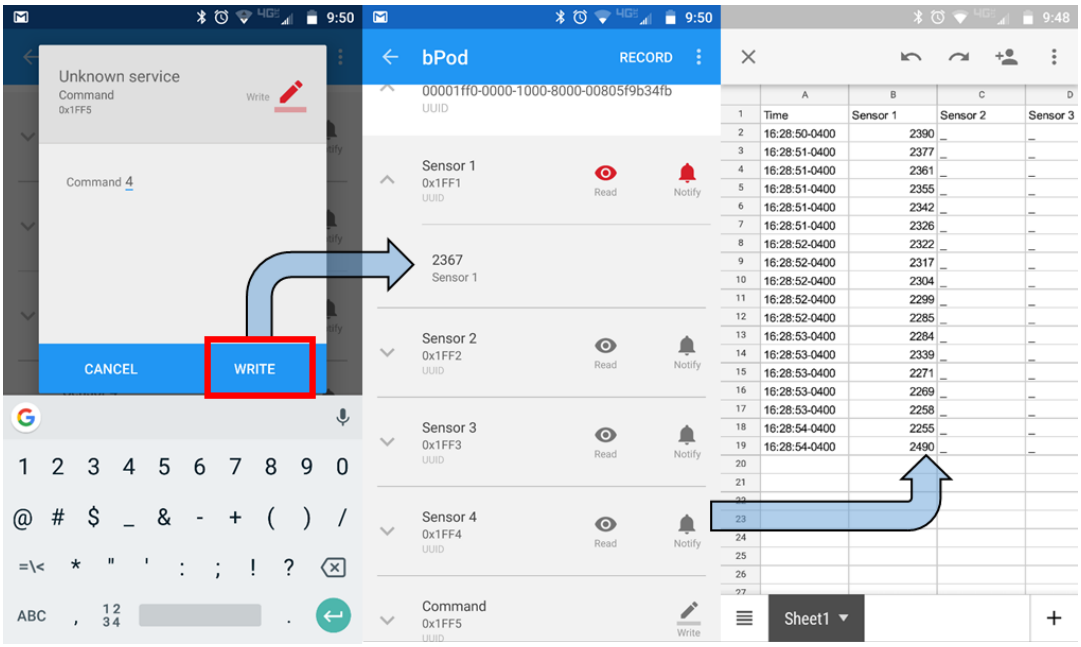

Figure 3-8. Several screenshots of the smartphone app depicting the measurement process from left to right. A command is sent from the phone to bPod (left), then the resulting value is displayed in the app (middle) and stored in a .csv file which can be saved by the user (right). Configuration of data recording interface is credited to Mayavan Sathyam.

3.1.4. Card Edge Connector (CEC)

As discussed in section 1.3.3, interfacing of electrochemical sensors with an electronic module is subject to numerous challenges. A robust connection was necessary for the proper conditioning and measurement of the sensor. The bPod accomplishes this by using a two-sided female 6-position CEC with pin pitch of 2.54 mm (TE Connectivity), ensuring tight physical connections between the electrode contacts and electronic module (Figure 3-9). Therefore, multiple sensors could easily

be connected and disconnected to a singular platform (electronic module) without using other processes such as wire-bonding or soldering to make the sensor connections. The bPod utilizes 3-pins at a given time and the connections are attached directly to the WE, RE, and CE inputs of the LMP91000. The dimensions of the CEC are 14 mm x 10 mm x 8 mm with an acceptable card thickness of 1.37 mm – 1.78 mm. Due to these size parameters, the DO sensor dimensions were required to be of sufficient length and width for inserting into the adapter, as well as thick enough to maintain proper contact. The specifics regarding the sensor fabrication dimensions were discussed in Chapter 2. The Pyrex sensor substrate (500 µm thickness) was susceptible to dislodging from the adapter, therefore additional spacers were needed to supplement the connection between the CEC contacts and those of the sensor.

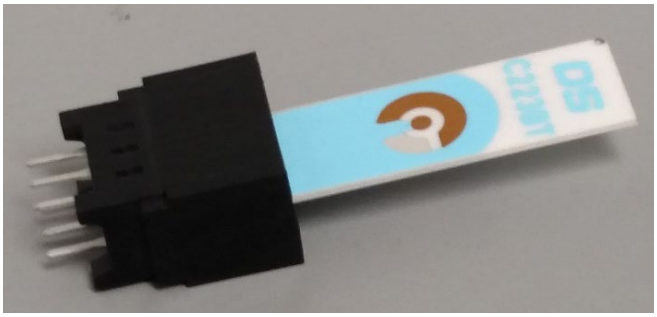

Figure 3-9. Double sided 2.54 mm pitch edge connector with commercial sensor.

3.1.5. 3D-Printed Spacer

For each generation of the 3D-printed enclosure, the electrochemical DO sensor was supported by a 3D-printed spacer. The function of this part was to add thickness to the sensor, which ensured a robust connection with the CEC of the electronic module, as well as supported the sensor, making it less fragile during leak-proof

sealing, which was discussed in Chapter 2. The various spacer designs are displayed in Figure 3-10, related to the generation of the bPod enclosure for which they were utilized. Discussion of how the spacers assisted with the creation of an electrochemical well was discussed in Chapter 2. Alternatively, the spacer could have been incorporated into the main 3D-printed enclosure, however, iterative design of tolerances would have proven costly and time consuming.

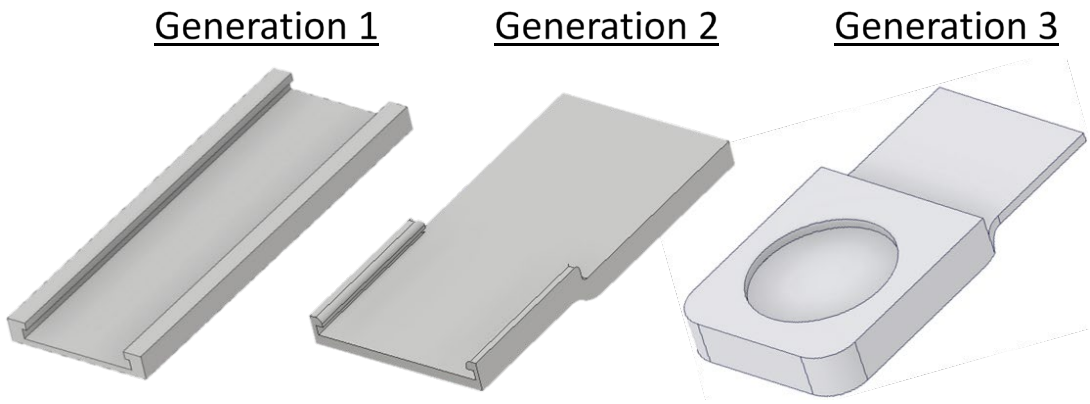

Figure 3-10. Three generations of 3D-printed spacer used for supporting the sensor when interfacing with the bPod.

3.1.6. Power Management

A key consideration for the design of a long-term embedded sensing system is careful power management to preserve battery life. Adequate current was provided to the electronic module to satisfy the power consumption of each measurement processes throughout the bPod lifecycle. The device lifetime is affected by the choice of battery, the power management of the electronic energy modes, and implementing an appropriate duty cycle for bioprocess monitoring. As discussed in section 2.2.3, the operational states were developed to ensure the bPod remains in a low power state unless absolutely necessary. In addition, monitoring parameters such as measurement

duration, sampling rate, and downtime between measurements were modulated to limit power consumption. Therefore, for short- to long-term monitoring, the choice of battery for the bPod would be critical to enable extended monitoring applications.

Battery Selection

The bPod power source must be contained within the packaging, and as such there exists a tradeoff between battery size and capacity. Several common battery chemistries used for portable applications today are silver oxide, lithium/manganese dioxide, lithium/iodine, lithium/ silver vanadium oxide, zinc air, lithium ion (Li-Ion), and lithium polymer (Li-Po) [120]. Silver oxide batteries are frequently used for ingestible capsule research and are based on a silver oxide cathode and zinc anode reaction within an alkaline electrolyte. Despite a small feature size (~10 mm), adequate capacity, and excellent 5-7 year shelf life, silver oxide batteries are not always capable of supplying sufficient instantaneous current for wireless communication [121]. Li-Po batteries based on a polymer electrolyte, however, can provide the necessary instantaneous current and are rechargeable, but do not scale quite as efficiently as silver oxide in terms of capacity to size ratio. Therefore, the prototype bPod utilizes a 14 mAh Li-Po battery (GM301014H) from PowerStream with a 10 mm x 15 mm size for early validation of the system. This battery can supply an average of 3.7 V at up to 140 mA, which are sufficient for powering the electronic module. Bioprocess monitoring within bioreactors may require device lifetimes on the order of a couple weeks, therefore future battery options would ideally be equipped with a larger capacity (>500 mAh).

Voltage Regulator

As the battery discharges, the voltage that it supplies drops. A voltage regulator is needed to maintain constant voltage supply to the embedded system. A TLV7033 linear voltage regulator was chosen for the bPod, which stepped down the 3.7 V input from the Li-Po battery and held the supply rail at a steady 3.3 V for the LMP91000. The BGM121 utilized an internal DC-DC converter, though was eventually also connected through the TLV7033. It was found that variations in the supply voltage to the BGM121, when not regulated, had a significant effect on the ADC resolution, thereby reducing the accuracy of the sensor. This was verified experimentally and explained below.

The BGM121 DC-DC converter supply voltage (V_{DD}) variation was monitored through the ADC to validate this effect of V_{DD} for device measurement. To determine this, a power supply was connected to the device and swept at a 0.1 V interval from 3.0 to 3.7 V, the expected range for the proposed Li-Po battery. It was found that for potentials larger than 3.3 V, the internal DC-DC converter for the BGM121 was unable to maintain 3.3 V, thus affecting the ADC reference voltage. The output voltage of the ADC was configured to output $V_{DD}/2$ shown in Table 2-1 below. The 'actual' value was measured using a multimeter probe placed at the output of LMP91000, whereas the 'measured' value was read from the smartphone. From this experiment, it was determined that the BGM121 internal DC-DC converter was not sufficient for VDD greater than 3.3 V, therefore the MCU power rail connection was moved to the voltage regulator as opposed to connecting directly to the battery.

Table 3-1. This table summarizes the output voltage of the LMP91000 under several different voltage supply rails. The 'actual' measurements were recorded directly from the LMP91000 output, whereas the 'measured' measurements were recorded through the BGM121 ADC.

Applied Voltage (V)	Actual (V)	Measured (V)
3.0	1.619	1.619
3.1	1.620	1.620
3.2	1.620	1.620
3.3	1.620	1.620
3.4	1.627	1.579
3.5	1.627	1.534
3.6	1.627	1.492
3.7	1.628	1.452

3.2. Assembly of bPod Electronic Module

The following section briefly discusses the assembly of the hand soldered electronic module for the bPod. A prototype integrating the various electronics and interface components was developed to identify potential challenges and viability within an enclosed package for underwater testing. Figure 3-11A provides an illustration of the electronic module and the orientation used to fit within the 60 mm bPod enclosure (45 mm cavity).

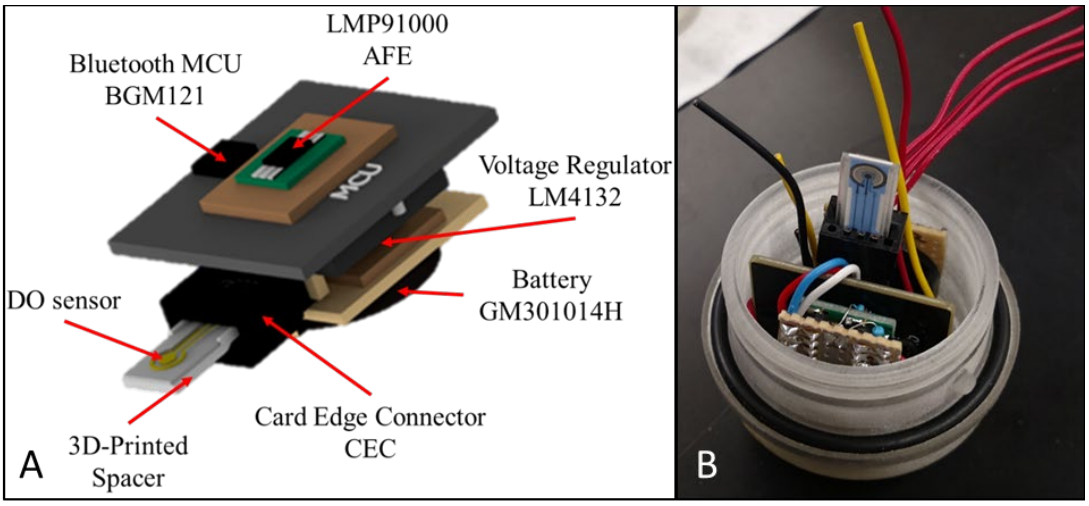

Figure 3-11. A) CAD diagram of the electronic module. The orientation and placement of each system component is modeled and B) arranged to fit inside of the 3D-printed enclosure.

The electronic module consisted of 5 separate components: (1) LMP91000, (2) coin cell battery, (3) linear voltage regulator, (4) the CEC, and (5) the BGM121 radio board. Individual IC's were first validated using the WSTK and LMP91000 evaluation board (LMP91000EVM) [122]. Assembly of the electronic module consisted, first, of soldering each IC to a dual inline-package (DIP) adapter that matched the standard land pattern of each chip. Then, long wires (24 gauge), coupling capacitors, and pull-up resistors were soldered onto an FR4 Veroboard cutout, which has a patterned metal surface with mixed vertical and horizontal metal traces (similar to commercial breadboards). Finally, the DIP adapters were then soldered on top. The FR4 Veroboard were then oriented about the BGM121 radio board such that they directly inserted into the bPod enclosure. The IC's were connected to the BGM121 radio board with 24 gauge wired according to the schematic diagram in Figure 3-1. Finally, wires were trimmed and wrapped around the BGM121. The orientation shown in Figure 3-11B

shows the electronic module inserted into the bPod enclosure. The connections between the BGM121 radio board module and the additional electronics components is available in Appendix A. The use of connectable wires attached to the BGM121 radio board enabled easy removal of the electronic module from the 3D-printed enclosure, as well as on-demand flashing of application code to the MCU.

3.3. Device Operation

When the bPod is powered on, the BLE software begins to broadcast advertising packets at a 200 ms interval in order to pair with a user device. These packets contain information from the GATT profile, such the device name, as well as other custom characteristics embedded into the code. An external device, typically a smart phone, will be able to discover and provide a list of nearby Bluetooth devices containing this information and the aforementioned services. When the bPod connects or is paired with the custom app, the broadcast packets become less frequent, only often enough to maintain the paired status. When paired, by default, the bPod stays in a low-energy state (EM2) until an event interrupt is triggered. An interrupt, for reference, is a conditional signal sent to the processor of the MCU indicating a specific routine that is immediately executed before proceeding to the same line of code prior to the interrupt trigger. The two main interrupt handles used in the programming of the bPod were external interrupts, triggered by write commands sent from the app, and software timers, triggered by internal clocks.

In Chapter 4, amperometric measurements performed with the bPod will be presented. The platform was submerged into a DI water solution and the DO%

saturation adjusted to steady state conditions between 0 and 100%. Further details discussing how these values are generated will be described in the experimental setup section in 4.1. For calibration of the sensor, chronoamperometric measurements were performed using the CALIBRATE operational state. First, the LMP91000 AFE is configured for amperometric measurements, used for three-electrode sensors. Next, the output voltage is recorded by the BGM121 ADC, while in low power mode, before momentarily toggling to active mode to wirelessly transmit the 16-bit value to the phone. This switching is repeated for the next recorded value every 50 ms for 25 s, completing one measurement. The CALIBRATE command is then sent to the bPod when the next steady state condition is achieved within the bioreactor. For real-time monitoring of DO with the bPod, the MEASURE operational state is used, triggering a similar energy mode that toggles once every 5 minutes, recording values every 50 ms for 25 s to produce a characteristic chronoamperometry curve. After each measurement sequence, the program checks the number of measurements performed; once the desired amount of data has been collected the device will return to deep sleep mode until another external command is given. A duty cycle of ~14% was determined to extend the current battery capacity from a couple hours to a couple of weeks.

3.4. 3D-printed Enclosure

A 3D-printing approach was employed as a rapid, low-cost prototyping method for the bPod enclosure, creating packaging to (1) protect the custom electronic module, (2) seal the device from the liquid environment, and (3) support contact with the fabricated electrochemical sensor. There exists a variety of 3D-printing techniques

suitable for generating small robust enclosures, including fused deposition modeling (FDM), stereolithography (SLA), and Polyjet printing. However, not all printing techniques are able to produce leak-proof features using biocompatible materials without additional post-processing (due to gaps between adjacent print layers). Biocompatibility and preservation of the electronic module in a liquid environment is critical for the successful operation of the system. To this end, the bPod was printed using a Polyjet printer, the Objet500 (Stratasys, Eden Prarie, MN) which employs UV-curable photo resins to produce high resolution prints with low moisture retention (1-2 %) [123]. A clear biocompatible resin commonly used in dental implants, MED610, in conjunction with a dissolvable support material was used to 3D-print the packaging for the encapsulation of the electronic module [124].

3.4.1. Architecture and Dimensions

The bPod was designed with a 60 mm diameter to incorporate the electronic module and sensor interface into a minimally viable product for monitoring DO. A larger module would allow for more flexibility when prototyping the electronics, as well as support successive testing of DO sensors. The ideal architecture for the bPod packaging was a sphere-like 'marble' with a target diameter of 25 mm (diameter of quarter). Smaller form factors would reduce potential interactions with the bioreactor impeller blades during stirring and agitation as well as minimize the shear effects of the device on cell culture products [47]. However, starting at the 60 mm size scale, a benchtop version could be validated with all of the system components before committing resources to a printed circuit board design. Additionally, the use of the

BGM121 radio board (40 mm x 35 mm) allowed for evaluation of the wireless communication capabilities of the bPod without encountering propagation signal losses due to an inefficient ground plane or PCB layout [125]. The spherical shape was inspired by submarine and buoy structures, which present a symmetrical distribution of mass and volume about the central axis of the bPod. Essential features for the bPod enclosure include a small cavity to hold the electronic module, interlocking seals for closing the device, adjustable mass for maintaining neutral buoyancy, and a sensor interface. Figure 3-12 shows an early conceptual representation of the 3D-printed packaging. Though ultimately impractical for various reasons not discussed here, this design showcased several of the necessary features that later were integrated into the bPod.

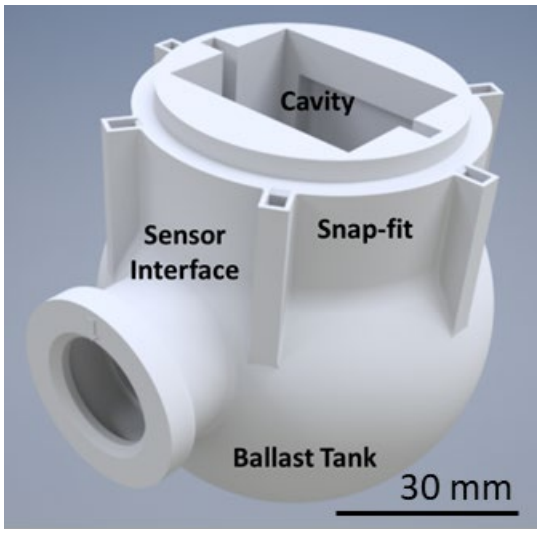

Figure 3-12. Conceptual representation of early bPod design. The functional features for the 3D-printed enclosure include a snap-fit seal, a fillable ballast tank, cavity for the electronics, and sensor interface plug opening.

bPod Enclosure Dimensions

The spherical pod consisted of an outer diameter of 60 mm and was assembled from two attachable parts as shown in Figure 3-13. The two halves (top and bottom) of the packaging were connected by a bayonet twist connector and sealed with three silicone O-rings. This allowed for switching various COTS components while designing the circuit, as well as improving the sealing of the packaging. A tolerance of 0.1 mm was used for the separation of the top and bottom parts, which press down onto an O-ring (55 mm inner diameter), and a tolerance of 0.45 mm for the two O-rings (50 mm inner diameter) used to create a leak-proof slip-fit seal. Silicon oil/grease and Teflon tape were incorporated to assist with O-ring sealing. The tolerance of the bPod enclosure was adjusted across several iterations to ensure that the seal was leak-proof. Moreover, application of a fine grit sand paper was necessary to smooth the 3D printed surfaces to ensure proper fitting between the two halves.

For achieving a neutral buoyancy condition two hollow cavities along the periphery of the package were included to allow additional weight or infill. The CEC was aligned using a 10 mm x 14 mm x 3 mm cutout, such that the sensor could be easily inserted into the electronic module. Finally, the sensor interface was designed to expose the sensing electrodes to the aqueous sample, while isolating the sensor contacts. The sensor interface geometry and leak-proof sealing were modified through three generations of prototype development, and evaluated for reliability during sensor testing. Each generation of the sealing interface is described in detail below.

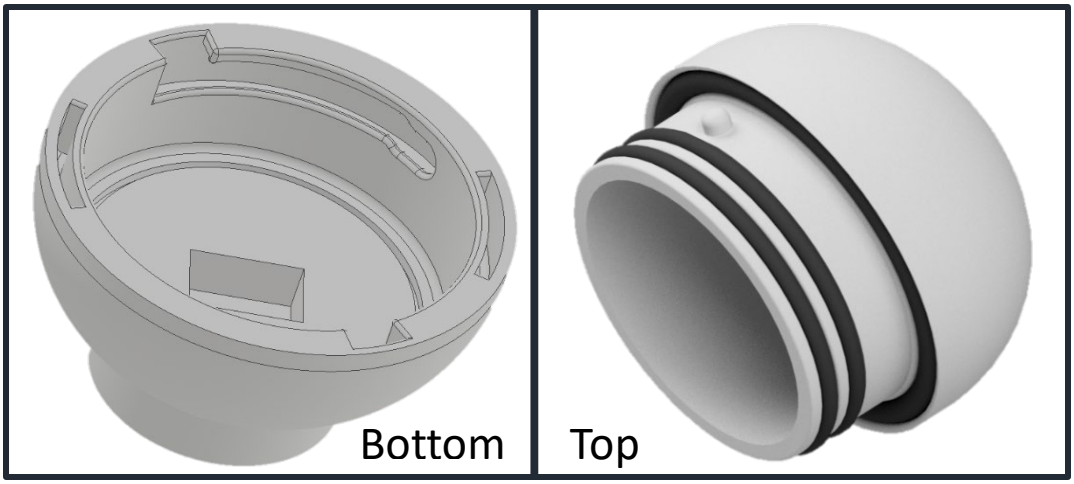

Figure 3-13. CAD drawing of the top and bottom halves of the bPod enclosure. Three O-rings were used to create a leak-proof seal for electronic module.

Generation 1: 3D-printed Enclosure for Glucose Sensing

As discussed in Chapter 2.1, the initial motivations for generation 1 of the 3D-printed enclosure were to enable the sensing of glucose. The electrodes were exposed to the liquid environment without the need of an electrochemical well to stabilize the sensor measurement. For achieving a leak-proof seal three custom molded Polydimethylsiloxane (PDMS) gaskets were utilized to seal the bPod interior, as seen in Figure 3-14A and Figure 3-14B. Details for the development of the generation 1 3D-printed enclosure and sensor interface are included in Appendix B. Due to issues with the PDMS seals leaking, difficulties with the PDMS fabrication, and concerns regarding exposing the sensor to the environment with minimal protection, the 3D-printed bPod enclosure (generation 1) and sensor interface design were significantly modified.

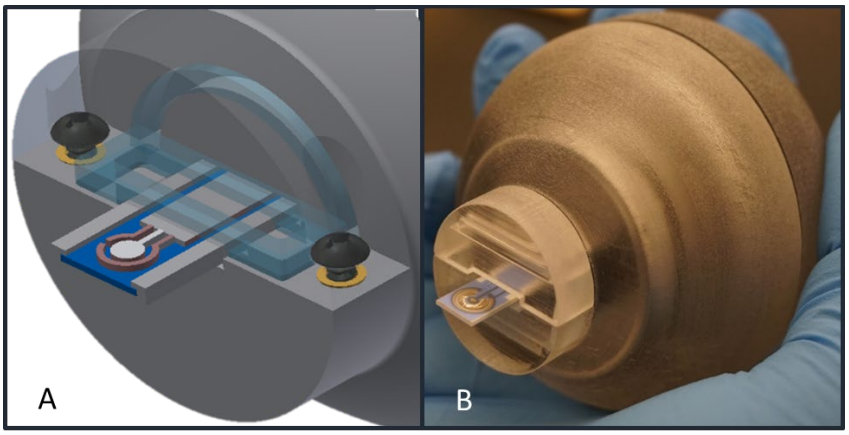

Figure 3-14. Generation 1 of 3D-printed enclosure. The sensor interface incorporates PDMS gaskets, which are press-fit against the sensor using two screws.

Generation 2: 3D-printed Screw-top Sensor Interface

The generation 2 bPod enclosure was designed to enable amperometric measurements of the fabricated DO sensors within a bioreactor. To accomplish this a 3D-printed screw-top sensor interface was utilized to form an electrochemical well integrated with the main 3D-printed enclosure, as shown in Figure 2-8A and Figure 2-8B. The design of the 3D-printed screw-top sensor interface was discussed in section 2.4.1, and a detailed description of modifications from the generation 1 to the generation 2 bPod enclosure are discussed in Appendix B.

It was found that the generation 2 bPod enclosure encapsulation method hindered sensor performance. The excess distance between the membrane and sensor surface caused a delay for the diffusion of DO into the electrolyte well from the bulk solution. This time delay was on the order of 10 minutes, which is undesirable for bioprocess monitoring within bioreactors. Therefore, to decrease the response and equilibration time of the sensor, an improved sensor interface was designed in generation 3 of the bPod enclosure.

Generation 3: 3D-printed Receptacle and Tape-based Sensor Interface

Generation 3 of the 3D-printed bPod enclosure greatly minimize the complexity of the sensor interface, by directly fabricating the electrochemical well onto the sensor rather than with the packaging, as was the case for generation 2. This approach preserved the integrity of the electronic module and improved consistency of the leak-proof sealing during testing. The aforementioned sealing interface (generation 2) was removed from the bPod enclosure and replaced with a 2 mm x 10 mm slit. When the top and bottom parts are brought into contact and twisted along the interlocking pin a frictional force is applied to the electronic module due to surface roughness of the internal cavity. At times this resulted in cracking of the Pyrex electrochemical DO sensor or unseating of wires used to connect the electronic components of the electronic module. While this did not degrade any leak-proof features, it resulted in numerous failed experiments. Therefore, for the generation 3 enclosure, the slit location for the DO sensor was flipped from the bottom half of the bPod to the top, according to the previously defined orientation provided in generation 1. As a result, the torque experienced by the electronic module during the assembly of the device was completely removed, allowing the bPod to be open and closed freely. This change is reflected in Figure 3-15 indicating the updated orientation.

For sealing the 3D-printed receptacle and the tape-based sensor interface discussed in Chapter 2, water-resistant epoxy (Devcon, Hartford, CT) was placed between the sensor assembly and the bPod enclosure slit followed by 15 minutes of curing. For interfacing with the electronic module, the 3D-printed receptacle

(generation 3 spacer) was designed and incorporated to add thickness to the sensor for insertion into the enclosure and robustness during handling.

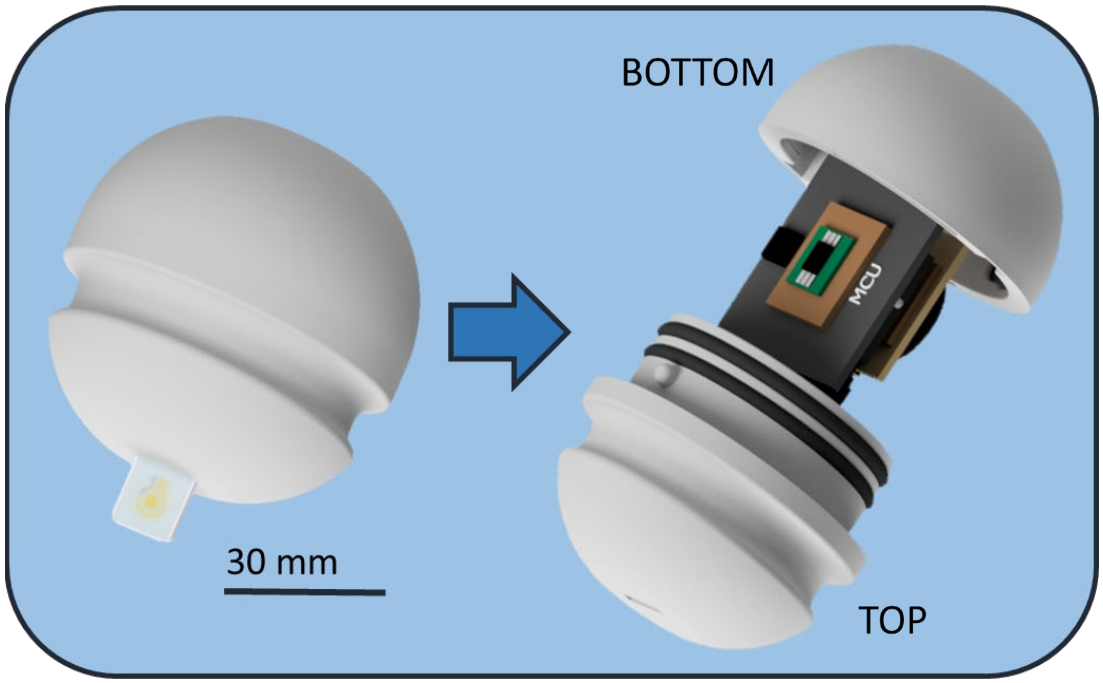

Figure 3-15. Generation 3 of bPod enclosure. Modifications consisted of removal of the sensing interface from the 3D-printed body, as well as swapping the location of the sensor opening from the enclosure bottom to the top.

3.5. Enclosure Summary

The 3D-printed enclosure had notably undergone many iterations to conform to the needs of the bPod system. The size of device was constructed to house the hand soldered electronic module, whose components and dimensions are summarized in Appendix A. Future iterations will seek to miniaturize the packaging size, while also satisfying the sensor interface requirements. Current limitations to scaling the packaging dimensions are found with the electronic module and battery size. The electronic module form factor can be reduced to roughly 18 mm in diameter by using a printed circuit board (PCB), while the battery is limited to roughly a 20 mm diameter to contain enough capacity for system operation. Strategies related to ongoing packaging designs will be discussed in Chapter 5.

Chapter 4. Validation of Integrated System

This chapter presents the electrochemical characterization of the fabricated DO sensor and the fully integrated bPod platform in several testing environments. The electrochemical characterization of the bPod was performed in three separate stages: (1) characterization of the DO sensors in a 250 mL beaker using a benchtop potentiostat, (2) characterization of the fully assembled bPod in a 2 L vessel for determining the optimal bPod testing experimental protocol, and (3) testing of the bPod in a 10 L Bioflo310 bioreactor for calibrating and dynamically monitoring the bPod platform at several DO% saturations. Within each testing setup several DO sensor packaging variations were demonstrated to improve the sensor repeatability and response time. In the following sections, the specifications for each testing setup will be explained and applied to validate system components for the bPod.

4.1. Electrochemical Characterization

4.1.1. Beaker-level Characterization of Electrochemical DO Sensor

Beaker-level Set-up

A small-scale beaker-level setup was developed for evaluation of the DO sensor prior to integration with the bPod platform. As shown in Figure 4-1, the setup incorporates a gas inlet for pumping air or N_2 into the beaker, a wired adapter for interfacing the sensor with the benchtop potentiostat, a flask holder for fixing the adapter in place, and a parafilm cover for trapping air inside the beaker. Sensors were submerged in 125 mL of 0.1 M KCl solution for electrochemical measurements, performed with a benchtop potentiostat (BioLogic VSP-300).

A single gas line, carrying either air or N_2, was connected to the beaker with polyethylene tubing (1/4" ID) and a stone bubble diffuser. The diffuser produces small gas bubbles, allowing facile gas dissolution by increasing the gas-solution interface, and leading to a rapid achievement of a partial pressure equilibrium. An external nitrogen tank (K-bottle) was connected to sparge (bubbling of a gas) N_2 into the beaker, displacing DO molecules within the solution, thereby creating a 0% DO saturation state. To return the solution back to an ambient oxygen condition, such as air (~20% O_2), the tubing was connected to an electronic serological pipette aid (USA Scientific, Ocala, FL), and air was pumped into the vessel via the accompanying air compressor. The parafilm cover was placed over top of the beaker to prevent gas exchange with the surroundings. By removing the parafilm cover the system would return to an ambient equilibrium after 10 – 15 minutes.

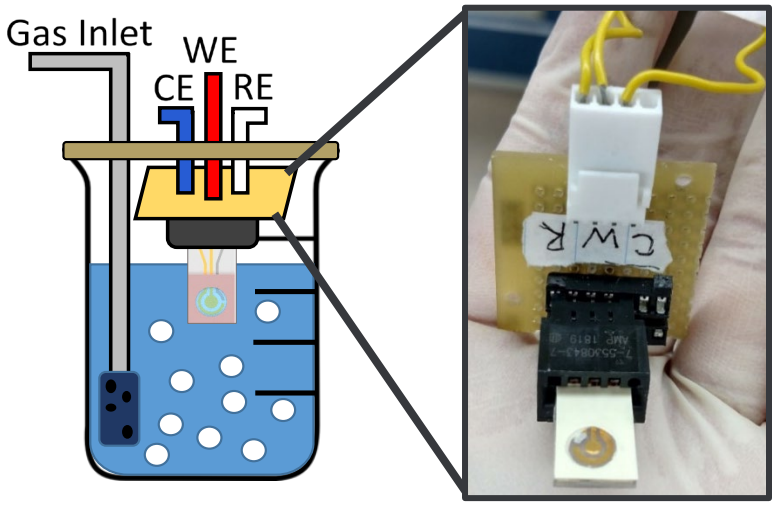

Figure 4-1. Illustration of the experimental setup used for determining the excitation bias for the reduction of DO. WE, CE, and RE were connected via three wires to a benchtop potentiostat, and the gas inlet provided either N_2 or air for varying the DO% saturation. The soldered adapter is used to interface the sensor and CEC to the BioLogic input pins.

Custom Adapter for Beaker-level Testing

Sensors were interfaced with the potentiostat via a custom adapter. The adapter utilizes the CEC and a 3D-printed spacer discussed in Chapter 3 to form an electrical contact with the sensors terminated with three wires. As seen in Figure 4-1, the adapter consists of two 2.54 mm pitch female headers soldered to a Veroboard (perforated FR4 board) which the CEC is plugged into. Traces on the backside of the board are soldered to a 4-pin 90° Molex connector, and the three wires are fastened with crimps inside the sockets. The wires connected with the potentiostat via alligator clips corresponding to the working, counter, and references electrodes.

Determination of Excitation Bias Point

The custom fabricated electrochemical DO sensors were evaluated using the beaker-level setup to determine a suitable excitation bias voltage which would maximize the DO reduction peak (maximally negative current). The sensor current response was recorded using a benchtop potentiostat (BioLogic), and the electrochemical properties of the three-electrode system (WE: Au, CE: Au, RE: Ag) in 0.1 M KCl were analyzed at two distinct DO% saturation states, namely a N_2 purged state (0% DO) and an air purged or ambient state (denoted as 100% DO). As discussed in the section 1.3.1, the dynamic range of DO sensors are defined by the signal difference between a 0 and 100 DO% saturation states. Common methods for controlling DO% saturation levels include pumping out (flowing N_2 gas into the system), or by adding an oxygen scavenger (i.e. sodium sulfite) [52]. The pump-out

method was utilized in this work to better relate to the bioreactor agitation conditions and to observe the effects of purging on the sensor response. Purging was disabled during measurements to minimize the effects of aeration and agitation on the bare electrodes.

Two electrochemistry techniques were employed to characterize the electrodes: cyclic voltammetry (CV) was used to determine the optimal voltage bias which was utilized in chronoamperometry (CA) for sensor calibration. Figure 4-2A presents the resulting cyclic voltammogram of the bare electrode at both N_2 and air purged states. The limiting current representing the reduction of DO was observed between -0.4 – -0.6 V, corresponding to the DO concentration. This is reflected as an output current ranging from 2 - ~5 μA between the 0 and 100% DO saturation states. As the potential became increasingly negative, hydrogen adsorption was observed at -0.72 V, therefore values beyond this point were discarded. From this, two candidate voltage biases were identified for application during CA measurement, namely -0.42 V and -0.5 V. These values corresponded to the excitation bias points that could be generated using the proposed potentiostat IC, namely the LMP91000. CA was applied as a fixed excitation bias pulse of -0.42 V, held for 45 seconds across the WE and RE, while the current was monitored between the CE and WE. The resulting chronoamperogram is shown in Figure 4-2B. The DO% saturation state alternated between 0 and 100% at both 5-minute (first three) and 10-minute (last three) intervals, which resulted in an easily distinguishable separation between 0 and 100% DO saturation. This experiment verifies the viability of the electrochemical DO sensor materials and topology for

bioprocess monitoring applications, as well as creates a reference system that can used to configure the AFE (LMP91000).

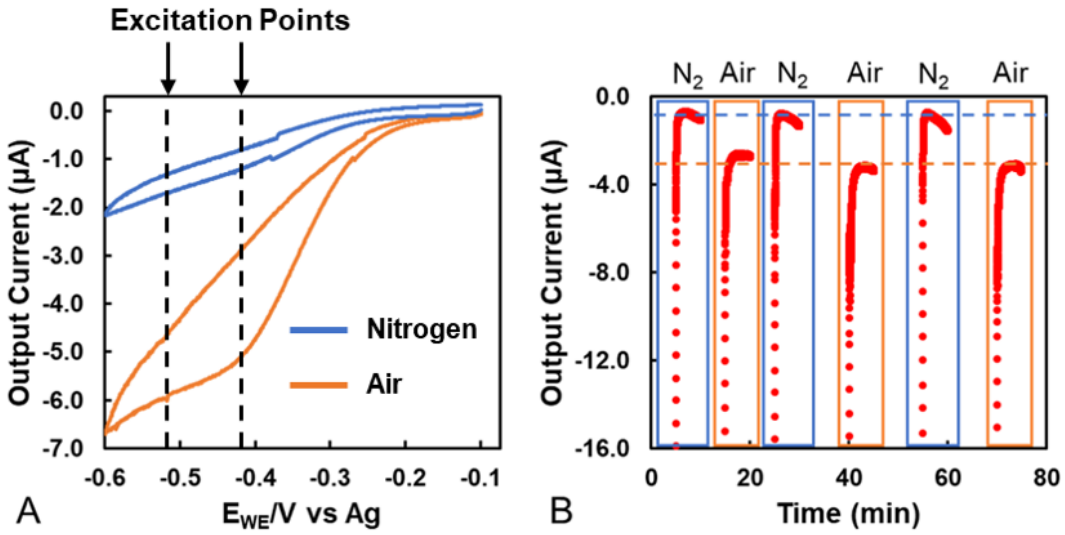

Figure 4-2. Electrochemical characterization of bare Au DO sensor. A) Cyclic voltammogram acquired from DO sensor in 0.1 M KCl purged at two different DO% saturation states, 0% (N_2) and 100% (air). CV was applied as a linear voltage sweep between 0.0 – -0.8 V at a scan rate of 20 mV/s. B) Chronoamperogram of 0% and 100% DO saturation states using an excitation bias of -0.42 V. Beaker is purged for three 5-minute intervals and three 10-minute intervals.

DO Sensor Testing with FEP Membrane

Following the electrochemical characterization of the bare Au DO sensors, electrodes were covered with an FEP membrane to form an isolated electrolyte well. The tape-based sensor interface, as described in section 3.3.3, was utilized for characterizing the current response of the sensor with and without the FEP membrane in 0.1 M KCl. This sensor interface provides a roughly 100 µm (thickness of electroplating tape) distance between the FEP membrane and WE surface, increasing the diffusivity of DO through the inner electrolyte, w improving the sensor response time. Since the DO within the bulk solution must diffuse through the FEP membrane

for the electrolyte reservoir to reach a steady state equilibrium, a delay in the response time for the sensor can be expected when compared to the bare Au electrode.

The beaker-level setup was used to compare the current response of the tape-based sensor interface to a bare Au sensor at two saturated DO states, an N_2 purged state and an air purged state. N_2 was sparged into the beaker for 3 minutes to generate a 0% DO saturation state, which was followed by sparging of air for 3 minutes to achieve a 100% DO state. The cyclic voltammogram in Figure 4-3 presents highlights the differences between the diffusion limiting current necessary for both sensor configurations. The CV was performed with a linear sweep from 0.0 – -0.65 to preserve the sensor integrity as the potential became increasingly negative. Most notably, the current response when comparing the bare Au sensor and the tape-based sensor interface (FEP membrane) was similar at the N_2 purged state, about 1 μA at -0.5 V, whereas a large deviation was seen in the current response during the air purged state between the FEP membrane sensor (-15 μA) and the bare sensor (-25 μA) in 0.1 M KCl. This result indicates that, under identical sparging idle times, the tape-based sealed sensor fully saturated at a lower excitation potential due to the diffusivity of the attached FEP membrane.

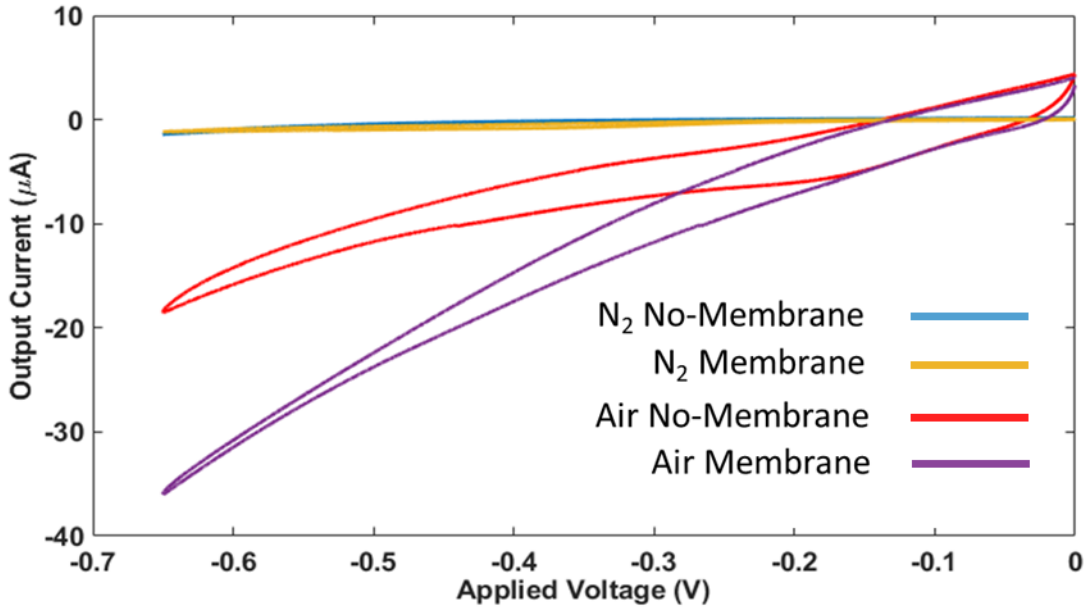

Figure 4-3. Impact of including or not including the FEP membrane on electrode response to DO. Cyclic voltammograms comparing peak current response between a bare sensor and a membrane integrated sensor in 0.1 M KCl at air purged and N_2 purged DO% saturation states.

To demonstrate the ability of the FEP membrane electrode to perform in a non-conductive media, the bare Au electrodes and the tape-based sensor interface (see section 2.4.3) were tested in DI water. With an identical experimental setup, the sweep parameters were adjusted to 0.0 V – -0.6 V, and the water was purged solely with air for 10 minutes (given that the N_2 purged state was the same for both sensors). It is shown in Figure 4-4 that the bare sensor is unable to measure DO in the absence of an electrolyte (KCl), which provides ions which enhance electron transport to the sensors [126]. Conversely, the FEP membrane enabled the DO sensor to successfully measure DO by diffusion through the electrolyte cell. When testing bare electrodes, bubbles from the sparging may displace fluid from the electrode surface and cause sporadic spikes in the current response, therefore the gas sources were turned off momentarily

during electrochemical DO measurements. This behavior was not observed in electrodes covered with an FEP membrane, therefore measurements and sparging could be performed simultaneously, providing dynamic monitoring capabilities which are compatible with existing bioreactor systems. This implies that the bPod would be able to monitor culture parameters under continuous agitation and aeration conditions, which are necessary for the proliferation of the cell culture within the bioreactor.

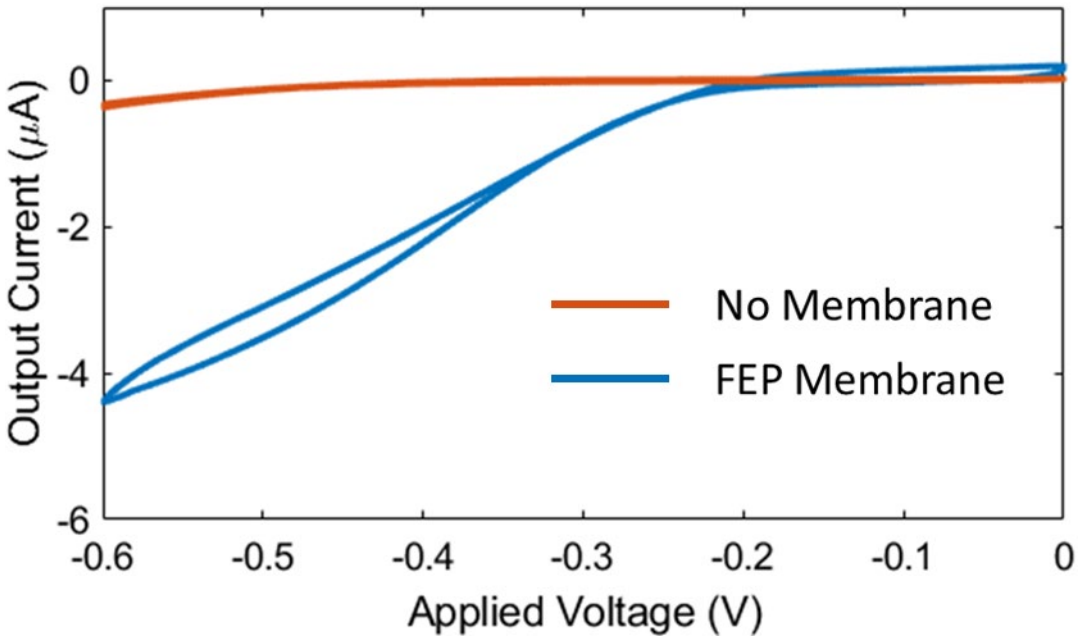

Figure 4-4. Validation of leak-proof sealing and evaluation in DI water. Cyclic voltammograms of a bare sensor and a membrane integrated sensor in DI water at an air purged DO% saturation state.

Beaker-level Measurements with LMP91000

The benchtop potentiostat was operated as a gold standard reference for electrochemical characterization of the DO sensors and assisted with transitioning to the AFE module (LMP91000). The small form factor of the LMP91000 allowed for

portable amperometric measurements. The operation of the AFE however presented two challenges: (1) a limited resolution for applying excitation biases and (2) incompatibility with performing CV measurements. However, utilizing the excitation bias determined from the benchtop potentiostat, CA measurements were possible for the LMP91000 and the electronic module. Therefore, an experiment was conducted using the bare electrode sensors to verify proper sensor conditioning and monitoring capabilities of the LMP91000. The electrodes were submerged in 1 mM potassium ferrocyanide ($K_4Fe(CN)_6$) in DI water, a common compound for characterizing electrochemical sensors, and the current response was monitored for several voltage biases applied by the LMP91000. The LMP91000 potentiostat was programmed to apply a +0.2V pulse for 120 seconds ($K_4Fe(CN)_6$ oxidation potential vs. silver reference electrode) [127]. As shown in Figure 4-5, a -0.2V pulse is applied for 60 s, resulting in a reduction spike that reaches a steady state value after about 10 seconds, followed by a +0.2 V pulse applied for 40 s, resulting in an oxidation current response. Data was captured by the BGM121 and transmitted via the Universal Asynchronous receiver/transmitter (UART) through a USB port, and recorded as a .csv file on the PC. This result demonstrated control of the LMP91000 registers for modulating the excitation voltage, as well as the monitoring of the output current. The representative chronoamperometric responses were utilized to determine essential parameters (i.e. pulse duration, sampling rate, the output gain, and virtual ground offset) for adjusting the LMP91000 measurement sequences, namely the sensor conditioning and digitization of the output voltage using the BGM121 ADC peripheral.

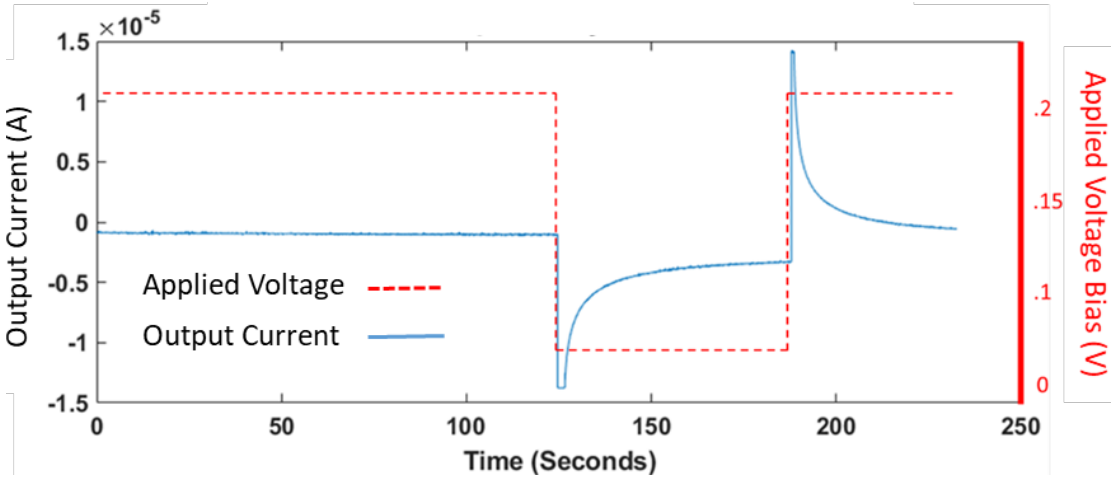

Figure 4-5. Chronoamperogram of gold electrode with LMP91000 excitation bias between 0 and +0.2 V in 1 mM $K_4Fe(CN)_6$ in DI water. The LMP91000 converts the output current to a voltage which is digitized via the ADC from the BGM121. The data is recorded via wired UART communication to the PC.

Evaluation of Electronic Module

Following validation of the LMP91000 AFE module with 1 mM $K_4Fe(CN)_6$ the electronic module was assembled as outlined in section 3.2. In order to evaluate the electronic module, for monitoring DO a two point-measurement was performed using the beaker-level testing setup. The DO sensor in this case, however, is used without the FEP membrane attached and the sensor surface was directly exposed to a 0.1 M KCl solution, in order to solely evaluate the operation of the electronic module. Chronoamperometric measurements were performed at 5-minute intervals with an excitation bias of -0.5 V, and the current response was monitored for 1 minute. This current was converted to a voltage reading using the LMP91000 transimpedance amplifier circuit, sent to the ADC of the microcontroller, and then transmitted to the PC using the UART (wired connection). Figure 4-6A shows the chronoamperogram at a 0 and a 100 DO% saturation state, obtained by alternating sparging of air and

nitrogen, respectively, into the beaker every 5 minutes (Figure 4-6B). The observed response time of the sensor was roughly 10 seconds for the air sparge state and 3 seconds for the N_2 sparged state, corresponding with direct reduction of DO at the working electrode surface with minimal delay before reaching a steady state response. The scattered distribution of data implies that measurements are susceptible to burst noise, or artifacts as a result of bubbles that collect at the sensor surface, and conversion errors relating to the ADC. It was determined that the BGM121 data transmission was set to a faster sampling rate than the ADC could convert the measured value, however this was resolved for future experiments. The electronic module was able to successfully apply a -0.5 V bias necessary to generate an output current that fits within the adjustable bounds of the LMP91000 AFE (5 µA to 750 µA).

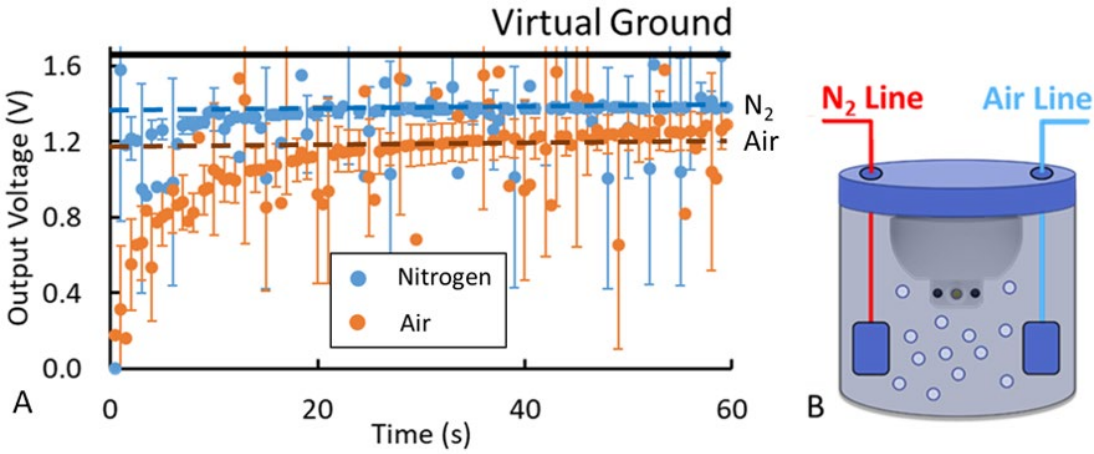

Figure 4-6. A) Chronoamperometric measurement of DO in 0.1 M KCl at an excitation bias of -0.5V (N=5). DO% saturation states were generated with N_2 and air, respectively. Test was performed without the FEP membrane attached and data recorded with wired UART transmission. B) Illustration of experimental setup with N_2 and air gas line for testing the electronic module.

4.1.2. bPod Testing in 2 L Glass Vessel

Two-point calibration in this work refers to a comparison of two separate measurements performed at the determined voltage bias with the same sensor in the bioreactor system: 1) at a 100% DO saturation state and 2) at a 0% DO saturation. This is essential for ensuring repeatability between different sensors, as well as accounting for variations in the bioreactor testing setup. For example, when comparing the benchtop setups, a 200 mL beaker, and a 10 L bioreactor vessel, may produce drastically different max current during two-point calibration, due to the stirring capabilities of the Bioflo310, however this parameter was not compared. Bioreactor system pressure, temperature, agitation and sparging capabilities all contribute to the maximum achievable DO% saturation and the time required between measurements [12], [36]. Three sensor interfaces with varied electrochemical cell geometries were evaluated: the 3D-printed screw-top, the 3D-printed receptacle, and the taped-well packaging architecture (see 2.4.3). The sensor response and equilibrium time between each specific generation of the bPod will be compared and the aforementioned parameters will be optimized for calibration of the final bPod design.

2 L Glass Vessel Setup

A 2 L glass vessel set-up was developed to generate a 0 and 100% DO saturation states for performing two-point calibration with the bPod. Figure 4-7 provides an overview for the 2 L bioreactor vessel setup. Gas supplies are provided by a nitrogen tank (K-bottle) and a compressed air line (attached to the building). Polyethylene tubing (1/8” ID) connected pressure regulators (5 psi) attached to the gas supplies, through a

1/8”-1/4” adapter (McMaster-Carr) to the fine stone bubble diffusers, which connected to 1/4” ID polyethylene tubing.

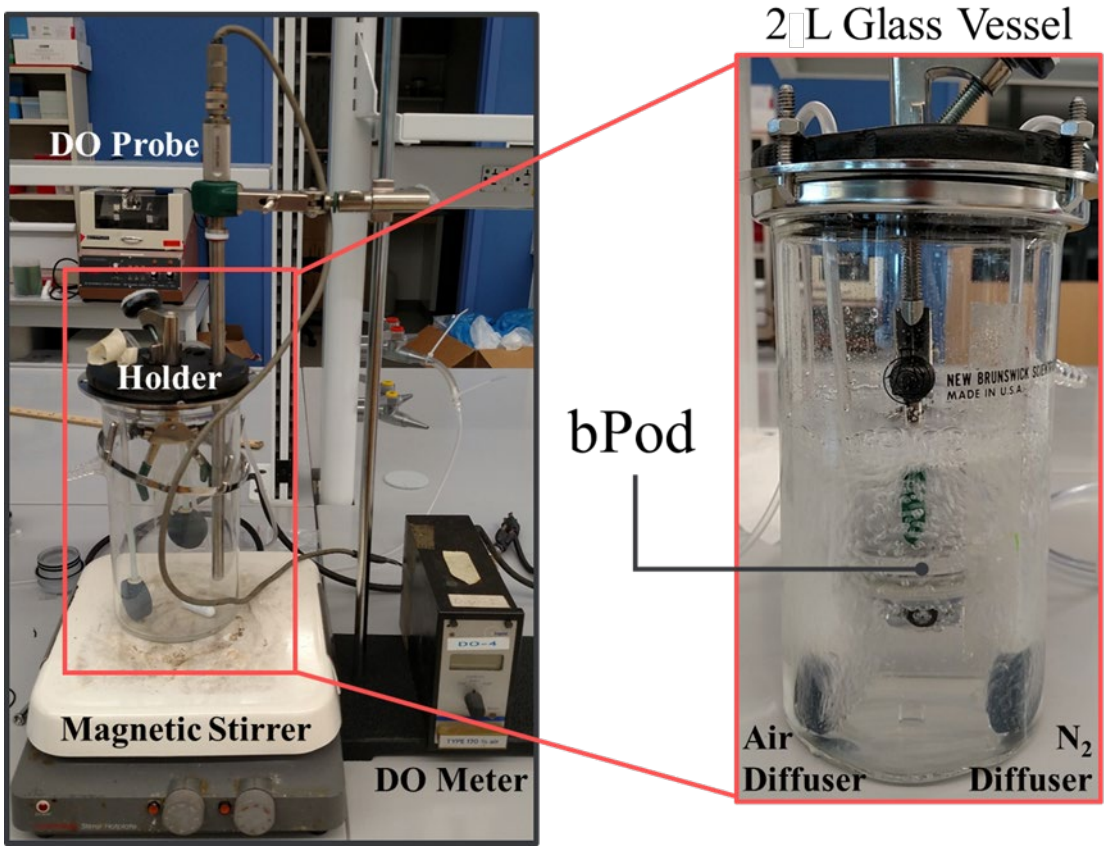

Figure 4-7. Experimental setup for the 2 L glass vessel. Setup incorporates a gas inlet for pumping N_2, an inlet for pumping air, flask holders for fixing the bPod and DO probe in place, a magnetic hotplate, a magnetic stir bar, and a DO meter. Air and N_2 are sparged in the 2 L vessel to perform two-point calibration.

The DO% saturation state is monitored by a commercial inline DO probe (Mettler Toledo) fixed into place by a flask holder and connected via a wire to a DO meter (Ingold), where the DO% value is displayed. The bounds of the DO meter are adjusted via an analog knob, such that both a 0 and 100% DO states are achieved for the given system. The larger vessel provided a dedicated inlet for each gas source and enabled

more rapid purging of air into the vessel. This reduced the equilibration time for generating a 100% DO state as compared to the beaker-level set-up. Simultaneous sparging of air and N_2 into the 2 L vessel is shown in Figure 4-7, with the generation 2 bPod suspended in the solution, however no control of the gas flow rate into the vessel was available.

Two-point calibration is typically conducted using a long purge time (i.e. 15-20 minutes) for DO% saturation values to completely stabilize. The hotplate is placed underneath the 2 L vessel and applies additional agitation to the system by spinning a magnetic stir bar. The formation of bubbles onto the membrane surface of the DO probe and the bPod, causes fluctuation in the DO saturation. The magnetic stir bar assists in the mixing and perturbation of the solution underneath the probe and bPod, ensuring sufficient diffusion of dissolved oxygen through the FEP membrane and stabilization of the steady state probe readings. This arrangement supports chronoamperometric measurements and two-point calibration of the bPod, containing the developed electronic module assembled with the rest of the system components.

Generation 2: 3D-printed Screw-top Sensor Interface

The two-point calibration of the bPod (generation 2 enclosure) was performed in the 2 L testing setup. Once a stable response was observed then a measurement could be performed with the bPod. The excitation bias determined during benchtop testing is applied to the assembled DO sensors, using the CALIBRATE command (as describe in 3.2) at the two DO% saturation states (0 and 100%, respectively). Figure 4-8A displays the resulting chronoamperogram of the two-point calibration with the FEP

membrane attached to the screw-top sensor interface, demonstrating successful wireless transmission of data to a custom phone app, and exhibiting smaller variations of the current response due to system agitation than without the FEP membrane. Testing occurred in 0.1 M KCl, with an applied excitation bias of -0.5 V for 40 seconds as opposed to 60 seconds. Longer duration sparging and wait between measurements (5-10 minutes) were added to allow the bulk solution to reach a steady state DO% saturation, as well as for the electrolyte well to equilibrate with the bulk. By reducing the measurement duration and maintaining a distinguishable difference between the equilibrium 0 and 100% DO saturation state, the bPod is able to remain in a low-energy mode for a longer time interval, thus decreasing the power consumption. During CV comparisons between membrane and non-membrane sensors, an increase in the sensor response time was observed. This was attributed to the additional diffusivity of the FEP membrane. The configuration of the bPod enclosure (generation 2), which resulted in the increased sensor response time incorporated the 3D-printed screw-top sensor interface (as described in 3.3.2).

Repeated experiments with the same sensor several days later were performed, resulting in a reduction in the voltage response from 0.75 V to 1.40 V at 100% DO saturation, as shown in the chronoamperogram presented in Figure 4-8B. This behavior originates from instabilities of the Ag/AgCl RE which occur over time as the thin film Ag layer is consumed during reduction in KCl. Inefficiencies with the 3D-printed screw-top sensor interface design, notably the 7mm distance between the FEP membrane and the electrode surface also contributed to the diminished voltage

response and remained unchanged even after 40 minutes of constant sparging at each DO% saturation state.

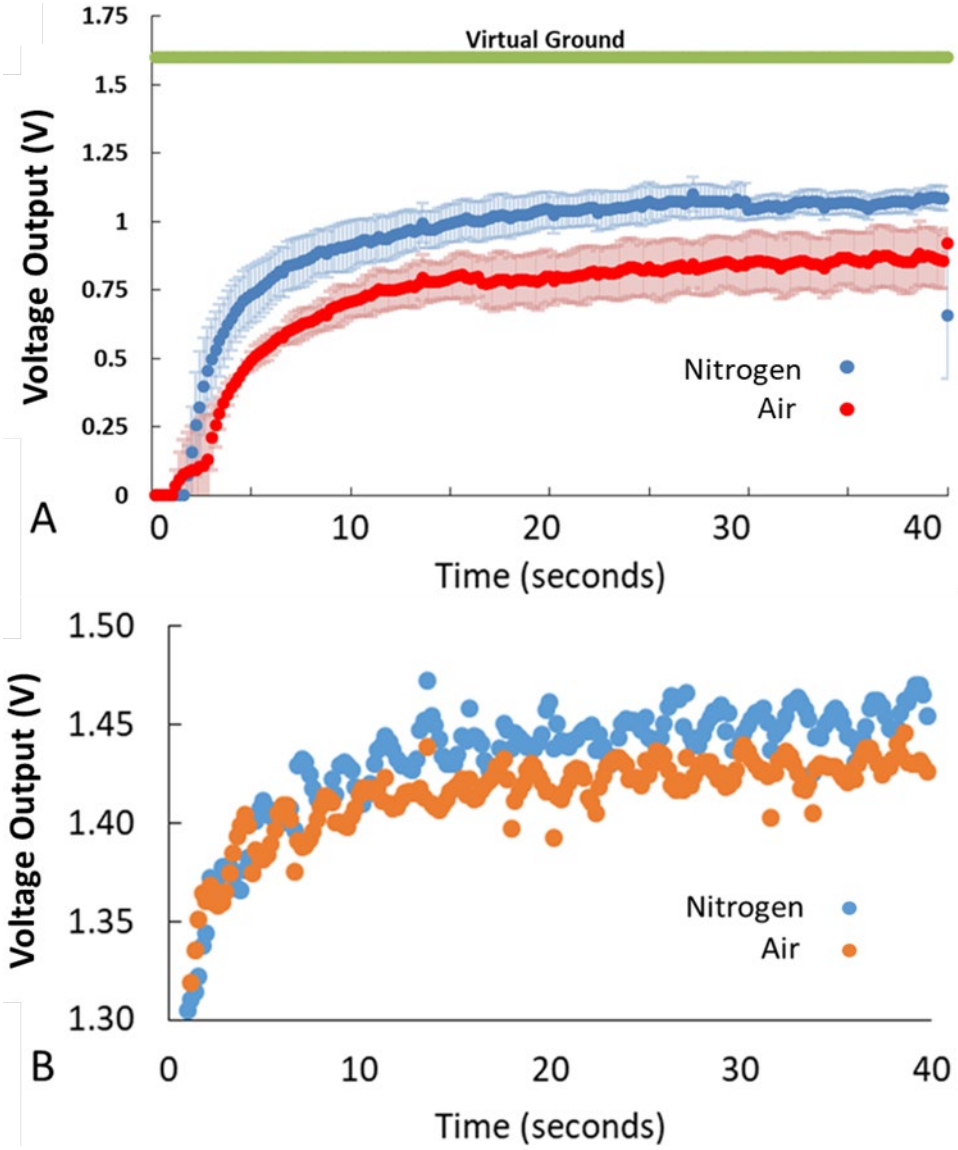

Figure 4-8. Two-point calibration of generation 2 bPod and 3D-printed screw-top sensor interface with FEP membrane in the 2 L testing setup with 0.1 M KCl. A) Chronoamperogram of averaged voltage output at two DO% saturation states generated by purging N_2 (0% DO) and air (100% DO), respectively, at 10-minute intervals and apply an excitation bias of V = -0.5 V (N = 4) for a 40-second measurement. B) Degradation of sensor response was observed after several days following the same testing conditions.

Generation 3: 3D-printed Receptacle

Addressing concerns with the screw-top sensor interface, the complex generation 2 enclosure was modified, and the 3D-printed receptacle was used instead to form the electrolyte well (described in 2.4.2). Recall the 3D-printed receptacle was inserted into the enclosure and sealed with epoxy at the intersection of the generation 3 bPod enclosure, as shown in Figure 4-9A. The simplified sensor interface allowed the bPod to be placed into the 2 L glass flask and a two-point calibration was performed. In order to obtain the electrochemical characterization throughout the duration of the measurements, a 3.7 V Li-Po battery (GM301014H, PowerStream) was utilized to a power the device, and wireless data acquisition was conducted using the 'CALIBRATE' command of the custom app. Additionally, DO% saturation was monitored once every 5 minutes for three saturation states N_2 purged (0%), O_2 purged (100%) and a mixture of O_2 and N_2 (~50%) purge conditions. Slight variations in the values read by the DO meter were observed during simultaneous sparging of both N_2 and O_2 due to the proximity of the O_2 and N_2 diffusers to the DO probe which caused the steady state percentage to fluctuate +/- 5%. The integrations of a mass flow controller with the 2 L setup would be necessary to correct this behavior.

For testing with the 3D-printed receptacle the compressed air line (building) was replaced with a regulated oxygen tank (K-tank). Figure 4-9B presents the chronoamperogram of the bPod with the 3D-printed receptacle sensor interface at a -0.5 V excitation bias for several DO% saturation states (0%, 50%, 100%), providing a remarkable decrease of the sensor response time and minimum deviation of the repeated values. By reducing the distance between the membrane and the electrode

surface from 7 mm to 500 µm the electrolyte well was able to quickly achieve a steady state DO% saturation. The 3D-printed receptacle starting to exhibit steady state behavior within 4 seconds as compared to 10 seconds when using the screw-top sensor interface. Additionally, using the 2 L bioreactor setup, testing parameters pertinent for tuning of the electronic module, such as measurement duration, equilibration time, response time, sampling rate, and output gain were adjusted to improve system accuracy. A noted downside of this implementation is that though excellent monitoring capabilities were possible the reliability of the sensor assembly warranted further adjustments to the sensor interface prior to scaling to the 10 L bioreactor. It was found that delicate epoxy seals resulted in an inconsistent sensor assembly with low yield and reduced the sensor lifetime (1 or 2 days) as portions of the electrode surface areas were covered while forming the well, as described in section 2.4.2.

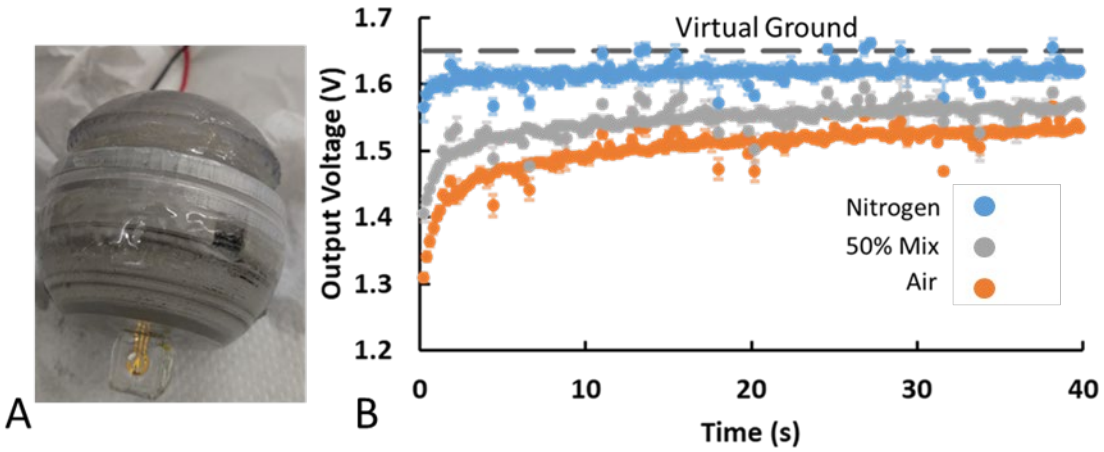

Figure 4-9. Validation of the 3D-printed receptacle sensor interface. A) Illustration of assembled bPod. B) Chronoamperogram of averaged voltage output (N = 4). System was purged with either air (orange), N_2 (blue), or a mixture of both (grey) at 5 minutes intervals at an applied voltage bias of V = -0.5 V. A decrease in the output voltage corresponds to the reduction of dissolved oxygen.

4.1.3. bPod Testing in 10 L Bioreactor

10 L Bioreactor Set-up

A 10 L glass bioreactor vessel coupled with the Bioflo310 fermenter (Eppendorf), was utilized for generating a calibration curve for the bPod. In addition, this equipment provides a viable testbed for analyzing the continuous monitoring capabilities of the bPod under a variety of system conditions for long-term bioprocess monitoring applications. As shown in Figure 4-10A, the 10 L bioreactor vessel is equipped with two Rushton blade impellers for agitating the solution, a motor column for driving the circulation of the impellers, a single gas inlet connected to a sparger at the bottom of the vessel for bubbling in gas mixtures, baffles for assisting with bioreactor mixing, a water cooled/heated metal jacket to stabilize the temperature of the vessel, and several sensor ports for a DO probe, a pH sensor as well as a temperature sensor. The bioreactor components described above are controlled by an accompanying Bioflo310 fermenter, which is capable of producing a variety of DO% saturations via a built-in mass flow controller, as well as monitoring the DO% saturation using the DO probe for the duration of a bioreactor process.

A single gas inlet is utilized for purging a mixture of air, N_2 and O_2 into the vessel. High pressure polyurethane tubing (5/32" ID, 1/4" OD, MSC Industrial Supply, Melville, NY) is attached to three regulated gas sources: a pure nitrogen tank (AirGas, Radnor, PA), a pure oxygen tank (K-bottle), and a compressed air line (supplied from lab bench), enabling highly controllable gas mixture concentrations to be purged into the 10 L vessel. Gas pressure for each of the three inputs is limited to less than 10 psi, and the overall gas flow rate (L/min) of the fermenter can be specified via the control

interface. It is important to note that the Bioflo310 does not internally mix the gases prior to release, instead the gas flow into the vessel is demultiplexed and output as a periodic pulse, dependent on a defined duty cycle. For example, a flow ratio (O_2:N_2) of 50% O_2 and 50% N_2 (50:50) for a one second pulse will result in 0.5 seconds of O_2 and 0.5 seconds of N_2 gas, respectively, to be purged into the vessel at a defined max flow rate.

The DO% saturation state is monitored using a commercial inline DO probe (30 mm) fixed to an access port on top of the vessel and displayed in real-time onto the integrated touchscreen user interface – values are saved once every 30 seconds. Values are calibrated through the user interface and set manually following purging of the system with either 100:0 of O_2 (or air), the 100% DO saturation bound, followed by 0:100 N_2, the 0% DO saturation bound. Once calibrated intermediate DO% saturation states are achieved through modulation of the N_2, O_2, and air ratio. As shown in Figure 4-10B a descending cascade of DO% saturation equilibrium states beginning at 100% DO and ending at 0% DO is achieved for characterization of the commercial DO probe. It is this DO% saturation reference which shall be used for experiments performed with this setup.

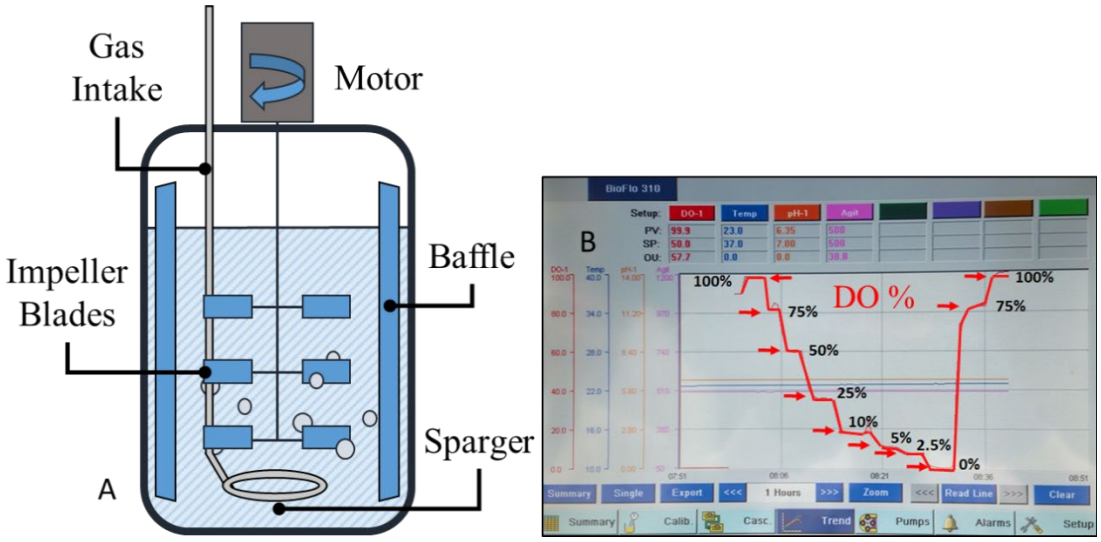

Figure 4-10. 10 L experimental setup. A) Description of the 10 L bioreactor vessel components. B) Screenshot of the characterization of the DO% saturation profile produced by the Bioflo310 fermenter.

The Bioflo310 fermenter is operated in three-gas-mode which enables mixing of oxygen, nitrogen, and air, while also fixing the impeller blade rotation to a constant rpm. For the following experiments, compressed air was not used, however, future integration into the Bioflo310 is expected to allow for long-term gas purging of the bioreactor (more than 10 days), given the limited supply of the O_2 and N_2 gas tanks. Additional operation modes allow for long-term bioprocess monitoring defined by system cascades that modulate the agitation of the system, by either increasing or decreasing the rpm of the impeller blades, to maintain culture parameter values, such as DO% saturation, at different stages of cell growth. The 10 L bioreactor setup and Bioflo310 fermenter have been used to evaluate the viability of the bPod prototype under a variety of test condition, and provide an invaluable testbed for further investigation onto the viability of the platform for large-scale bioprocess monitoring applications [128].

Generation 3: Tape-based Sensor Interface

To calibrate the bPod inside the 10 L bioreactor vessel the tape-based sensor interface design was integrated with the bPod as described in section 2.3.3, trapping the 0.1 M KCl electrolyte between the FEP membrane and the gold electrode. The bPod was submerged inside the bioreactor utilizing a braided two-wire tether to (1) provide a 3.3 V voltage supply (Agilent, Santa Clara, CA) for prolonged measurements and (2) to prevent the device from colliding with the rotating impeller blades. Prior to measurements, the Bioflo310 fermenter gas ratio was set to start with a two-point calibration of 0% and 100% DO between 100:0 and 0:100 at a 25 % interval generating several DO saturation percentages using the built-in mass flow controller (2 L/min flow rate) with a fixed spin speed of 75 rpm. Table 4-1 summarizes the O_2 and N_2 ratios input in the flow controller and the generated DO% saturation states as correlated with the commercial inline DO probe. The DO sensor was excited using -0.5 V, and the current response was measured every 5 minutes for 30 seconds at a sampling rate of 50 ms with the 'CALIBRATE' state. Data was wirelessly transmitted from the bPod to the external modified smart phone app.

Table 4-1. Parameters for the generation of DO% saturation states. Constant variables include temperature (22 °C), impeller blade speed (75 rpm), and max flow rate (2.0 L/min).

O_2:N_2 (Ratio)	**DO%(Probe)**
100:0	100%
75:25	79%
50:50	55%
25:75	25%
100:0	0%

Figure 4-11A shows the resulting chronoamperograms of the bPod for a decreasing DO saturation state in DI water. A steady state output voltage was observed after 10 seconds at each DO% state, exhibiting a linear behavior in agreement with the polarographic DO probe. The measurement duration of 10 seconds allows the entire current response to be observed, and comparatively to previous measurements (40 seconds) reduces the time the bPod operates in active mode, thus reducing the power consumption. Even shorter measurement durations would allow for further reduction in the power consumption. However, the current response prior to 5 seconds have shown a lack of repeatability across additional sensors.

Figure 4-11B provides the resulting calibration curve, correlating DO% saturation to the output voltage at 10 second and exhibiting a linear response (correlation coefficient R^2= 0.9794) with a sensitivity if 37.5 nA/DO% and limit of detection of 8.26 DO%. Additional testing is necessary to achieve dynamic sampling at various locations for untethered experiments, which would require extrapolation of the current response at lower measurement times (i.e. 5 seconds) that are correlated with the DO steady state behavior.

Industrial bioreactor systems typically utilize an air gas source to generate a calibrated 100% DO saturation state, therefore the dynamic range of the bPod can be readily adjusted to account for this. The resolution is currently limited by the diffusivity of the FEP membrane, the resolution of the LMP91000 TIA, and the stability of the sensor. Each of these parameters can be further optimized to improve the resolution of the bPod by maintaining fixed timed intervals and fermenter settings for each measurement, and systematically adjusting. Nonetheless essential functionality of the

60 mm bPod tethered in the 10 L setup was demonstrated and validation of the system components necessary for scaling the platform was completed.

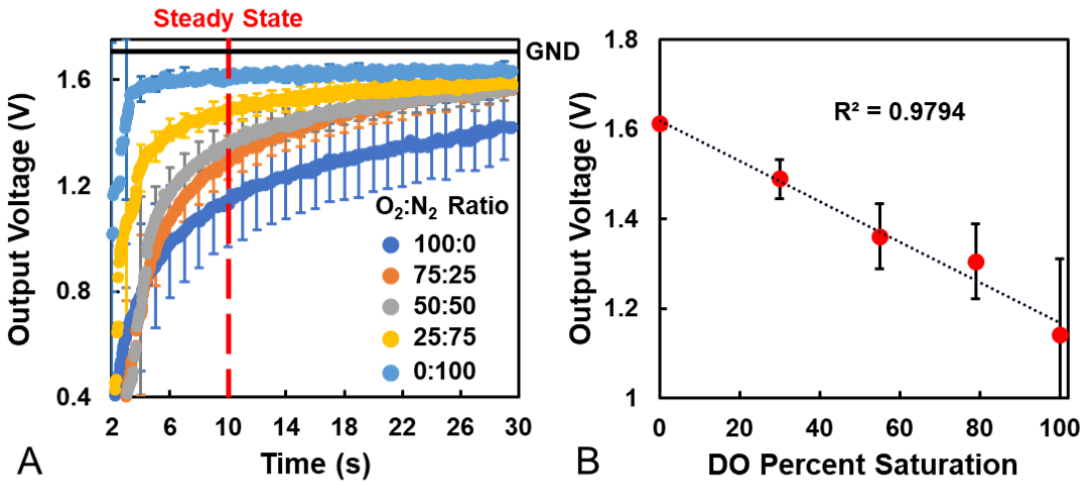

Figure 4-11. Electrochemical characterization of the bPod for wireless amperometric measurements in DI water. (A) Chronovoltammogram depicting the averaged output voltage recorded by the bPod with 3 repeats at a 5-minute interval (N=3). The O_2:N_2 gas ratio was adjusted from 100:0 to 0:100 at a 25% interval. (B) Resulting calibration curve taken at steady state (10 sec) and compared to the commercial polarographic DO probe.

Real-time Monitoring of DO with Free-floating bPod

To evaluate the stability and continuous monitoring capabilities of the untethered system, the bPod was deployed in the 10 L bioreactor. The 'MEASUREMENT' sequence, as described in section 3.1.2, was utilized to perform chronoamperometric measurements of DO every 5 minutes for 1.5 hours. The DO% saturation was adjusted from 100 to 0% DO at 25% intervals every 10 minutes. Fig. 4-12A depicts the steady state output voltage response of the bPod taken after 10 seconds. Similar to calibration results shown in Fig 4-11, the output voltage was found to linearly increase inversely proportional with DO% saturation, demonstrating excellent

reproducibility using the tape-based sensor interface. bPod measurements were converted into a DO% saturation for comparison with the commercial polarographic DO probe to evaluate the system viability in Fig. 4-12B. Initial measurements varied less than 3 % (1 hour), with a slight increase in drift between the bPod measurements (~9%) observed over time. The average shift across the measurements was 4 %. A possible explanation for this discrepancy is the degradation of the sensing electrode and shifting of the silver reference due to repeated excitation. Additionally, differences in membrane permeability of the commercial DO probe and FEP membrane used for the bPod may imply measurement intervals longer than 5 minutes are required for achieving an equilibrium within the electrolyte reservoir. However, the DO probe and bPod were found to converge slightly with additional sparging time at each particular DO% saturation.

Potential improvements to the bPod sensor response are increasing the ratio between the surface area of the counter and working electrodes (CE:WE > 2:1) to minimize the potential difference between CE and WE during measurements [129], operating a lower excitation potential (-0.42 V), or applying a weighted correction factor based on the rate of sensor degradation. For example, a suggested method to account for the shift in DO% saturation, is to apply a correction factor (CF). As shown in Fig. 4-13, the absolute value of the difference between the bPod and DO probe DO% were recorded for each measurement, showing a linear deviation for values greater than 5% after 45 minutes. A linear fit was applied and reflected in Fig. 6B, where the modified bPod values with the CF (bPod-CF), show significantly reduced DO% deviation (< 4%) across later measurements (after 45 minutes) as compared to the

reference inline probe. Therefore, offline correction of linear DO% saturation shifts provide a viable solution to account for degradation in the sensor response, prolonging device operation and stabilizing the DO% saturation measurement of the bPod.

The 3.7 V Li-Po battery maintained a stable supply voltage without degradation throughout the measurement. This sampling time can be extended using a larger capacity battery, such as a typical CR2032 coin cell (Energizer), in order achieve operational lifetimes suitable for mammalian cell cultures [130]. While the introduced bPod platform sufficiently validates the practicality of free-floating wireless capsules for DO monitoring within bioreactors, there are additional opportunities to extend this study in terms of device scalability, sensor network size, and continuous monitoring of cell culture products of interest (i.e. monoclonal antibodies). Approaches integrating wireless microsystems with specific and robust sensors can greatly enhance bioprocess monitoring capabilities and provide a platform for investigating product heterogeneity with bioreactors.

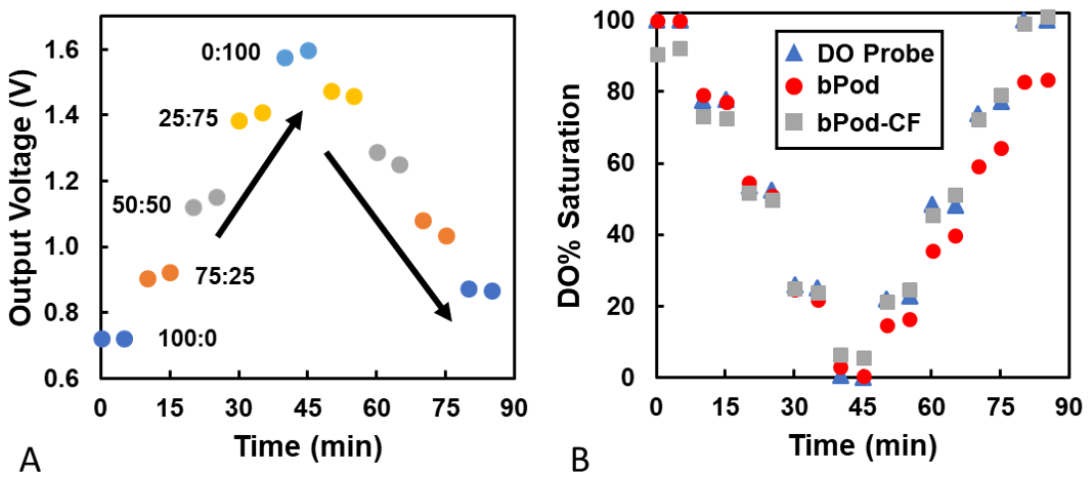

Figure 4-12. Electrochemical response of untethered bPod (w/ battery) in the 10 L bioreactor setup. Gas input is alternated (O_2:N_2 - 100:0, 75:25 50:50, 25:75, 0:100) over a 1.5-hour period using a 5-minute measurement interval. (A) Output voltage from the bPod recorded at steady state (10 s). (B) Comparison of the inline DO probe (blue, triangle), bPod (red, circle), and corrected bPod (bPod-CF) (gray, square).

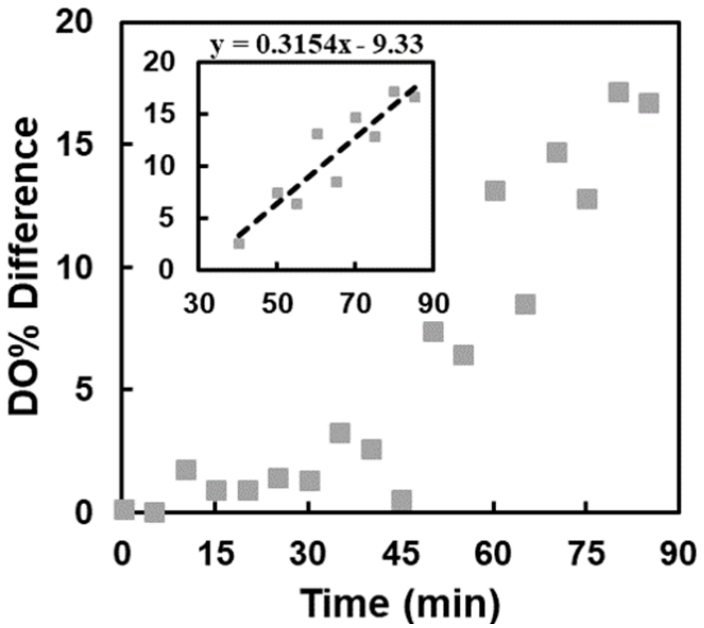

Figure 4-13. The absolute value of the variation between the bPod and DO probe was extracted over time. A correction factor for the bPod (bPod-CF) was found by linearly fitting the data once DO% difference was greater than 5%. This occurred after 45 minutes of continuous real-time testing within the 10 L bioreactor.

Chapter 5. Conclusion and Future Work

5.1. Summary

In this thesis research, a disruptive bioprocess monitoring technology, the bPod, has been developed, enabling the real-time wireless monitoring of DO in bioreactors. In completion of this platform, three main system components have been investigated and integrated into a scalable prototype: (1) an electronic module for signal conditioning and wireless data transmission, (2) an electrochemical sensor for the evaluation of DO% saturation, and (3) a leak-proof package to enclose the sensor and electronics for an underwater-environment operation.

The concept is based on several existing approaches of microsystems design stemming from ingestible and bioprocessing capsules that were reviewed in Chapter 1. However, the choice of wireless modality, sensor assembly, and packaging materials were guided towards future implementation within industrial bioreactors. Initial efforts have focused on characterization of the custom-developed Clark-type electrochemical sensors in both DI water and aqueous ionic media (0.1 M KCl). The electrochemical current response under various excitation biasing was explored for the DO sensor with an integrated FEP membrane. The successful demonstration of the Clark-type electrochemical sensor coupled with a BLE chipset for wireless data acquisition allowed for autonomous measurements controlled by a smartphone or through a computer virtual terminal software (Teraterm). Furthermore, several operation states were programmed to demonstrate scheduled measurements as well as calibration of the bPod. Control of the operational states using a smartphone enabled the bPod to be

placed in the lowest energy mode possible when idle, in order to minimize power consumption.

Numerous iterations of the 3D-pinted enclosure were explored to eliminate leaking underwater. Early generations of the design demonstrated leak-proof sealing for benchtop testing, however were not sufficient at higher system pressures relevant to bioreactor sparging conditions [114]. Minimizing the design complexity by replacing extraneous O-rings and 3D-printed extrusions from the enclosure in favor of simpler sealing methods, such as epoxy and water-resistant tape, succeeded in achieving a leak-proof condition, formation of an electrochemical well, and allowed streamlined access to the electronic components.

Electrochemical characterization was conducted first using a beaker-level setup before moving into a 10 L bioreactor vessel. For the latter case, the 10 L vessel was attached to the BioFlo310 fermenter, which enabled the generation of various DO% saturation states through the use of a built-in mass flow controller. The DO partial pressure of the system was adjusted by sparging (bubbling) in different ratios of N_2, O_2, and air, which has been monitored by the bPod. The bPod was calibrated by comparing recorded CA measurements with a commercial inline DO probe (Mettler Toledo). The fundamental behavior of the Clark electrode was verified as the electrochemical characterization of the sensor resulted in a linear current response with respect to the DO% saturation. The integration of the individual system components into a wireless *in situ* module highlighted the potential of this approach and will provide an invaluable tool for quality control and future optimization of cell cultures within bioreactors.

5.2. Future Work

The focus of this thesis was not directed toward the development of a higher quality sensor than current commercial inline probes, however validation of the bPod components demonstrated a systems integration approach for achieving a scalable wireless sensing node. Future and ongoing efforts will focus on the miniaturization of system components to achieve a smaller form factor, assessing biocompatibility with cell media, and localization of individual device nodes, which may be implemented into a sensor network to distinguish aggregation of culture parameters within large scale and single-use bioreactors.

Device Scaling

The current size of the spherically-shaped bPod prototype is 60 mm in diameter. The ultimate target size of the bPod ranges between 15-25 mm in diameter to reduce the risk of shear interactions with the cell culture and for easily inserting the bPod into large-scale industrial bioreactor system. In order to achieve a smaller form factor, each system component would require further development. First, by reducing the DO sensor form factor and improving the consistency of the fabrication process, the overall sensor reproducibility would be improved. This would eliminate the need for intermediate interfacing components such as the CEC, which takes up considerable space, and allow permanent interfacing processes such as wire bonding that are ideal for minimizing trace distance. Particularly, smaller feature sizes can be obtained via traditional MEMS fabrication techniques, which are critical for achieving system miniaturization. The current approach presented in this thesis utilizes paper masks

produced by laser cutting, which limit the feature size to 100-200 μm and produce irregularities in the deposition trace pattern. Application of photolithography and use of a transparency mask would replace the current fabrication process and allow sub-1 μm features. Finally, a flexible substrate, such as polyimide, would provide additional interfacing options for bending the connecting traces and could be integrated into the 3D-print package, further reducing the form factor.

In regard to the electronic module, scaling efforts for the bPod would focus on: 1) the design and construction of a PCB and 2) implementation of a sufficient power supply. Implementation of a PCB would greatly miniaturize the overall bPod, by replacing the soldered DIP adapters and wires with small copper traces. Sub-25 mm form factor is achievable through various implementations such as a stack board design or proper placement of sensor IC's, as shown in Figure 5-1. A major challenge with the design is maintaining a robust RF link between the bPod and external device using BLE communication. Since BLE operates at the 2.45 GHz frequency band it is susceptible to significant power dissipation through a lossy medium, such as water or cell culture. Therefore, careful attention to the antenna placement and ground plane size are needed in order to mitigate potential system losses in signal propagation. Currently, the BGM121 radio board (Silicon Labs), an ideal PCB layout for the BGM121 module, was utilized for the bPod because it incorporated an efficient ground plane design. However, the cost of this was an increase in size; compared to the BGM121 module (6.5 mm x 6.5 mm) the radio board was about 5 times larger in length and width. Design and construction of a PCB following best practices for high frequency circuit and antenna design coupled with the rest of the electronics is currently in ongoing

development. The goal is to develop a miniaturized PCB that can be integrated with a variety of electrochemical sensors, and allow for a modular means of simultaneous monitoring not only DO, but temperature and pH.

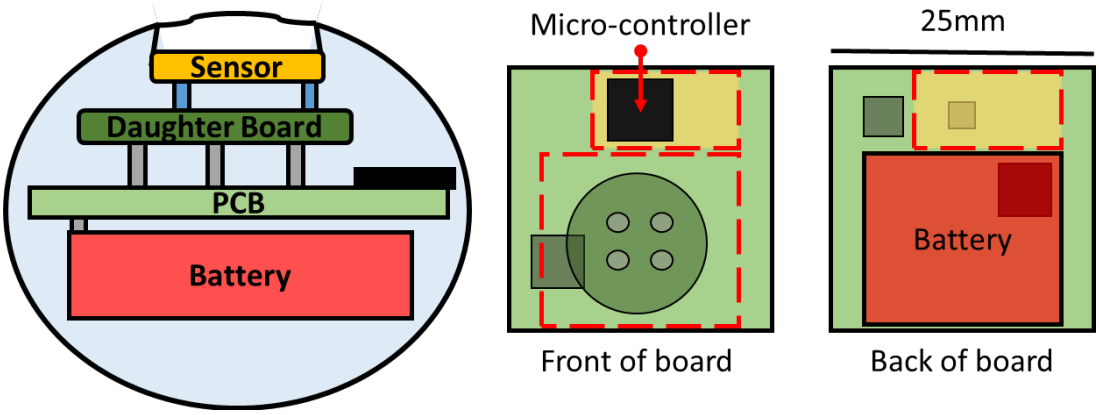

Figure 5-1. Conceptual diagram of the PCB layout for the electronic module. A sub-25 mm form factor is implemented using a) stacked boards and b) careful placement of the IC's.

Location Tracking

In addition to monitoring DO% saturation, the bPod can be used to localize culture parameter distribution. *In situ* modules provide an excellent template for the investigation of location tracking as they are able to dynamically move throughout the flow of the bioreactors. Of particular interest is identifying spatial distributions of process parameters to target product heterogeneities within the bioreactor. Future research focusing on device miniaturization and locating the bPod may utilize deployment of a Bluetooth mesh network that will ensure multihopping of data between distributed sensing devices. A mesh network would considerably improve the security

and robustness of the system, providing multiple data transmission paths to overcome failures in device connectivity.

Sensor modalities that require continuous/constant sampling (order of 1 second) or rely on iterative tracking in order to accurately assess the position of the bPod (inertial measurement units i.e. accelerometers) are not ideal for long-term sensing in bioreactors, as they drastically increase the overall power consumption. To this end, incorporation of a low-power tracking methodology leveraging the Bluetooth signal strength (RSSI) in combination with on-board sensors, pressure and magnetometer, would allow for localization of individual nodes independent of previous bPod positioning. A MEMS pressure sensor, such as the LPS33HW (ST Electronics), would provide a small form factor (3.3 mm x 3.3 mm x 2.9 mm) and monitor depth to up to 4.25 m of liquid. A magneto-resistive sensor, such as the LIS3MDL (ST Electronics) with dimensions: 2.0 mm x 2.0 mm x 1.0 mm, could also be used to correlate an observed magnetic field to the distance between the sensor and a magnetic source. For more information please refer to the following references [131]–[135]. The approaches discussed above provide a means for extracting location data wirelessly out from large-scale stainless-steel bioreactors, which would normally be impossible.

5.3. Conclusion

Growing global demand for culture products has led to the increased use of large-scale bioreactors and a shift towards parallel processing. This has necessitated the need for effective tools that both continuously monitor cell culture parameter levels, as well as identify cell culture distribution throughout the bioreactor. This thesis addresses these needs through the development of an integrated wireless platform for real time monitoring of DO, the bPod that can be integrated into a variety of bioreactor vessels as a low-cost and localizable solution for *in situ* bioprocess monitoring. Additionally, initial chronoamperometry measurements, resulting in a linear electrochemical response to DO concentrations, show significant progress towards scalable *in situ* applications targeting bioreactor heterogeneity. Lastly, it is believed that successful integration into bioreactors and further development of innovative autonomous approaches such as this offers highly controllable bioreactor conditions, which will promote large scale production of increasingly complex biologics.

Appendix A – SmartCAP Specifications

Table A-1. Properties of smartCAP product from smartINST.

Metrics	**smartCAPS**
Wireless Transmission	443MHz
Neutral Buoyancy	Yes (offers various density capsules)
Size	25 mm
Duration	up to 400 hrs → Minimum of 100 hours
Material	PEET (autoclavable)
Biocompatible	USP class VI compliant
Sampling rate	240 per second
Parallel monitoring	Up to 5
External Interface	smartCENTER*

Appendix B – Glucose Testing Protocol

Glucose Experiment Procedure:

1. Allow 15 minutes for temperature acclimation of sensor in air.
2. Submerge electrode for 30 seconds in 1x PBS (pH 7.2) solution (negative control), while monitoring the open circuit potential.
3. Perform a Cyclic Voltammetry (CV) measurement with the BioLogic potentiostat, scanning from 0.2 to -0.5 V at a 20 mV/s scan rate. Then remove GOx electrode.
4. Perform over range of target concentrations between PBS, 10 µM, 100 µM, 200 µM, 500 µm, and 1 mM.
5. Submerge electrode for 30 seconds in PBS (negative control). The use of consistent binding times allows for normalization of the decay time of each Chronoamperometric (CA) measurement.
6. Apply zero voltage bias pulse for 30 seconds. This normalizes the open circuit potential (E_{OC}) across subsequent measurements.
7. Apply a -0.1 V bias voltage for 100 seconds and determine global time point for measurement acquisition (~40 seconds).
8. Perform over range of target concentrations between PBS, 10 µM, 100 µM, 200 µM, 500 µm, and 1 mM.
9. Repeat for several electrodes.

Appendix C – Description of bPod Electronic Module

Electronic Module Parts List

Table C-1. Parts list for the bPod, including quantity and relevant dimensions for the electronic module.

Quantity	Name	Dimension
1	BGM121 Radio board	40 mm x 35 mm
1	TLV7033	2.9 mm x 1.6 mm
1	LMP91000	4 mm x 4mm
2	4k99 Ohm Resistors	Through-hole
2	100uF capacitor	Through-hole
1	8-pin DIP adapter (IPC0051-ND)	25.40 mm x 15.24 mm
1	20-pin DIP adapter (DR050D254P020-ND)	17.78mm x 25.40mm
1	Card edge connector (A101966-ND)	14 mm x 10 mm x 8 mm
1	Li-Po Battery (GM301014H)	10 mm x 15 mm

Description of I^2C

I^2C is a universal communication protocol allowing for IC's to be paired with a microcontroller. By producing the proper bit sequences, the Master microcontroller and the Slave sensor will "handshake". This communication is driven by comparing two input lines: a clock waveform (SCL) and a data sequence (SDA). The voltage is held at V_{DD} using a pull-up resistor and then driven low (using ground) by the microcontroller to produce the pulse sequence. Below is an example sequence to highlight the communication between the master and slave. A START bit, or a falling edge when the clock is high, initiates the sequence. The master then produces a seven bit device ID followed by one read or write bit. Here, the MCU is polling for the slave sensor and telling it which operation to perform on the device register. Ideally, if there are multiple sensors connected to the I^2C bus, they can be differentiated by a unique 7-bit ID. If the ID sent out by the microcontroller and the sensor/AFE matches then the slave will "acknowledge" (ACK) the master. In the case of a "no acknowledge" (NACK), the devices will be unable to be paired. Finally, a STOP bit is sent to end the sequence, which is denoted by a rising edge when the clock is high.

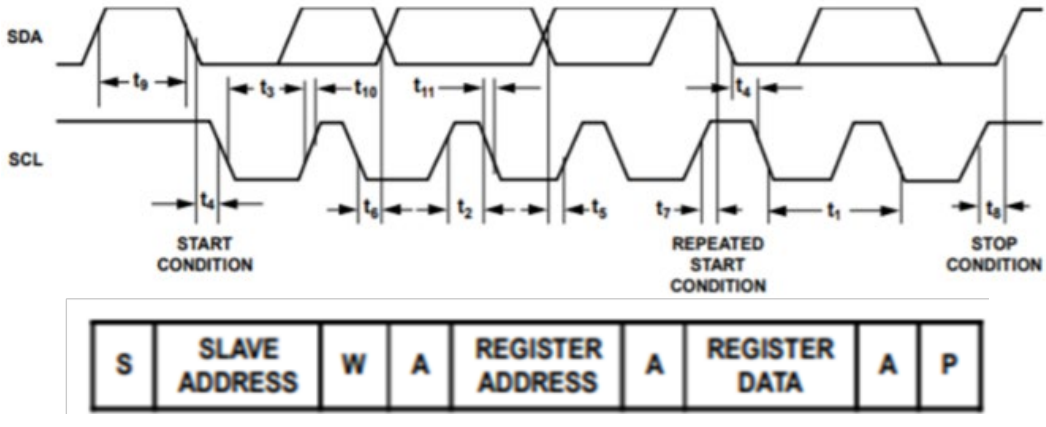

Figure A-1. I^2C sequence description for master and slave communication.

Appendix D – Description of Gen. 1 and Gen. 2 Enclosures

Generation 1: 3D-printed bPod Enclosure Description

The interface consisted of two separate parts. An extrusion from the 3D-printed enclosure is sealed with two PDMS gaskets (Figure 3-14a and 3-14b) to keep liquid from infiltrating around the edges of the sensor. This gasket was necessary because the sensing electrodes were fabricated using glass substrates which are prone to cracking under excess force. Next, the top part of the interface utilized an identical sealing gasket and was pressed down onto the sensor using two thermoset inserts and two screws. The goal of the interface was to establish a non-permanent seal that would both preserve the electrode integrity and allow for interchanging of different sensors. The PDMS was mixed in a 10:1 base to crosslinker ratio, and then placed in a vacuum desiccator for 30 minutes to remove bubbles from the mixture. The mixture was them inserted into each of the indentations and cured in the furnace at 60° C for 3 hours. Additionally, a small MED610 3D-printed support structure (20 mm x 10 mm) was added to reduce the risk of cracking and to improve the contact with the electronic module interface. The electrode simply slid into the 3D-printed spacer and then into the enclosure.

Due to the overall complexity of the design and tolerances of the 3D-print parts, the PDMS gaskets ultimately were prone to spurious leaking. It was determined that direct application of the PDMS into the structure indentations did not provide sufficient surface tension to allow the uncured PDMS to maintain the gasket shape. However, direct exposure of the sensor to the environment for bioprocess monitoring was less than ideal, and therefore generation 2 of the packaging was constructed. Additional issues with generation 1 arose from inadequate sealing under medium to high pressures

such as a bubbling solution. The two points of contact between the PDMS gasket and the sensor were sufficient due to the press seal facilitated by the screws, but the design neglected to account for the necessary force into the package to seal the third gasket (semi-circle) properly, as seen in Figure 3-14a.

Generation 2: 3D-printed bPod Enclosure for

Modifications from the generation 1 to the generation 2 bPod enclosures are detailed below. Minor improvements consisted of tighter tolerances on the O-rings seals and handle to help grip the two halves of the packaging for separation. More significantly a robust sensor interface was designed to completely encapsulate the sensor. Improving upon the application of PDMS gaskets, the second generation utilized two concentric commercial O-rings (11 mm and 5 mm diameter) for leak-proof sealing. Additionally, instead of the entrance of the packaging being a slit with an exposed sensor; the extrusion from the main 3D-print incorporated a 7 mm circular opening with a depth of 2 mm. As seen in Fig 3-15b, a 3D-printed top held two O-rings that would be brought into contact with the sensor, and had a 5 mm circular opening with a depth of 5 mm. The outer O-ring is pressed against the 3D-printed package to prevent liquid from reaching the electronic module, whereas the inner O-ring is pressed solely against the glass substrate, thus isolating the inner chamber solution at the working electrode. This enhancement created a reservoir for the DO sensor, enabling amperometric measurement. The chamber was filled with an electrolyte solution and covered by a liquid impermeable, gas permeable FEP membrane stretched across the

top of the 5 mm opening, which is then sealed into place with a 5 mm diameter O-ring (Figure 3-15b).

Improvements to the liquid sealing of the sensor interface as compared to the generation 1 design were required to enable preliminary measurements to be taken more reliably with the DO sensor. As such, the 3D-printed screw-top sensor interface was devised to eliminate persistent leaking into the bPod enclosure. The sensors are fabricated on a 500 μm thick Pyrex substrate and are quite fragile, which introduced several leaking issues. Particularly, when the O-ring at the intersection of the 3D-printed screw-top and the bPod began to press against the electrode, the electrode would simply bend downward or break. To prevent this, a spacer was 3D-printed to support the electrode, providing additional thickness and stability.

Though the generation 2 method showed much promise for creating a sealed interface between the oxygen permeable membrane and the sensor, it did not provide very accurate electrochemical measurements.

Appendix E – BGM121 Application Code

Main.c

```
/***************************************************************************************
 * \file   main.c
 * \brief  Silicon Labs Empty Example Project
 *
 * This example demonstrates the bare minimum needed for a Blue Gecko C application
 * that allows Over-the-Air Device Firmware Upgrading (OTA DFU). The application
 * starts advertising after boot and restarts advertising after a connection is
closed.

***************************************************************************************
 * <b> (C) Copyright 2016 Silicon Labs, http://www.silabs.com</b>

***************************************************************************************
 * This file is licensed under the Silabs License Agreement. See the file
 * "Silabs_License_Agreement.txt" for details. Before using this software for
 * any purpose, you must agree to the terms of that agreement.

***************************************************************************************/

/* Board headers */
#include "boards.h"
#include "ble-configuration.h"
#include "board_features.h"

/* Bluetooth stack headers */
#include "bg_types.h"
#include "native_gecko.h"
#include "gatt_db.h"
#include "aat.h"

/* Libraries containing default Gecko configuration values */
#include "em_emu.h"
#include "em_cmu.h"
#include "sleep.h"

#ifdef FEATURE_BOARD_DETECTED
#include "bspconfig.h"
#include "pti.h"
#endif

/* Device initialization header */
#include "InitDevice.h"

#ifdef FEATURE_SPI_FLASH
#include "em_usart.h"
#include "mx25flash_spi.h"
#endif /* FEATURE_SPI_FLASH */

#include "LMP91000.h"
#include "em_system.h"
#include "em_i2c.h"

#include "retargetserial.h"
#include <stdio.h>

#include "em_adc.h"
#include "em_cryotimer.h"
#include "em_gpio.h"

#define UINT32_TO_BITSTREAM(p, n)    {*(p)++ = (uint8_t)(n); *(p)++ = (uint8_t)((n) >>
8); \
                                      *(p)++ = (uint8_t)((n) >> 16); *(p)++ =
(uint8_t)((n) >> 24);}
```

```
#define UINT32_TO_BYTE0(n)        ((uint8_t) (n))
#define UINT32_TO_BYTE1(n)        ((uint8_t) ((n) >> 8))
#define UINT32_TO_BYTE2(n)        ((uint8_t) ((n) >> 16))
#define UINT32_TO_BYTE3(n)        ((uint8_t) ((n) >> 24))

/*******************************************************************************
                          Values for ADC Gain Calibration
*******************************************************************************/

#define ADC_CLOCK               11000000        /* ADC conversion clock */
#define ILLEGAL_VALUE           0xffff          /* Invalid 12 bit ADC value */
#define ADC_NEG_OFFSET_VALUE    0xfff0
#define ADC_PRS_CH_SELECT       adcPRSSELCh0
#define ADC_GAIN_CAL_VALUE      0xffd0          /* ADC gain calibration value */
#define ADC_SINGLE_DVL          4
//#define ADC_CAL_INPUT           adcSingleInputCh4
#define ADC_CAL_INPUT           adcPosSelAPORT1YCH11

uint32_t sampleValue_P22 = 100;
uint32_t sampleValue_P7 = 100;

uint32_t newGainOffsetValue;
int i;
int convert_P7;
int voltage_P7;
int sample_P7_flag = 0;
uint8_t Device_Select = 0;
char space[6];

uint8_t ADCTempBuffer_P7[4];
//uint32_t ADCconverted;   /* Stores the temperature data read from the sensor in the
correct format */
uint8_t *p_34 = ADCTempBuffer_P7; /* Pointer to HTM temperature buffer needed for
converting values to bitstream. */

/*******************************************************************************
                              Values for I2C Communication
*******************************************************************************/

/* Define the data storage locations and set polling flags for the I2C transfer. */
uint8_t status;
uint8_t modestatus;
uint8_t lockstatus1;
uint8_t lockstatus2;
uint8_t tiastatus;
uint8_t refstatus;
uint32_t statusresult = 1;
uint32_t moderesult = 1;
uint32_t lockresult = 1;
uint32_t tiaresult = 1;
uint32_t refresult = 1;
int led = 0;
bool menb;

/*******************************************************************************
                          Values for RTCC and CRYO Timers
*******************************************************************************/

#define REACTION                    30
#define SLEEP                       15
#define DATA                        10

int count = 0;

/*******************************************************************************
                                   ADC Functions
```

```
*****************************************************************************************/

void ADC0_IRQHandler(void)
{
  /* Clear ADC0 interrupt flag */
  ADC_IntClear(ADC0, ADC_IFC_SINGLECMP);
  sampleValue_P7 = ADC_DataSingleGet(ADC0);
}

void adcSingle_P7(void)
{
        ADC0_enter_DefaultMode_from_RESET();
        ADC_Start(ADC0, adcStartSingle);

          /* Wait while conversion is active */
          while (ADC0->STATUS & ADC_STATUS_SINGLEACT){}
          while ((ADC0 ->STATUS & ADC_STATUS_SINGLEDV) == 0){}

          /* Get ADC result */
          sampleValue_P7 = ADC_DataSingleGet(ADC0);

          ADC_Reset(ADC0);
}

/*****************************************************************************************
                                        I2C Functions

*****************************************************************************************/

void LMP91000_Enable(bool menb){
        if(menb){
                GPIO_PinModeSet(gpioPortF, 4,gpioModePushPull,0);
        }
        else
        {
                GPIO_PinModeSet(gpioPortF, 4,gpioModePushPull,1);
        }
}

void apply_bias(void)
{
/* Set MENB low in order to allow I2C communication between the LMP91000 and BGM121.*/
    LMP91000_Enable(true);
/* Poll the Status Register to determine whether the device is powered up.*/
        while(!(statusresult == LMP91000_OK)){
                        statusresult = LMP91000_Read( LMP91000_STATUS_REG, 1, &status);
        }
        statusresult = 1; // Reset flag for STATUS read. Can remove eventually.
/* Set the MODECN Register in power saver mode. Poll the result.*/
        LMP91000_MODECNRegister_Write(LMP91000_FET_SHORT_DISABLED,LMP91000_OP_MODE_AMP
EROMETRIC);
        while(!(moderesult == LMP91000_OK)){
                        moderesult = LMP91000_Read(LMP91000_MODECN_REG,1,&modestatus);
        }
        moderesult = 1; // Reset flag for MODECN read.
/* Set the Lock Register to "unlock" to write to TIA/REF registers. Poll the result.*/
        LMP91000_LockRegister_Write(LMP91000_WRITE_UNLOCK);
        while(!(lockresult == LMP91000_OK)){
                        lockresult = LMP91000_Read(LMP91000_LOCK_REG,1,&lockstatus1);
                }
        lockresult = 1; // Reset flag for LOCK read.
/* Set the TIACN Register to desired gain and load. Poll the result.*/
        LMP91000_TIACNRegister_Write(LMP91000_TIA_GAIN_120K, LMP91000_RLOAD_100OHM);
        while(!(tiaresult == LMP91000_OK)){
                        tiaresult = LMP91000_Read(LMP91000_TIACN_REG,1,&tiastatus);
        }
        tiaresult = 1; // Reset flag for TIACN read.
/* Set the REFCN Register to reference source, reference value as a percent of Vdd,
 *  bias voltage sign, and bias voltage value as a percent of Vdd. Poll the result.*/
```

```
        LMP91000_REFCNRegister_Write(LMP91000_REF_SOURCE_INT,LMP91000_INT_Z_50PCT,LMP9
1000_BIAS_SIGN_NEG, LMP91000_BIAS_16PCT);
        while(!(refresult == LMP91000_OK)){
                        refresult = LMP91000_Read(LMP91000_REFCN_REG,1,&refstatus);
        }
        refresult = 1; // Reset flag for REFCN read.
/* Set the Lock Register to "lock" to disable the TIA/REF registers. Poll the
result.*/
        LMP91000_LockRegister_Write(LMP91000_WRITE_LOCK);
        while(!(lockresult == LMP91000_OK)){
                        lockresult = LMP91000_Read(LMP91000_LOCK_REG,1,&lockstatus2);
        }
        lockresult = 1; // Reset flag for LOCK read.

        LMP91000_Enable(false);
}

void standby_state(void)
{

/* Set MENB low in order to allow I2C communication between the LMP91000 and BGM121.*/
    LMP91000_Enable(true);
/* Poll the Status Register to determine whether the device is powered up.*/
        while(!(statusresult == LMP91000_OK)){
                        statusresult = LMP91000_Read( LMP91000_STATUS_REG, 1, &status);
        }
        statusresult = 1; // Reset flag for STATUS read. Can remove eventually.
/* Set the MODECN Register in power saver mode. Poll the result.*/
        LMP91000_MODECNRegister_Write(LMP91000_FET_SHORT_DISABLED,LMP91000_OP_MODE_STA
NDBY);
        while(!(moderesult == LMP91000_OK)){
                        moderesult = LMP91000_Read(LMP91000_MODECN_REG,1,&modestatus);
        }
        moderesult = 1; // Reset flag for MODECN read.
/* Set the Lock Register to "unlock" to write to TIA/REF registers. Poll the result.*/
        LMP91000_LockRegister_Write(LMP91000_WRITE_UNLOCK);
        while(!(lockresult == LMP91000_OK)){
                        lockresult = LMP91000_Read(LMP91000_LOCK_REG,1,&lockstatus1);
                }
        lockresult = 1; // Reset flag for LOCK read.
/* Set the TIACN Register to desired gain and load. Poll the result.*/
        LMP91000_TIACNRegister_Write(LMP91000_TIA_GAIN_35K, LMP91000_RLOAD_100OHM);
        while(!(tiaresult == LMP91000_OK)){
                        tiaresult = LMP91000_Read(LMP91000_TIACN_REG,1,&tiastatus);
        }
        tiaresult = 1; // Reset flag for TIACN read.
/* Set the REFCN Register to reference source, reference value as a percent of Vdd,
 *  bias voltage sign, and bias voltage value as a percent of Vdd. Poll the result.*/
        LMP91000_REFCNRegister_Write(LMP91000_REF_SOURCE_INT,LMP91000_INT_Z_50PCT,LMP9
1000_BIAS_SIGN_NEG, LMP91000_BIAS_0PCT);
        while(!(refresult == LMP91000_OK)){
                        refresult = LMP91000_Read(LMP91000_REFCN_REG,1,&refstatus);
        }
        refresult = 1; // Reset flag for REFCN read.
/* Set the Lock Register to "lock" to disable the TIA/REF registers. Poll the
result.*/
        LMP91000_LockRegister_Write(LMP91000_WRITE_LOCK);
        while(!(lockresult == LMP91000_OK)){
                        lockresult = LMP91000_Read(LMP91000_LOCK_REG,1,&lockstatus2);
        }
        lockresult = 1; // Reset flag for LOCK read.

        LMP91000_Enable(false);
}

void enable_sleep(void)
{
/* Set MENB low in order to allow I2C communication between the LMP91000 and BGM121.*/
    LMP91000_Enable(true);
/* Poll the Status Register to determine whether the device is powered up.*/
```

```
        while(!(statusresult == LMP91000_OK)){
                        statusresult = LMP91000_Read( LMP91000_STATUS_REG, 1, &status);
        }
        statusresult = 1; // Reset flag for STATUS read. Can remove eventually.
/* Set the MODECN Register in power saver mode. Poll the result.*/
        LMP91000_MODECNRegister_Write(LMP91000_FET_SHORT_ENABLED,LMP91000_OP_MODE_DEEP
_SLEEP);
        while(!(moderesult == LMP91000_OK)){
                        moderesult = LMP91000_Read(LMP91000_MODECN_REG,1,&modestatus);
        }
        moderesult = 1; // Reset flag for MODECN read.
/* Set the Lock Register to "unlock" to write to TIA/REF registers. Poll the result.*/
        LMP91000_LockRegister_Write(LMP91000_WRITE_UNLOCK);
        while(!(lockresult == LMP91000_OK)){
                        lockresult = LMP91000_Read(LMP91000_LOCK_REG,1,&lockstatus1);
                }
        lockresult = 1; // Reset flag for LOCK read.
/* Set the TIACN Register to desired gain and load. Poll the result.*/
        LMP91000_TIACNRegister_Write(LMP91000_TIA_GAIN_35K, LMP91000_RLOAD_100OHM);
        while(!(tiaresult == LMP91000_OK)){
                        tiaresult = LMP91000_Read(LMP91000_TIACN_REG,1,&tiastatus);
        }
        tiaresult = 1; // Reset flag for TIACN read.
/* Set the REFCN Register to reference source, reference value as a percent of Vdd,
 *  bias voltage sign, and bias voltage value as a percent of Vdd. Poll the result.*/
        LMP91000_REFCNRegister_Write(LMP91000_REF_SOURCE_INT,LMP91000_INT_Z_50PCT,LMP9
1000_BIAS_SIGN_POS, LMP91000_BIAS_0PCT);
        while(!(refresult == LMP91000_OK)){
                        refresult = LMP91000_Read(LMP91000_REFCN_REG,1,&refstatus);
        }
        refresult = 1; // Reset flag for REFCN read.
/* Set the Lock Register to "lock" to disable the TIA/REF registers. Poll the
result.*/
        LMP91000_LockRegister_Write(LMP91000_WRITE_LOCK);
        while(!(lockresult == LMP91000_OK)){
                        lockresult = LMP91000_Read(LMP91000_LOCK_REG,1,&lockstatus2);
        }
        lockresult = 1; // Reset flag for LOCK read.

        LMP91000_Enable(false);
}


/**************************************************************************************
                                    CRYO Functions
**************************************************************************************/

void Cryo_Setup(void)
{
  CRYOTIMER_Init_TypeDef cryoInit = CRYOTIMER_INIT_DEFAULT;

  /* Enable CRYO clock */
  CMU_ClockEnable(cmuClock_CRYOTIMER, true); // normally located in InitDevice.c

  cryoInit.enable = false;
  cryoInit.debugRun = false;
  cryoInit.em4Wakeup = true;

  //Change the period to get a different wake-up time. This in milliseconds

  cryoInit.osc = cryotimerOscULFRCO;
  cryoInit.presc = cryotimerPresc_8;
  cryoInit.period = cryotimerPeriod_64k;

  CRYOTIMER_Init(&cryoInit);

  /* Enable required interrupt */
  CRYOTIMER_IntEnable(CRYOTIMER_IF_PERIOD);
```

```
  /* Enable CRYOTIMER interrupt */
  CRYOTIMER_IntClear(CRYOTIMER_IF_PERIOD);

  NVIC_ClearPendingIRQ(CRYOTIMER_IRQn);
  NVIC_EnableIRQ(CRYOTIMER_IRQn);
}

void CRYOTIMER_IRQHandler(void)
{
  /* Read and clear interrupt source */
  CRYOTIMER_IntClear(CRYOTIMER_IF_PERIOD);
}

/***************************************************************************************
                                    SLEEP Functions

***************************************************************************************/

/*Sleep mode EM4. */
void Enter_EM4S(void)
{
        EMU_EM4Init_TypeDef em4Init = EMU_EM4INIT_DEFAULT;
    em4Init.retainUlfrco = true;
    EMU_EM4Init(&em4Init);
    SLEEP_ForceSleepInEM4();
}

/***************************************************************************************//**
 @addtogroup app
 @{

***************************************************************************************/

#ifndef MAX_CONNECTIONS
#define MAX_CONNECTIONS 4
#endif
uint8_t bluetooth_stack_heap[DEFAULT_BLUETOOTH_HEAP(MAX_CONNECTIONS)];

#ifdef FEATURE_PTI_SUPPORT
static const RADIO_PTIInit_t ptiInit = RADIO_PTI_INIT;
#endif

/* Gecko configuration parameters (see gecko_configuration.h) */
static const gecko_configuration_t config = {
  .config_flags = 0,
  .sleep.flags = SLEEP_FLAGS_DEEP_SLEEP_ENABLE,
  .bluetooth.max_connections = MAX_CONNECTIONS,
  .bluetooth.heap = bluetooth_stack_heap,
  .bluetooth.heap_size = sizeof(bluetooth_stack_heap),
  .bluetooth.sleep_clock_accuracy = 100, // ppm
  .gattdb = &bg_gattdb_data,
  .ota.flags = 0,
  .ota.device_name_len = 3,
  .ota.device_name_ptr = "OTA",
  #ifdef FEATURE_PTI_SUPPORT
  .pti = &ptiInit,
  #endif
};

/* Flag for indicating DFU Reset must be performed */
uint8_t boot_to_dfu = 0;

/**
 * @brief  Main function
 */
int main(void)
{
#ifdef FEATURE_SPI_FLASH
  /* Put the SPI flash into Deep Power Down mode for those radio boards where it is
available */
```

```
  MX25_init();
  MX25_DP();
  /* We must disable SPI communication */
  USART_Reset(USART1);

#endif /* FEATURE_SPI_FLASH */

  /* Initialize peripherals */
  enter_DefaultMode_from_RESET();

  /* Initialize stack */
  gecko_init(&config);

 //RETARGET_SerialInit();

  /* Enumerate the states of the device. STANDBY state to allow the device to
  power-up and initialize each of the components. A MEASURE state where we perform
  the scheduled measurements. A CALIBRATE state to one-shot the MEASURE command for
  one cycle. A STOP_MEASURE state to terminate measurements based on data flag.
  An OFF state to put the device into a hibernation mode (EM4) after desired
  measurements have been taken. System reset is triggered once initiated by the
  CRYOtimer, and the startup functions are called. */

 enum {OFF, SAMPLE, MEASURE, STOP_MEASURE, CALIBRATE, STANDBY };

  while (1) {
    /* Event pointer for handling events */
    struct gecko_cmd_packet* evt;

    /* Check for stack event. */
    evt = gecko_wait_event();

    /* Handle events */
    switch (BGLIB_MSG_ID(evt->header)) {
      /* This boot event is generated when the system boots up after reset.
       * Here the system is set to start advertising immediately after boot procedure.
*/
      case gecko_evt_system_boot_id:

/* Set advertising parameters. 100ms advertisement interval. All channels used. The
first two parameters are minimum and maximum advertising interval, both in units of
(milliseconds * 1.6). The third parameter '7' sets advertising on all channels. */

gecko_cmd_le_gap_set_adv_parameters(160, 160, 7);

        /* Start general advertising and enable connections. */
      gecko_cmd_le_gap_set_mode(le_gap_general_discoverable,
le_gap_undirected_connectable);
       break;

      case gecko_evt_hardware_soft_timer_id:
                if(evt->data.evt_hardware_soft_timer.handle == MEASURE){
                            standby_state(); // Turn on amperometric measurements
                            apply_bias();
                            if(count < (DATA-1))
                            {
       /*Start sampling timer and measurement timer. */

        gecko_cmd_hardware_set_soft_timer(32768*.05,SAMPLE,0);

        gecko_cmd_hardware_set_soft_timer(32768*REACTION,STOP_MEASURE,1);
        count++;
                            }
                            else if(count == (DATA-1))
                            {

        gecko_cmd_hardware_set_soft_timer(32768*(SLEEP+REACTION),MEASURE,1);
        count = 0;
                            }
                    }
```

```
                else if(evt->data.evt_hardware_soft_timer.handle == STOP_MEASURE){
                                gecko_cmd_hardware_set_soft_timer(32768*.05,SAMPLE,1);
                                enable_sleep();
                        }
                else if(evt->data.evt_hardware_soft_timer.handle == SAMPLE){
                                SLEEP_SleepBlockBegin(sleepEM2);
                                adcSingle_P7();


        gecko_cmd_gatt_server_write_attribute_value(gattdb_analog_ADC1, 0, 4,
(uint8*)&sampleValue_P7);

        gecko_cmd_gatt_server_send_characteristic_notification(0xff,
gattdb_analog_ADC1, 4, (uint8*)&sampleValue_P7);
                                SLEEP_SleepBlockEnd(sleepEM2);
                        }
                        else if(evt->data.evt_hardware_soft_timer.handle == OFF){
                                CRYOTIMER_Enable(true);
                                Enter_EM4S();
                        }
                 break;

      case gecko_evt_le_connection_closed_id:

        /* Check if need to boot to dfu mode */
        if (boot_to_dfu) {
          /* Enter to DFU OTA mode */
          gecko_cmd_system_reset(2);
        } else {
          /* Restart advertising after client has disconnected */
          gecko_cmd_le_gap_set_mode(le_gap_general_discoverable,
le_gap_undirected_connectable);
        }
        break;

      /* Events related to OTA upgrading
    ----------------------------------------------------------------------------- */

      /* Check if the user-type OTA Control Characteristic was written.
       * If ota_control was written, boot the device into Device Firmware Upgrade
(DFU) mode. */
      case gecko_evt_gatt_server_user_write_request_id:

        if (evt->data.evt_gatt_server_user_write_request.characteristic ==
gattdb_ota_control) {
          /* Set flag to enter to OTA mode */
          boot_to_dfu = 1;
          /* Send response to Write Request */
          gecko_cmd_gatt_server_send_user_write_response(
            evt->data.evt_gatt_server_user_write_request.connection,
            gattdb_ota_control,
            bg_err_success);

          /* Close connection to enter to DFU OTA mode */
          gecko_cmd_endpoint_close(evt-
>data.evt_gatt_server_user_write_request.connection);
        }
        else if (evt->data.evt_gatt_server_user_write_request.characteristic ==
gattdb_command){
                                if (evt-
>data.evt_gatt_server_user_write_request.value.data[0] == OFF){

        gecko_cmd_hardware_set_soft_timer(32768,OFF,1);
                                }
                else if (evt->data.evt_gatt_server_user_write_request.value.data[0] ==
CALIBRATE){
                                apply_bias();// Turn on voltage pulse
```

```
                //Start sampling timer and measurement timer
                gecko_cmd_hardware_set_soft_timer(32768*.05,SAMPLE,0);
                gecko_cmd_hardware_set_soft_timer(32768*REACTION, STOP_MEASURE,1);
                                }
      else if (evt->data.evt_gatt_server_user_write_request.value.data[0] == STANDBY){
                        standby_state(); // Turn on amperometric measurements
                                }
      else if (evt->data.evt_gatt_server_user_write_request.value.data[0] == MEASURE){
                                    count = 0;

        gecko_cmd_hardware_set_soft_timer(32768*(SLEEP+REACTION),MEASURE,0);
                apply_bias();// Apply excitation bias

                //Start sampling timer and measurement timer
                gecko_cmd_hardware_set_soft_timer(32768*.05,SAMPLE,0);
                gecko_cmd_hardware_set_soft_timer(32768*REACTION, STOP_MEASURE,1);
                                }
                      gecko_cmd_gatt_server_send_user_write_response(evt-
                      >data.evt_gatt_server_user_write_request.connection,
                      evt->data.evt_gatt_server_user_write_request.characteristic,0);
                      }
        break;
      default:
        break;
    }
  }
}
```

LMP91000.h File

```
#ifndef LMP91000_H
#define LMP91000_H

#include "em_device.h"
#include "i2cspm.h"

// Device Address
#define LMP91000_I2C_ADDRESS          (0x90)

// Device Registers
#define LMP91000_STATUS_REG           (0x00)    /* Read only status
register */
#define LMP91000_LOCK_REG             (0x01)    /* Protection
Register */
#define LMP91000_TIACN_REG            (0x10)    /* TIA Control
Register */
#define LMP91000_REFCN_REG            (0x11)    /* Reference Control
Register*/
#define LMP91000_MODECN_REG           (0x12)    /* Mode Control
Register */

// STATUS register bit-field definition
#define LMP91000_READY                (0x01)
#define LMP91000_NOT_READY            (0x00) //default

// LOCK register bit-field definition
#define LMP91000_WRITE_LOCK           (0x01) //default
#define LMP91000_WRITE_UNLOCK         (0x00)

// TIACN register bit-field definition
#define LMP91000_TIA_GAIN_EXT         (0x00) //default
#define LMP91000_TIA_GAIN_2P75K       (0x04)
#define LMP91000_TIA_GAIN_3P5K        (0x08)
#define LMP91000_TIA_GAIN_7K          (0x0C)
#define LMP91000_TIA_GAIN_14K         (0x10)
#define LMP91000_TIA_GAIN_35K         (0x14)
#define LMP91000_TIA_GAIN_120K        (0x18)
#define LMP91000_TIA_GAIN_350K        (0x1C)
#define LMP91000_RLOAD_10OHM          (0X00)
#define LMP91000_RLOAD_33OHM          (0X01)
#define LMP91000_RLOAD_50OHM          (0X02)
#define LMP91000_RLOAD_100OHM         (0X03) //default

// REFCN register bit-field definition
#define LMP91000_REF_SOURCE_INT       (0x00) //default
#define LMP91000_REF_SOURCE_EXT       (0x80)
#define LMP91000_INT_Z_20PCT          (0x00)
#define LMP91000_INT_Z_50PCT          (0x20) //default
#define LMP91000_INT_Z_67PCT          (0x40)
#define LMP91000_INT_Z_BYPASS         (0x60)
#define LMP91000_BIAS_SIGN_NEG        (0x00) //default
#define LMP91000_BIAS_SIGN_POS        (0x10)
#define LMP91000_BIAS_0PCT            (0x00) //default
#define LMP91000_BIAS_1PCT            (0x01)
```

```
#define LMP91000_BIAS_2PCT            (0x02)
#define LMP91000_BIAS_4PCT            (0x03)
#define LMP91000_BIAS_6PCT            (0x04)
#define LMP91000_BIAS_8PCT            (0x05)
#define LMP91000_BIAS_10PCT           (0x06)
#define LMP91000_BIAS_12PCT           (0x07)
#define LMP91000_BIAS_14PCT           (0x08)
#define LMP91000_BIAS_16PCT           (0x09)
#define LMP91000_BIAS_18PCT           (0x0A)
#define LMP91000_BIAS_20PCT           (0x0B)
#define LMP91000_BIAS_22PCT           (0x0C)
#define LMP91000_BIAS_24PCT           (0x0D)

// MODECN register bit-field definition
#define LMP91000_FET_SHORT_DISABLED   (0x00) //default
#define LMP91000_FET_SHORT_ENABLED    (0x80)
#define LMP91000_OP_MODE_DEEP_SLEEP   (0x00) //default
#define LMP91000_OP_MODE_GALVANIC     (0x01)
#define LMP91000_OP_MODE_STANDBY      (0x02)
#define LMP91000_OP_MODE_AMPEROMETRIC (0x03)
#define LMP91000_OP_MODE_TIA_OFF      (0x06)
#define LMP91000_OP_MODE_TIA_ON       (0x07)

// LMP91000 Error Status
#define LMP91000_OK                          (0x0000)
#define LMP91000_I2C_FAIL                   (0x0001)

/*****************************************************************
*********
 ***************************  PROTOTYPE
*********************************

*****************************************************************
*******/

void LMP91000_I2C_Enable(uint8_t menb);
void LMP91000_Unlock(I2C_TypeDef *i2c, uint8_t deviceAddress,
uint8_t enable);
void LMP91000_apply_bias(I2C_TypeDef *i2c, uint8_t deviceAddress);
void LMP91000_enable_sleep(I2C_TypeDef *i2c, uint8_t deviceAddress);
void LMP91000_standby_state(I2C_TypeDef *i2c, uint8_t
deviceAddress);
I2C_TransferReturn_TypeDef LMP91000_readRegister (I2C_TypeDef *i2c,
uint8_t deviceAddress, uint8_t registerAddress, uint8_t *data);
I2C_TransferReturn_TypeDef LMP91000_writeRegister (I2C_TypeDef *i2c,
uint8_t deviceAddress, uint8_t registerAddress, uint8_t *data);

#endif
```

LMP91000.c

```
/*
 * LMP91000.c
 *
 *  Created on: Jan 17, 2018
 *      Author: Justin
 */

#include <stddef.h>

#include "boards.h"
#include "ble-configuration.h"
#include "board_features.h"

/* Libraries containing default Gecko configuration values */
#include "em_emu.h"
#include "em_cmu.h"
#ifdef FEATURE_BOARD_DETECTED
#include "bspconfig.h"
#include "pti.h"
#endif


#include "em_system.h"
#include "em_i2c.h"

#include "LMP91000.h"


/**************************************************************/

I2C_TransferReturn_TypeDef LMP91000_Transfer(I2C_TypeDef *i2c,
I2C_TransferSeq_TypeDef *i2cTransfer)
{
      I2C_TransferReturn_TypeDef ret;
      ret = I2C_TransferInit(I2C0, i2cTransfer);
      while (ret == i2cTransferInProgress){
            ret = I2C_Transfer(I2C0);
      }
      return ret;
}

uint32_t LMP91000_Read( uint8_t reg, uint8_t length, uint8_t *data)
{
  /* Transfer structure */
  I2C_TransferSeq_TypeDef i2cTransfer;
  I2C_TransferReturn_TypeDef ret;
  uint8_t i2c_write_data[1];

  uint32_t retval;

  retval = LMP91000_OK;

  /* Setting pin to indicate transfer */
  GPIO_PinOutSet(gpioPortC, 0);
```

```
  /* Write data */
  i2c_write_data[0] = reg;

  /* Initializing I2C transfer */
  i2cTransfer.addr          = LMP91000_I2C_ADDRESS;
  i2cTransfer.flags         = I2C_FLAG_WRITE_READ;
  i2cTransfer.buf[0].data   = i2c_write_data;
  i2cTransfer.buf[0].len    = 1;

  /* Select length of data to be read */
  i2cTransfer.buf[1].data   = data;
  i2cTransfer.buf[1].len    = length;

  ret = LMP91000_Transfer(I2C0, &i2cTransfer);
  if( ret != i2cTransferDone ){
        retval = LMP91000_I2C_FAIL;
  }

  /* Clearing pin to indicate end of transfer */
  GPIO_PinOutClear(gpioPortC, 0);
  //enableI2cSlaveInterrupts();

  return retval;
}

uint32_t LMP91000_LockRegister_Write(uint8_t lock)
{
  /* Transfer structure */
  I2C_TransferSeq_TypeDef i2cTransfer;
  I2C_TransferReturn_TypeDef ret;
  uint8_t i2c_write_data[2];
  uint8_t i2c_read_data[0];
  uint32_t retval;

  retval = LMP91000_OK;

  /* Setting pin to indicate transfer */
  GPIO_PinOutSet(gpioPortC, 0);

  /* Write data */
  i2c_write_data[0] = LMP91000_LOCK_REG;
  i2c_write_data[1] = lock;

  /* Initializing I2C transfer */
  i2cTransfer.addr          = LMP91000_I2C_ADDRESS;
  i2cTransfer.flags         = I2C_FLAG_WRITE;
  i2cTransfer.buf[0].data   = i2c_write_data;
  i2cTransfer.buf[0].len    = 2;

  /* Select length of data to be read */
  i2cTransfer.buf[1].data   = i2c_read_data;
  i2cTransfer.buf[1].len    = 0;

  ret = LMP91000_Transfer(I2C0, &i2cTransfer);
  if( ret != i2cTransferDone ){
```

```
        retval = LMP91000_I2C_FAIL;
  }

  /* Clearing pin to indicate end of transfer */
  GPIO_PinOutClear(gpioPortC, 0);
  //enableI2cSlaveInterrupts();

  return retval;
}

uint32_t LMP91000_TIACNRegister_Write(uint8_t tia_gain, uint8_t load
)
{
  /* Transfer structure */
  I2C_TransferSeq_TypeDef i2cTransfer;
  I2C_TransferReturn_TypeDef ret;
  uint8_t i2c_write_data[2];
  uint8_t i2c_read_data[0];
  uint32_t retval;

  retval = LMP91000_OK;

  /* Setting pin to indicate transfer */
  GPIO_PinOutSet(gpioPortC, 0);

  /* Write data */
  i2c_write_data[0] = LMP91000_TIACN_REG;
  i2c_write_data[1] = tia_gain | load;

  /* Initializing I2C transfer */
  i2cTransfer.addr          = LMP91000_I2C_ADDRESS;
  i2cTransfer.flags         = I2C_FLAG_WRITE;
  i2cTransfer.buf[0].data   = i2c_write_data;
  i2cTransfer.buf[0].len    = 2;

  /* Select length of data to be read */
  i2cTransfer.buf[1].data   = i2c_read_data;
  i2cTransfer.buf[1].len    = 0;

  ret = LMP91000_Transfer(I2C0, &i2cTransfer);
  if( ret != i2cTransferDone ){
        retval = LMP91000_I2C_FAIL;
  }

  /* Clearing pin to indicate end of transfer */
  GPIO_PinOutClear(gpioPortC, 0);
  //enableI2cSlaveInterrupts();

  return retval;
}

uint32_t LMP91000_REFCNRegister_Write(uint8_t ref_source, uint8_t
int_z, uint8_t polarity, uint8_t bias_pct)
{
  /* Transfer structure */
  I2C_TransferSeq_TypeDef i2cTransfer;
```

```
  I2C_TransferReturn_TypeDef ret;
  uint8_t i2c_write_data[2];
  uint8_t i2c_read_data[0];
  uint32_t retval;

  retval = LMP91000_OK;

  /* Setting pin to indicate transfer */
  GPIO_PinOutSet(gpioPortC, 0);

  /* Write data */
  i2c_write_data[0] = LMP91000_REFCN_REG;
  i2c_write_data[1] = ref_source | int_z | polarity | bias_pct;

  /* Initializing I2C transfer */
  i2cTransfer.addr          = LMP91000_I2C_ADDRESS;
  i2cTransfer.flags         = I2C_FLAG_WRITE;
  i2cTransfer.buf[0].data   = i2c_write_data;
  i2cTransfer.buf[0].len    = 2;

  /* Select length of data to be read */
  i2cTransfer.buf[1].data   = i2c_read_data;
  i2cTransfer.buf[1].len    = 0;

  ret = LMP91000_Transfer(I2C0, &i2cTransfer);
  if( ret != i2cTransferDone ){
        retval = LMP91000_I2C_FAIL;
  }

  /* Clearing pin to indicate end of transfer */
  GPIO_PinOutClear(gpioPortC, 0);
  //enableI2cSlaveInterrupts();

  return retval;
}

uint32_t LMP91000_MODECNRegister_Write(uint8_t fet_short, uint8_t
op_mode)
{
  /* Transfer structure */
  I2C_TransferSeq_TypeDef i2cTransfer;
  I2C_TransferReturn_TypeDef ret;
  uint8_t i2c_write_data[2];
  uint8_t i2c_read_data[0];
  uint32_t retval;

  retval = LMP91000_OK;

  /* Setting pin to indicate transfer */
  GPIO_PinOutSet(gpioPortC, 0);

  /* Write data */
  i2c_write_data[0] = LMP91000_MODECN_REG;
  i2c_write_data[1] = fet_short | op_mode;

  /* Initializing I2C transfer */
```

```
  i2cTransfer.addr          = LMP91000_I2C_ADDRESS;
  i2cTransfer.flags         = I2C_FLAG_WRITE;
  i2cTransfer.buf[0].data   = i2c_write_data;
  i2cTransfer.buf[0].len    = 2;

  /* Select length of data to be read */
  i2cTransfer.buf[1].data   = i2c_read_data;
  i2cTransfer.buf[1].len    = 0;

  ret = LMP91000_Transfer(I2C0, &i2cTransfer);
  if( ret != i2cTransferDone ){
        retval = LMP91000_I2C_FAIL;
  }

  /* Clearing pin to indicate end of transfer */
  GPIO_PinOutClear(gpioPortC, 0);
  //enableI2cSlaveInterrupts();

  return retval;
}
```

References

[1] G. P. Adams and L. M. Weiner, “Monoclonal antibody therapy of cancer,” vol. 23, no. 9, pp. 1147–1157, 2005.

[2] Z. S. Wallace *et al.*, “Plasmablasts as a biomarker for IgG4-related disease, independent of serum IgG4 concentrations,” *Ann. Rheum. Dis.*, vol. 74, no. 1, pp. 190–195, Jan. 2015.

[3] N. Carreau and A. Pavlick, “Revolutionizing treatment of advanced melanoma with immunotherapy,” *Surg. Oncol.*, 2019.

[4] G. J. Weiner, “Building better monoclonal antibody-based therapeutics,” *Nat. Rev. Cancer*, vol. 15, p. 361, May 2015.

[5] B. Somasundaram, K. Pleitt, E. Shave, K. Baker, and L. H. L. Lua, “Progression of continuous downstream processing of monoclonal antibodies: Current trends and challenges,” *Biotechnol. Bioeng.*, vol. 115, no. 12, pp. 2893–2907, Dec. 2018.

[6] M. Vázquez-Rey and D. A. Lang, “Aggregates in monoclonal antibody manufacturing processes,” *Biotechnol. Bioeng.*, vol. 108, no. 7, pp. 1494–1508, Jul. 2011.

[7] F. Torkashvand and B. Vaziri, “Main Quality Attributes of Monoclonal Antibodies and Effect of Cell Culture Components,” *Iran. Biomed. J.*, vol. 21, no. 3, pp. 131–141, May 2017.

[8] A. R. Lara, E. Galindo, O. T. Ramírez, and L. A. Palomares, “Living with heterogeneities in bioreactors,” *Mol. Biotechnol.*, vol. 34, no. 3, pp. 355–381, 2006.

[9] J. Y. Kim, Y.-G. Kim, and G. M. Lee, “CHO cells in biotechnology for production of recombinant proteins: current state and further potential[1] J. Y. Kim, Y.-G. Kim, and G. M. Lee, ‘CHO cells in biotechnology for production of recombinant proteins: current state and further potential,’ Appl. ,” *Appl. Microbiol. Biotechnol.*, vol. 93, no. 3, pp. 917–930, 2012.

[10] H. F. S. Freitas and C. G. M. Andrade, “A brief review on biotechnological process sensoring,” *2015 IEEE 12th Int. Conf. Electron. Meas. Instruments, ICEMI 2015*, vol. 3, pp. 1622–1627, 2016.

[11] Y. Obeidat and T. Chen, “Characterization of an O2 sensor using microelectrodes,” in *2016 IEEE SENSORS*, 2016, pp. 1–3.

[12] P. Gronemeyer, R. Ditz, and J. Strube, “Trends in Upstream and Downstream Process Development for Antibody Manufacturing,” *Bioengineering* , vol. 1, no. 4. 2014.

[13] J. Kim *et al.*, “Biosensors and Bioelectronics Wearable salivary uric acid mouthguard biosensor with integrated wireless electronics,” *Biosens. Bioelectron.*, vol. 74, pp. 1061–1068, 2015.

[14] H. Yoon, X. Xuan, S. Jeong, and J. Y. Park, “Wearable, robust, non-enzymatic

continuous glucose monitoring system and its in vivo investigation," *Biosens. Bioelectron.*, vol. 117, no. May, pp. 267–275, 2018.

[15] A. Pal, D. Goswami, H. E. Cuellar, B. Castro, and S. Kuang, "Biosensors and Bioelectronics Early detection and monitoring of chronic wounds using low-cost , omniphobic paper-based smart bandages," *Biosens. Bioelectron.*, vol. 117, no. July, pp. 696–705, 2018.

[16] R. C. Huiszoon, S. Subramanian, P. R. Rajasekaran, L. A. Beardslee, W. E. Bentley, and R. Ghodssi, "Flexible Platform for In Situ Impedimetric Detection and Bioelectric Effect Treatment of Escherichia coli Biofilms," vol. 9294, no. c, pp. 1–9, 2018.

[17] S. Søpstad, K. Imenes, and E. Johannessen, *Hybrid electrochemical sensor platform for capsaicin determination using coarsely stepped cyclic squarewave voltammetry*, vol. 130. 2018.

[18] L. C. Clark, "Monitor and Control of Blood and Tissue Oxygen," *Trans. Am. Soc. Artif. Intern. Organs*, vol. 2, no. 1, pp. 41–48, 1956.

[19] S. Yang and X. Liu, "Cell culture processes for biologics manufacturing: recent developments and trends »," *Pharm. Bioprocess.*, vol. 1, no. 2013, pp. 133–136, 2016.

[20] A. F. Jozala *et al.*, "Biopharmaceuticals from microorganisms: from production to purification," *Braz. J. Microbiol.*, vol. 47 Suppl 1, no. Suppl 1, pp. 51–63, Oct. 2016.

[21] A. A. Shukla, B. Hubbard, T. Tressel, S. Guhan, and D. Low, "Downstream processing of monoclonal antibodies—Application of platform approaches," *J. Chromatogr. B*, vol. 848, no. 1, pp. 28–39, 2007.

[22] A. A. Shukla and J. Thömmes, "Recent advances in large-scale production of monoclonal antibodies and related proteins," *Trends Biotechnol.*, vol. 28, no. 5, pp. 253–261, 2010.

[23] F. M. Wurm, "Production of recombinant protein therapeutics in cultivated mammalian cells," *Nat. Biotechnol.*, vol. 22, no. 11, pp. 1393–1398, 2004.

[24] M. Butler, "Animal cell cultures: Recent achievements and perspectives in the production of biopharmaceuticals," *Appl. Microbiol. Biotechnol.*, vol. 68, no. 3, pp. 283–291, 2005.

[25] F. Li, N. Vijayasankaran, A. Y. Shen, R. Kiss, and A. Amanullah, "Cell culture processes for monoclonal antibody production," *MAbs*, vol. 2, no. 5, pp. 466–479, 2010.

[26] Y. Zhou *et al.*, "Effects of Agitation, Aeration and Temperature on Production of a Novel Glycoprotein GP-1 by Streptomyces kanasenisi ZX01 and Scale-Up Based on Volumetric Oxygen Transfer Coefficient.," *Molecules*, vol. 23, no. 1, Jan. 2018.

[27] R. Kunert and D. Reinhart, "Advances in recombinant antibody

manufacturing," *Appl. Microbiol. Biotechnol.*, vol. 100, no. 8, pp. 3451–3461, 2016.

[28] A. L. Zydney, "Perspectives on integrated continuous bioprocessing—opportunities and challenges," *Curr. Opin. Chem. Eng.*, vol. 10, pp. 8–13, 2015.

[29] P. O'Mara, A. Farrell, J. Bones, and K. Twomey, "Staying alive! Sensors used for monitoring cell health in bioreactors," *Talanta*, vol. 176, pp. 130–139, 2018.

[30] FDA, "Guidance for Industry, PAT-A Framework for Innovative Pharmaceutical Development, Manufacturing and Quality Assurance," no. September, 2004.

[31] E. S. Langer and R. A. Rader, "Single-use technologies in biopharmaceutical manufacturing: A 10-year review of trends and the future," *Eng. Life Sci.*, vol. 14, no. 3, pp. 238–243, May 2014.

[32] J. C. Merchuk, "Airlift Bioreactors: Review of Recent Advances," *Can. J. Chem. Eng.*, vol. 81, no. 3–4, pp. 324–337, 2010.

[33] M. Stephenson and W. Grayson, "Recent advances in bioreactors for cell-based therapies," *F1000Research*, vol. 7, p. F1000 Faculty Rev-517, Apr. 2018.

[34] A. A. Shukla and U. Gottschalk, "Single-use disposable technologies for biopharmaceutical manufacturing," *Trends Biotechnol.*, vol. 31, no. 3, pp. 149–156, 2013.

[35] S. Lone, V. Kumar, J. Seay, D. L. Englert, and H. T. Hwang, *Evaluation of Volumetric Mass Transfer Coefficient in a Stirred Tank Bioreactor Using Response Surface Methodology*. 2018.

[36] P. O'Mara, A. Farrell, J. Bones, and K. Twomey, "Staying alive! Sensors used for monitoring cell health in bioreactors," *Talanta*, vol. 176, no. June 2017, pp. 130–139, 2018.

[37] G. T. Benz, "Piloting bioreactors for agitation scale-up," *Chem. Eng. Prog.*, vol. 104, no. 2, pp. 32–34, 2008.

[38] Y. Zhou *et al.*, "Effects of agitation, aeration and temperature on production of a novel glycoprotein gp-1 by streptomyces kanasenisi zx01 and scale-up based on volumetric oxygen transfer coefficient," *Molecules*, vol. 23, no. 1, pp. 1–14, 2018.

[39] GE Life Sciences, "What do cells need from a bioreactor ?," 2018. [Online]. Available: https://cdn.gelifesciences.com/dmm3bwsv3/AssetStream.aspx?mediaformatid=10061&destinationid=10016&assetid=26286.

[40] K. B. Konstantinov and C. L. Cooney, "White Paper on Continuous Bioprocessing May 20–21 2014 Continuous Manufacturing Symposium," *J.*

Pharm. Sci., vol. 104, no. 3, pp. 813–820, 2015.

[41] P. A. Ruffieux, U. Von Stockar, and I. W. Marison, "Measurement of volumetric (OUR) and determination of specific (qO2) oxygen uptake rates in animal cell cultures," *J. Biotechnol.*, vol. 63, no. 2, pp. 85–95, 1998.

[42] E. Casey, B. Glennon, and G. Hamer, "Oxygen mass transfer characteristics in a membrane-aerated biofilm reactor," *Biotechnol. Bioeng.*, vol. 62, no. 2, pp. 183–192, 1999.

[43] S. Suresh, V. C. Srivastava, and I. M. Mishra, "Techniques for oxygen transfer measurement in bioreactors: a review," *J. Chem. Technol. Biotechnol.*, vol. 84, no. 8, pp. 1091–1103, Aug. 2009.

[44] A. L. Damiani, M. H. Kim, and J. Wang, "An improved dynamic method to measure kLa in bioreactors," *Biotechnol. Bioeng.*, vol. 111, no. 10, pp. 2120–2125, 2014.

[45] J. B. Sieck *et al.*, "Development of a Scale-Down Model of hydrodynamic stress to study the performance of an industrial CHO cell line under simulated production scale bioreactor conditions," *J. Biotechnol.*, vol. 164, no. 1, pp. 41–49, 2013.

[46] J. A. Sánchez Pérez, E. M. Rodríguez Porcel, J. L. Casas López, J. M. Fernández Sevilla, and Y. Chisti, "Shear rate in stirred tank and bubble column bioreactors," *Chem. Eng. J.*, vol. 124, no. 1–3, pp. 1–5, 2006.

[47] C. B. Elias, R. B. Desai, M. S. Patole, J. B. Joshi, and R. A. Mashelkar, "Turbulent shear stress—Effect on mammalian cell culture and measurement using laser Doppler anemometer," *Chem. Eng. Sci.*, vol. 50, no. 15, pp. 2431–2440, 1995.

[48] M. S. Puthli, V. K. Rathod, and A. B. Pandit, "Gas–liquid mass transfer studies with triple impeller system on a laboratory scale bioreactor," *Biochem. Eng. J.*, vol. 23, no. 1, pp. 25–30, 2005.

[49] H. Ameur, "Modifications in the Rushton turbine for mixing viscoplastic fluids," *J. Food Eng.*, vol. 233, pp. 117–125, 2018.

[50] M. Irene Sánchez Cervantes, J. Lacombe, F. J. Muzzio, and M. M. Álvarez, "Novel bioreactor design for the culture of suspended mammalian cells. Part I: Mixing characterization," *Chem. Eng. Sci.*, vol. 61, no. 24, pp. 8075–8084, 2006.

[51] G. Rodriguez, M. Micheletti, and A. Ducci, "Macro- and micro-scale mixing in a shaken bioreactor for fluids of high viscosity," *Chem. Eng. Res. Des.*, vol. 132, no. 2013, pp. 890–901, 2018.

[52] B. Tang *et al.*, "Bioresource Technology Distribution and mass transfer of dissolved oxygen in a multi-habitat membrane bioreactor," *Bioresour. Technol.*, vol. 182, pp. 323–328, 2015.

[53] O. S. Wolfbeis, "Luminescent sensing and imaging of oxygen: fierce

competition to the Clark electrode," *Bioessays*, vol. 37, no. 8, pp. 921–928, Aug. 2015.

[54] X. Liu, Q. Liu, E. Gupta, N. Zorko, E. Brownlee, and J. L. Zweier, "Quantitative measurements of NO reaction kinetics with a Clark-type electrode," *Nitric Oxide*, vol. 13, no. 1, pp. 68–77, 2005.

[55] J. Park, J. H. Chang, M. Choi, J. J. Pak, D. Y. Lee, and Y. K. Pak, "Microfabirated clark-type sensor for measuing dissolved oxygen," *Proc. IEEE Sensors*, pp. 1412–1415, 2007.

[56] T.-J. Kim, T.-H. Jurng, U.-H. Chung, and S.-I. Hong, "Simultaneous determination of oxygen transport characteristics of six membranes by hexagonal dissolved oxygen sensor system," *Sensors Actuators B Chem.*, vol. 72, no. 1, pp. 11–20, 2001.

[57] Y. Zhang and I. Angelidaki, "A simple and rapid method for monitoring dissolved oxygen in water with a submersible microbial fuel cell (SBMFC)," *Biosens. Bioelectron.*, vol. 38, no. 1, pp. 189–194, 2012.

[58] P. Zimmermann, A. Weltin, G. A. Urban, and J. Kieninger, "Active Potentiometry for Dissolved Oxygen Monitoring with Platinum Electrodes," *Sensors (Basel).*, vol. 18, no. 8, p. 2404, Jul. 2018.

[59] K. Twomey, L. C. Nagle, A. Said, F. Barry, and V. I. Ogurtsov, "Characterisation of Nanoporous Gold for Use in a Dissolved Oxygen Sensing Application," *Bionanoscience*, vol. 5, no. 1, pp. 55–63, 2015.

[60] B. J. Polk, A. Stelzenmuller, G. Mijares, W. MacCrehan, and M. Gaitan, "Ag/AgCl microelectrodes with improved stability for microfluidics," *Sensors Actuators, B Chem.*, vol. 114, no. 1, pp. 239–247, 2006.

[61] H. Suzuki, H. Ozawa, S. Sasaki, and I. Karube, "A novel thin-film Ag/AgCl anode structure for microfabricated Clark-type oxygen electrodes," *Sensors Actuators B Chem.*, vol. 53, no. 3, pp. 140–146, 1998.

[62] J. R. Lakowicz and G. Weber, "Quenching of Fluorescence by Oxygen. a Probe for Structural Fluctuations in Macromolecules," *Biochemistry*, vol. 12, no. 21, pp. 4161–4170, 1973.

[63] I. Bergman, "Rapid-response atmospheric oxygen monitor based on fluorescence quenching (42)," *Nature*, vol. 218, no. 5139, p. 396, 1968.

[64] C. Cobianu, B. C. Serban, V. Avramescu, M. Brezeanu, A. Stratulat, and O. Buiu, "Novel materials for oxygen sensing technologies," *Proc. Int. Semicond. Conf. CAS*, vol. 2016-Decem, pp. 17–26, 2016.

[65] C. Staudinger *et al.*, "A versatile optode system for oxygen, carbon dioxide, and pH measurements in seawater with integrated battery and logger," *Limnol. Oceanogr. Methods*, vol. 16, no. 7, pp. 459–473, 2018.

[66] C. McDonagh *et al.*, "Phase fluorometric dissolved oxygen sensor," *Sensors Actuators, B Chem.*, vol. 74, no. 1–3, pp. 124–130, 2001.

[67] S. Søpstad, K. Imenes, and E. A. Johannessen, “Hybrid electrochemical sensor platform for capsaicin determination using coarsely stepped cyclic squarewave voltammetry,” *Biosens. Bioelectron.*, vol. 130, pp. 374–381, 2019.

[68] F. Wu, T. Wu, and M. R. Yuce, “An Internet-of-Things (IoT) Network System for Connected Safety and Health Monitoring Applications,” *Sensors (Basel).*, vol. 19, no. 1, p. 21, Dec. 2018.

[69] S. Labs, “WGM110 Wizard Gecko Wi-Fi ® Module Data Sheet,” 2017. [Online]. Available: https://www.silabs.com/documents/login/data-sheets/wgm110-datasheet.pdf.

[70] Microchip, “RN1810/RN1810E 2.4 Ghz IEEE 802.11b/g/n Wireless Module,” 2016. [Online]. Available: http://ww1.microchip.com/downloads/en/DeviceDoc/50002460B.pdf.

[71] Zentri, “Zentri AMW006/AMW106 Data Sheet,” 2017. [Online]. Available: https://www.silabs.com/documents/login/data-sheets/ADS-MWx06-ZentriOS-110R.pdf.

[72] T. Instruments, “CC3120 SimpleLink ™ Wi-Fi ® Wireless Network Processor , Internet-of-Things Solution for MCU Applications,” 2017. [Online]. Available: http://www.ti.com/lit/ds/symlink/cc3120.pdf.

[73] Nordic Semiconductor, “nRF9E5 433/868/915MHz RF Transceiver with Embedded 8051 Compatible Microcontroller and 4 Input, 10 Bit ADC,” 2004. [Online]. Available: http://www.keil.com/dd/docs/datashts/nordic/nrf9e5.pdf.

[74] S. Labs, “EFR32FG12 Flex Gecko Proprietary Protocol SoC Family Data Sheet,” 2017. [Online]. Available: https://www.silabs.com/documents/public/data-sheets/efr32fg12-datasheet.pdf.

[75] R. E. W. Solutions, “Tinymesh RF Transceiver Modules,” 2018. [Online]. Available: https://radiocrafts.com/uploads/RCxxxxHP-TM_Data_Sheet.pdf.

[76] Hoperf Electronic, “RFM69HCW ISM Transceiver Module v1.1,” 2006. [Online]. Available: https://cdn.sparkfun.com/datasheets/Wireless/General/RFM69HCW-V1.1.pdf.

[77] Nordic Semiconductor, “nRF52810 Product Specification v1.0,” 2017. [Online]. Available: https://infocenter.nordicsemi.com/pdf/nRF52810_PS_v1.0.pdf.

[78] NXP Semiconductors, “Kinetis KW41Z/31Z/21Z MCUs for Wireless Applications,” 2015. [Online]. Available: https://www.nxp.com/docs/en/fact-sheet/KNTSKW41Z31Z21ZFS.pdf.

[79] T. Instruments, “CC2564MODx Bluetooth ® Host Controller Interface (HCI) Module,” 2017. [Online]. Available: http://www.ti.com/lit/ds/symlink/cc2564moda.pdf.

[80] S. Labs, “BGM121/BGM123 Blue Gecko Bluetooth SiP Module Data Sheet,” 2017. [Online]. Available: https://www.silabs.com/documents/login/data-

sheets/bgm12x-datasheet.pdf.

[81] S. Labs, “BGM13S Blue Gecko Bluetooth ® SiP Module Data Sheet,” 2019. [Online]. Available: https://www.silabs.com/documents/login/data-sheets/bgm13s-datasheet.pdf.

[82] S. Microelectronics, “STM32WB55xx Multiprotocol wireless 32-bit MCU Arm-based Cortex-M4 with FPU, Bluetooth 5 and 802.15.4 radio solution,” 2019. [Online]. Available: https://www.st.com/resource/en/datasheet/stm32wb55rg.pdf.

[83] K. Kalantar-zadeh, N. Ha, J. Z. Ou, and K. J. Berean, “Ingestible Sensors,” *ACS Sensors*, vol. 2, no. 4, pp. 468–483, Apr. 2017.

[84] C. J. Bettinger, “Advances in Materials and Structures for Ingestible Electromechanical Medical Devices,” *Angew. Chemie Int. Ed.*, vol. 57, no. 52, pp. 16946–16958, Dec. 2018.

[85] M. Mimee *et al.*, “An ingestible bacterial-electronic system to monitor gastrointestinal health,” *Science (80-.).*, vol. 360, no. 6391, pp. 915 LP – 918, May 2018.

[86] J. Z. Ou, C. K. Yao, A. Rotbart, J. G. Muir, P. R. Gibson, and K. Kalantar-zadeh, “Human intestinal gas measurement systems: in vitro fermentation and gas capsules,” *Trends Biotechnol.*, vol. 33, no. 4, pp. 208–213, 2015.

[87] W. Xie *et al.*, “Design and Validation of a Biosensor Implantation Capsule Robot,” *J. Biomech. Eng.*, vol. 139, no. 8, p. 081003, 2017.

[88] Y. L. Kong *et al.*, “3D-Printed Gastric Resident Electronics,” *Adv. Mater. Technol.*, vol. 1800490, p. 1800490, 2018.

[89] P. Nadeau *et al.*, “Prolonged energy harvesting for ingestible devices,” *Nat. Biomed. Eng.*, vol. 1, p. 22, Feb. 2017.

[90] C. Quaglia, S. Tognarelli, E. Sinibaldi, N. Funaro, P. Dario, and A. Menciassi, *Wireless Robotic Capsule for Releasing Bioadhesive Patches in the Gastrointestinal Tract*, vol. 8. 2014.

[91] V. Vojinović, J. M. S. Cabral, and L. P. Fonseca, “Real-time bioprocess monitoring: Part I: In situ sensors,” *Sensors Actuators B Chem.*, vol. 114, no. 2, pp. 1083–1091, 2006.

[92] R. A. Potyrailo *et al.*, “Lab-scale long-term operation of passive multivariable RFID temperature sensors integrated into single-use bioprocess components,” in *2011 IEEE International Conference on RFID-Technologies and Applications*, 2011, pp. 16–19.

[93] C. Surman *et al.*, “Temperature-independent passive RFID pressure sensors for single-use bioprocess components,” *2011 IEEE Int. Conf. RFID, RFID 2011*, pp. 78–84, 2011.

[94] R. A. Potyrailo and C. Surman, “A Passive Radio-Frequency Identification (RFID) Gas Sensor With Self-Correction Against Fluctuations of Ambient

Temperature," *Sens. Actuators. B. Chem.*, vol. 185, pp. 587–593, Aug. 2013.

[95] S. Bhadra *et al.*, "Wireless passive sensor for pH monitoring inside a small bioreactor," in *2013 IEEE International Instrumentation and Measurement Technology Conference (I2MTC)*, 2013, pp. 276–279.

[96] S. Bhadra *et al.*, "Fluid Embeddable Coupled Coil Sensor for Wireless pH Monitoring in a Bioreactor," *IEEE Trans. Instrum. Meas.*, vol. 63, no. 5, pp. 1337–1346, 2014.

[97] T. Nguyen *et al.*, "Sensor-array for continuous monitoring of biochemicals for bioprocess control," in *2015 Transducers - 2015 18th International Conference on Solid-State Sensors, Actuators and Microsystems (TRANSDUCERS)*, 2015, pp. 1684–1687.

[98] N. Todtenberg *et al.*, "Autonomous sensor capsule for usage in bioreactors," *IEEE Sens. J.*, vol. 15, no. 7, pp. 4093–4102, 2015.

[99] N. Todtenberg, T. Basmer, J. Klatt, and K. Schmalz, "Estimation of 433 MHz path loss in algae culture for biosensor capsule application," in *2013 European Microwave Conference*, 2013, pp. 712–715.

[100] N. Todtenberg, J. Klatt, S. T. Schmitz-Hertzberg, F. Jorde, and K. Schmalz, "Wireless sensor capsule for bioreactors," *2013 IEEE MTT-S Int. Microw. Work. Ser. RF Wirel. Technol. Biomed. Healthc. Appl. IMWS-BIO 2013 - Proc.*, pp. 5–7, 2013.

[101] SmartINST, "In Situ Wireless Measurements," 2015. [Online]. Available: http://webma9021.wixsite.com/smartinstnew/smartcaps-in-situ-wireless-measurem.

[102] R. Zimmermann, L. Fiabane, Y. Gasteuil, R. Volk, and J.-F. Pinton, *Measuring Lagrangian accelerations using an instrumented particle*, vol. T155. 2012.

[103] R. Zimmermann, L. Fiabane, Y. Gasteuil, R. Volk, and J. F. Pinton, "Characterizing flows with an instrumented particle measuring Lagrangian accelerations," *New J. Phys.*, vol. 15, 2013.

[104] C. M. Caffrey, K. Twomey, and V. I. Ogurtsov, "Development of a wireless swallowable capsule with potentiostatic electrochemical sensor for gastrointestinal track investigation," *Sensors Actuators B Chem.*, vol. 218, pp. 8–15, Oct. 2015.

[105] P. Jesudoss *et al.*, "System packaging & integration for a swallowable capsule using a direct access sensor," in *2009 European Microelectronics and Packaging Conference*, 2009, pp. 1–4.

[106] X. Huang, S. Li, J. S. Schultz, Q. Wang, and Q. Lin, "A MEMS affinity glucose sensor using a biocompatible glucose-responsive polymer," *Sens. Actuators. B. Chem.*, vol. 140, no. 2, pp. 603–609, Jul. 2009.

[107] D. A. Gough, L. S. Kumosa, T. L. Routh, J. T. Lin, and J. Y. Lucisano, "Function of an Implanted Tissue Glucose Sensor for More than 1 Year in

Animals," *Sci. Transl. Med.*, vol. 2, no. 42, pp. 42ra53 LP-42ra53, Jul. 2010.

[108] M. Quinto, I. Losito, F. Palmisano, and C. G. Zambonin, "Disposable interference-free glucose biosensor based on an electropolymerised poly(pyrrole) permselective film," *Anal. Chim. Acta*, vol. 420, no. 1, pp. 9–17, 2000.

[109] F. Palmisano, P. G. Zambonin, D. Centonze, and M. Quinto, "A Disposable, Reagentless, Third-Generation Glucose Biosensor Based on Overoxidized Poly(pyrrole)/Tetrathiafulvalene− Tetracyanoquinodimethane Composite," *Anal. Chem.*, vol. 74, no. 23, pp. 5913–5918, Dec. 2002.

[110] W. Villena Gonzales, A. T. Mobashsher, and A. Abbosh, "The Progress of Glucose Monitoring-A Review of Invasive to Minimally and Non-Invasive Techniques, Devices and Sensors," *Sensors (Basel).*, vol. 19, no. 4, p. 800, Feb. 2019.

[111] C.-H. Tsai, Y.-H. Tang, H.-T. Chen, Y.-W. Yao, T.-C. Chien, and C.-L. Kao, "A selective glucose sensor: the cooperative effect of monoboronic acid-modified poly(amidoamine) dendrimers," *Chem. Commun.*, vol. 54, no. 36, pp. 4577–4580, 2018.

[112] S. M. Egi, C. Altepe, M. Pieri, and R. Sinoplu, "Design and Implementation of an Underwater Telemetric Glucose Monitoring System for Scuba Divers," *Hittite J. Sci. Eng.*, vol. 5, no. 2, pp. 141–146, 2018.

[113] B. Technologies, "Glucose Oxidase Biosensor Type : AC1 . GOD." [Online]. Available: https://www.basinc.com/assets/file_uploads/AC1-GODn.pdf.

[114] S. Giusti, D. Mazzei, L. Cacopardo, G. Mattei, C. Domenici, and A. Ahluwalia, "Environmental Control in Flow Bioreactors," *Processes*, vol. 5, no. 2, p. 16, 2017.

[115] T.-J. Kim, T.-H. Jurng, U.-H. Chung, and S.-I. Hong, "Simultaneous determination of oxygen transport characteristics of six membranes by hexagonal dissolved oxygen sensor system," *Sensors Actuators B Chem.*, vol. 72, no. 1, pp. 11–20, 2001.

[116] A. F. D. Cruz, N. Norena, A. Kaushik, and S. Bhansali, "A low-cost miniaturized potentiostat for point-of-care diagnosis," *Biosens. Bioelectron.*, vol. 62, pp. 249–254, 2014.

[117] T. Instruments, "LMP91000 Sensor AFE System: Configurable AFE Potentiostat for Low-Power Chemical-Sensing Applications," 2014. [Online]. Available: http://www.ti.com/lit/ds/symlink/lmp91000.pdf.

[118] T. Nordman, P. Rahikkala, and T. Hakkila, "Miniaturizing IoT Designs," *Silicon Labs*, 2017. [Online]. Available: https://smtnet.com/library/files/upload/miniaturizing-iot-designs.pdf.

[119] Bluetooth, "Bluetooth Core Specification v5.1," 2019. [Online]. Available: https://www.bluetooth.com/~/media/a32d89c21ee44b648486f1a430c2f720.ashx.

[120] D. C. Bock, A. C. Marschilok, K. J. Takeuchi, and E. S. Takeuchi, “Batteries used to power implantable biomedical devices,” *Electrochim. Acta*, vol. 84, pp. 155–164, 2012.

[121] R. A. Powers, “Batteries for low power electronics,” *Proc. IEEE*, vol. 83, no. 4, pp. 687–693, 1995.

[122] T. Instruments, “LMP91000EVM User’s Guide,” 2012. [Online]. Available: http://www.ti.com/lit/ug/snau121a/snau121a.pdf.

[123] Stratasys, “Objet350 and Objet500 Connex3,” 2016. [Online]. Available: https://www.stratasys.com/3d-printers/objet-350-500-connex3.

[124] Stratasys, “Biocompatible Biocompatible Clear MED610,” 2014. [Online]. Available: https://www.stratasys.com/-/media/files/material-spec-sheets/mds_pj_med610_0618a.pdf?la=en&hash=08DA2330C6946B5BF708D179F7465F70840F876F.

[125] M. T. Nguyen, B. Kim, H. Choo, and I. Park, “Effects of Ground Plane Size on a Square Microstrip Patch Antenna Designed on a Low-Permittivity Substrate with an Air Gap,” *2010 Int. Work. Antenna Technol.*, no. 1, pp. 1–4, 2010.

[126] J. Gębicki, A. Kloskowski, W. Chrzanowski, P. Stepnowski, and J. Namiesnik, “Application of Ionic Liquids in Amperometric Gas Sensors,” *Crit. Rev. Anal. Chem.*, vol. 46, no. 2, pp. 122–138, Mar. 2016.

[127] P. A. Rock, “The standard oxidation potential of the ferrocyanide-ferricyanide electrode at 25° and the entropy of ferrocyanide ion,” *J. Phys. Chem.*, vol. 70, no. 2, pp. 576–580, 1966.

[128] Eppendorf, “Technical application notes on cell culture and fermentation,” 2017. [Online]. Available: https://www.eppendorf.com/uploads/media/Application_bioprocess_shakers_incubators_Application-Note-Boo.pdf.

[129] M. Tian, C. Cousins, D. Beauchemin, Y. Furuya, A. Ohma, and G. Jerkiewicz, “Influence of the Working and Counter Electrode Surface Area Ratios on the Dissolution of Platinum under Electrochemical Conditions,” *ACS Catal.*, vol. 6, no. 8, pp. 5108–5116, Aug. 2016.

[130] S. Xu, J. Gavin, R. Jiang, and H. Chen, “Bioreactor productivity and media cost comparison for different intensified cell culture processes,” *Biotechnol. Prog.*, vol. 33, no. 4, pp. 867–878, Jul. 2017.

[131] S. Microelectronics, “LIS3MDL Digital output magnetic sensor :,” 2017. [Online]. Available: https://www.st.com/resource/en/datasheet/lis3mdl.pdf.

[132] S. Microelectronics, “LPS33HW digital output barometer with water-resistant package,” 2017. [Online]. Available: https://www.st.com/resource/en/datasheet/lps33hw.pdf.

[133] K.-Y. Chen, S. N. Patel, and S. Keller, “Finexus: Tracking Precise Motions of Multiple Fingertips Using Magnetic Sensing,” in *ACM CHI 2016*, 2016, pp.

1504–1514.

[134] N. Mehmood and S. M. Aziz, “Magnetic sensing technology for in vivo tracking,” in *2012 International Conference on Emerging Technologies*, 2012, pp. 1–4.

[135] O. Sosnicki, T. Porchez, G. Michaud, N. Bencheikh, and F. Claeyssen, “AC magnetic field detection system applied to motion tracking,” *Sensoren und Messsyst. 2010*, p. 7, 2010.